

## ABSTRACT

HEO, JAESEOK. Optimization of Design for SMR via Data Assimilation and Uncertainty Quantification. (Under the direction of Paul J. Turinsky).

This thesis presents work on reducing the uncertainty in thermal-hydraulic transient predictions for nuclear power plants (NPP) with a focus on SMRs characterized by the integral PWR design. The objective of a part of the study was to determine the economic benefit of conducting transient experiments on an SMR NPP. To accomplish this, a thermal-hydraulic simulator is used to complete data assimilation for input parameters to the simulator using experimental data generated by the plant. Since no such experimental data exists, it was generated using an altered simulator, referred to as the virtual NPP facilitating the investigation of the benefits of conducting various experiments and sensor deployment. The mathematical approach that is used to complete this analysis depends upon whether the system responses, i.e. sensor signals, and the system attributes, e.g. DNBR, are or are not linearly dependent upon the parameters. A linearity test showed that there exist highly nonlinear as well as mildly nonlinear responses, hence both deterministic and probabilistic methods were used to complete data assimilation and uncertainty quantification. For the mildly nonlinear transient, the Bayesian approach was used to obtain the parameters posteriori distributions assuming Gaussian distributions for the input parameters and responses. In order to obtain the a posteriori, given measurements of the observables and a priori distributions of the parameters, one solves an inverse problem calibrating the parameter values to achieve better agreement between measured and predicted sensor response values. For the highly nonlinear transient, the Markov Chain Monte Carlo method was utilized based upon Bayes theorem to estimate the posteriori distributions of parameters.

This thesis also discusses the optimization methodology used to design the plant's experiments so as to reduce a posteriori system attribute uncertainties. The optimization problem decision variables include the selection of sensor types and locations, and experiment type imposing realistic constraints, with the objective of maximizing the savings achieved by utilizing the larger degree of the plant operational freedom created by system attribute uncertainty reduction to achieve a more economical plant design, offset by the cost of sensors and experiments. The best altered design specs, which maximize the savings, constrained by the safety criteria, e.g. 95/95, were determined by solving the suboptimization problem using simulated annealing method.

Finally this thesis presents an uncertainty analysis method and result for reactor control problems. For this problem, our goal is to select the optimum algorithm that minimizes the time integrated deviation of the actual state from the desired state accounting for uncertainties introduced during the design phase due to simulator employed and operations phase due to sensor uncertainties. To minimize the deviation from the desired values, multiple control algorithms were created and tested, and the optimum control algorithm was identified.

Optimization of Design for SMR via Data Assimilation and Uncertainty Quantification

by  
Jaeseok Heo

A dissertation submitted to the Graduate Faculty of  
North Carolina State University  
in partial fulfillment of the  
requirements for the degree of  
Doctor of Philosophy

Nuclear Engineering

Raleigh, North Carolina

2011

APPROVED BY:

---

Dr. Paul J. Turinsky  
Committee Chair

---

Dr. J. Michael Doster

---

Dr. Igor A. Bolotnov

---

Dr. Negash G. Medhin

## DEDICATION

To mom and dad

## BIOGRAPHY

Jaeseok Heo was born in Jecheon, South Korea on July 16, 1980. After his graduation from Hanyang University, Seoul, South Korea, with Bachelors in Nuclear Engineering in 2007, he enrolled at North Carolina State University in Department of Nuclear Engineering as a PhD student under the direction of Dr. Paul J. Turinsky. For his PhD research, he has worked on data assimilation, uncertainty quantification, and optimization of thermal hydraulic reactor system with the specific application being SMRs. He completed his PhD in August of 2011.

## ACKNOWLEDGMENTS

This research would not have been possible without the support of many people. First, I would like to offer my gratitude to my advisor, Dr. Paul Turinsky, for his encouragement, guidance and support for the last four years. I would also like to thank Dr. Doster and Dr. Cacuci for their outstanding lectures and invaluable comments. They offered their knowledge into my dissertation. Finally, thanks to my friends at NC State, especially Ross, Cyrus, and all Dr. Turinsky's group members, for their help and suggestion.

## TABLE OF CONTENTS

<b>List of Tables .....</b>	<b>vii</b>
<b>List of Figures.....</b>	<b>viii</b>
<b>1. Introduction.....</b>	<b>1</b>
1.1. Overview of the IRIS Reactor System .....	1
1.2. Motivation.....	4
1.3. Literature Review.....	5
<b>2. Description of the Actual Work.....</b>	<b>9</b>
2.1. Linearity Test for the IRIS Reactor System .....	9
2.2. Data Assimilation and Uncertainty Quantification .....	15
2.2.1. Deterministic Method for the Mildly Nonlinear Problems .....	15
2.2.2. MCMC Method for the Nonlinear Problems .....	26
2.3. Virtual Experiments .....	29
2.4. Uncertainty Contribution to the System Attributes.....	30
2.5. Mathematical Review for the Inverse Method.....	32
2.6. Design Optimization .....	38
2.7. Uncertainty Analysis for Reactor Control.....	49
2.7.1. Control Algorithms in the Simulator .....	50
2.7.2. Optimum Control Algorithm.....	57
<b>3. Results .....</b>	<b>62</b>
3.1. Mean and Standard Deviation of A Posteriori Input Parameters .....	62
3.2. Standard Deviation of A Posteriori System Attributes .....	68
3.3. Individual Parameter's Uncertainty Contribution .....	81
3.4. MCMC Simulation.....	90
3.5. Design Optimization .....	98
3.6. Uncertainty Analysis for the Reactor Control.....	103
<b>4. Conclusions and Recommendations for Future Work.....</b>	<b>113</b>
<b>References.....</b>	<b>119</b>
<b>Appendices.....</b>	<b>123</b>
<b>Appendix A.....</b>	<b>124</b>

Appendix B .....128



## LIST OF TABLES

Table I.	Uncertainties of Observables .....	25
Table II.	Virtual Experiment Values and Input Parameters Adapted for Experiment A.....	63
Table III.	Virtual Experiment Values and Input Parameters Adapted for Experiment B.....	64
Table IV.	Virtual Experiment Values and Input Parameters Adapted for Experiment C.....	64
Table V.	Virtual Experiment Values and Input Parameters Adapted for Experiment D.....	65
Table VI.	Virtual Experiment Values and Input Parameters Adapted using Experiments A, B, C and D .....	65
Table VII.	A Posteriori Standard Deviations for the Input Parameters using Experiment A for MCMC Simulation .....	98
Table VIII.	Deviations for 10% Step Load Changes at 70% and 90% Power using Four Different Control Algorithms .....	106
Table IX.	Operational Constraint Probability for 10% Step Load Changes at 70% and 90% Power using Four Different Control Algorithms.....	106
Table X.	Safety Constraint Probability for 10% Step Load Changes at 70% and 90% Power using Four Different Control Algorithms.....	107
Table XI.	Deviations for 20% Ramp Load Changes at 70%Power using Four Different Control Algorithms .....	107
Table XII.	Operational Constraint Probability for 10% Step Load Changes at 70% and 90% Power using Four Different Control Algorithms.....	107
Table XIII.	Safety Constraint Probability for 10% Step Load Changes at 70% and 90% Power using Four Different Control Algorithms .....	108

## LIST OF FIGURES

Figure 1.	Layout of the IRIS Primary System .....	3
Figure 2.	Pressurizer Heater Output .....	10
Figure 3.	Primary Pressure .....	11
Figure 4-1.	Chi-Squared Values for the Primary Side of the System for the 10% Step Load Change .....	11
Figure 4-2.	Chi-Squared Values for the Secondary Side of the System for the 10% Step Load Change .....	12
Figure 5-1.	Chi-Squared Values for the Primary Side of the System for the Uncontrolled Rod Bank Withdrawal obtained with Inactive Controllers .....	13
Figure 5-2.	Chi-Squared Values for the Primary Side of the System for the Uncontrolled Rod Bank Withdrawal obtained with Inactive Controllers .....	13
Figure 6-1.	Chi-Squared Values for the Primary Side of the System for the Uncontrolled Rod Bank Withdrawal obtained with Active Controllers .....	14
Figure 6-2.	Chi-Squared Values for the Secondary Side of the System for the Uncontrolled Rod Bank Withdrawal obtained with Active Controllers .....	14
Figure 7.	Chi-Squared Values for the Secondary Side of the System for the 10% Step Load Change .....	42
Figure 8.	Pressurizer Setpoints .....	54
Figure 9.	Standard Deviations for the Input Parameters for Experiment A at 80% Power .....	66
Figure 10.	Standard Deviations for the Input Parameters for Experiment B .....	66
Figure 11.	Standard Deviations for the Input Parameters for Experiment C .....	67
Figure 12.	Standard Deviations for the Input Parameters for Experiment D .....	67
Figure 13.	Standard Deviations for the Input Parameters for Experiments A, B, C and D .....	68
Figure 14-1.	Standard Deviations for Average Fuel Temperature for RCP Trip using Experiment A at 80% Power for Data Assimilation .....	69
Figure 14-2.	Standard Deviations for Hot Channel Fuel Centerline Temperature for RCP Trip using Experiment A at 80% Power for Data Assimilation .....	69
Figure 14-3.	Standard Deviations for Hot Channel MDNBR for RCP Trip using Experiment A at 80% Power for Data Assimilation .....	70
Figure 15-1.	Standard Deviations for Average Fuel Temperature for Control Bank Withdrawal using Experiment B for Data Assimilation .....	70
Figure 15-2.	Standard Deviations for Hot Channel Fuel Centerline Temperature for Control Bank Withdrawal using Experiment B for Data Assimilation .....	71
Figure 15-3.	Standard Deviations for Hot Channel MDNBR for Control Bank Withdrawal using Experiment B for Data Assimilation .....	71
Figure 16-1.	Standard Deviations for Average Fuel Temperature for FCV Failed Open using Experiment C for Data Assimilation .....	72

Figure 16-2.	Standard Deviations for Hot Channel Fuel Centerline Temperature for FCV Failed Open using Experiment C for Data Assimilation .....	72
Figure 16-3.	Standard Deviations for Hot Channel MDNBR for FCV Failed Open using Experiment C for Data Assimilation.....	73
Figure 17-1.	Standard Deviations for Average Fuel Temperature for TCV Failed Open using Experiment D for Data Assimilation.....	73
Figure 17-2.	Standard Deviations for Hot Channel Fuel Centerline Temperature for TCV Failed Open using Experiment D for Data Assimilation .....	74
Figure 17-3.	Standard Deviations for Hot Channel MDNBR for TCV Failed Open using Experiment D for Data Assimilation .....	74
Figure 18-1.	Standard Deviations for Average Fuel Temperature for RCP Trip using Experiment A, B, C and D for Data Assimilation .....	75
Figure 18-2.	Standard Deviations for Hot Channel Fuel Centerline Temperature for RCP Trip using Experiment A, B, C and D for Data Assimilation.....	75
Figure 18-3.	Standard Deviations for Hot Channel MDNBR for RCP Trip using Experiment A, B, C and D for Data Assimilation .....	76
Figure 19-1.	Standard Deviations for Average Fuel Temperature for Control Bank Withdrawal using Experiment A, B, C and D for Data Assimilation.....	76
Figure 19-2.	Standard Deviations for Hot Channel Fuel Centerline Temperature for Control Bank Withdrawal using Experiment A, B, C and D for Data Assimilation ...	77
Figure 19-3.	Standard Deviations for Hot Channel MDNBR for Control Bank Withdrawal using Experiment A, B, C and D for Data Assimilation.....	77
Figure 20-1.	Standard Deviations for Average Fuel Temperature for FCV Failed Open using Experiment A, B, C and D for Data Assimilation.....	78
Figure 20-2.	Standard Deviations for Hot Channel Fuel Centerline Temperature for FCV Failed Open using Experiment A, B, C and D for Data Assimilation .....	78
Figure 20-3.	Standard Deviations for Hot Channel MDNBR for FCV Failed Open using Experiment A, B, C and D for Data Assimilation .....	79
Figure 21-1.	Standard Deviations for Average Fuel Temperature for TCV Failed Open using Experiment A, B, C and D for Data Assimilation.....	79
Figure 21-2.	Standard Deviations for Hot Channel Fuel Centerline Temperature for TCV Failed Open using Experiment A, B, C and D for Data Assimilation .....	80
Figure 21-3.	Standard Deviations for Hot Channel MDNBR for TCV Failed Open using Experiment A, B, C and D for Data Assimilation .....	80
Figure 22.	Each Parameter's Uncertainty Contribution to the System Attributes for RCP Trip.....	82
Figure 23.	Each Parameter's Uncertainty Contribution to the System Attributes for Control Bank Withdrawal.....	83
Figure 24.	Each Parameter's Uncertainty Contribution to the System Attributes for FCV Failed Open.....	84
Figure 25.	Each Parameter's Uncertainty Contribution to the System Attributes for TCV Failed Open.....	85

Figure 26.	Each Parameter's Uncertainty Contribution to the System Attributes for RCP Trip as a Result of Multiple Experiments .....	86
Figure 27.	Each Parameter's Uncertainty Contribution to the System Attributes for Control Bank Withdrawal as a Result of Multiple Experiments .....	87
Figure 28.	Each Parameter's Uncertainty Contribution to the System Attributes for FCV Failed Open as a Result of Multiple Experiments .....	88
Figure 29.	Each Parameter's Uncertainty Contribution to the System Attributes for TCV Failed Open as a Result of Multiple Experiments .....	89
Figure 30.	Accepted Input Parameter Vector Samples .....	91
Figure 31.	A posteriori distribution of the parameters using RCP Trip at 30% Power....	92
Figure 32.	A posteriori distribution of the parameters using RCP Trip at 80% Power....	95
Figure 33.	Inner Optimization using A Priori Design Margin .....	100
Figure 34.	Constraint Violation for Inner Optimization using A Priori Design Margin	101
Figure 35.	Inner Objective Function using All Experiments and Sensors for Data Assimilation .....	101
Figure 36.	Constraint Violation for Inner Objective Function using All Experiments and Sensors for Data Assimilation .....	102
Figure 37.	Objective Function for Outer Iteration .....	103
Figure 38.	System Responses obtained Simulating 100 Samples for 10% Step Load Changes at 70% Power using Control Algorithm F1Q1 for Uncertainty Analysis.....	109
Figure 39.	System Responses obtained Simulating 100 Samples for 10% Step Load Changes at 70% Power using Control Algorithm F3Q1 for Uncertainty Analysis.....	110
Figure 40.	System Responses obtained Simulating 100 Samples for 20% Ramp Load Changes at 70% Power using Control Algorithm F1Q1 for Uncertainty Analysis.....	111
Figure 41.	System Responses obtained Simulating 100 Samples for 20% Ramp Load Changes at 70% Power using Control Algorithm F3Q1 for Uncertainty Analysis.....	112

## 1. Introduction

### 1. 1. Overview of the IRIS Reactor System

IRIS (International Reactor Innovative and Secure) reactor system has been developed by an international consortium of twenty plus organization from nine countries with the original purpose of commercially deploying it in the next decade, but has since been abandoned. It is a 1000 MWt integral PWR which has eight helical steam generators, eight spool-type pumps, neutron reflector, pressurizer and control rod drive mechanism inside the reactor vessel [1]. The current design features of this small scale advanced light water reactor's vessel are presented in Figure 1. The primary system is contained in the reactor vessel and reactor coolant is pumped in a closed circuit in the vessel. The coolant goes up through the core, turns outward at the top of the internal, flows up to the eight primary pumps, is pumped downward through the pumps and through the steam generators, down the annulus between the core barrel and the reactor vessel wall, then upward through the core support assembly. Steam generator (SG) feedwater passes through the feedwater nozzles into the feedwater header, enters the steam generator tube and flows upward inside the tubes, first being heated to saturation, then boiled, and subsequently heated to dry superheated steam, which then flows into the upper steam discharge header and out through the steam outlet nozzles to the turbines. Both the SG feedwater and steam headers attach directly to the reactor vessel inside wall and form the primary to secondary pressure boundary.

One of the primary goals of the IRIS project is to complete the “safety by design.” First of all, it eliminates the Large Break Loss of Coolant Accident (LBLOCA) since the large loop

piping of conventional PWRs does not exist. This is the unique characteristic of the Small Modular Reactor (SMR). The large vessel per unit thermal energy compared to other PWRs provides a large coolant inventory in the reactor coolant system, which contributes to the more favorable IRIS responses to small and medium LOCAs. The large coolant inventory per unit thermal energy also provides a large heat sink that acts to effectively mitigate cooldown and heatup events. The IRIS once through steam generators with the primary coolant on the shell side provide reduced probability and consequences of the steam generator tube rupture accident. Another feature of IRIS once through steam generators is the limited secondary side water inventory, which reduces the consequences of cooldown event, e.g. steam line break. However, on the other hand, the limited inventory on the secondary side provides less mitigation to heatup events, e.g. feed line break. In this case, the large volume of the pressurizer compensates for the limited heat sink provided by the steam generators (The steam volume to reactor power ratio is five times larger in IRIS than in advanced passive PWRs). It is also obvious that multiple coolant pumps and steam generators mitigate single component failure accidents for the IRIS. As it is presented above, the primary goal of the IRIS project is designing a safe reactor in a simple and cost effective way.

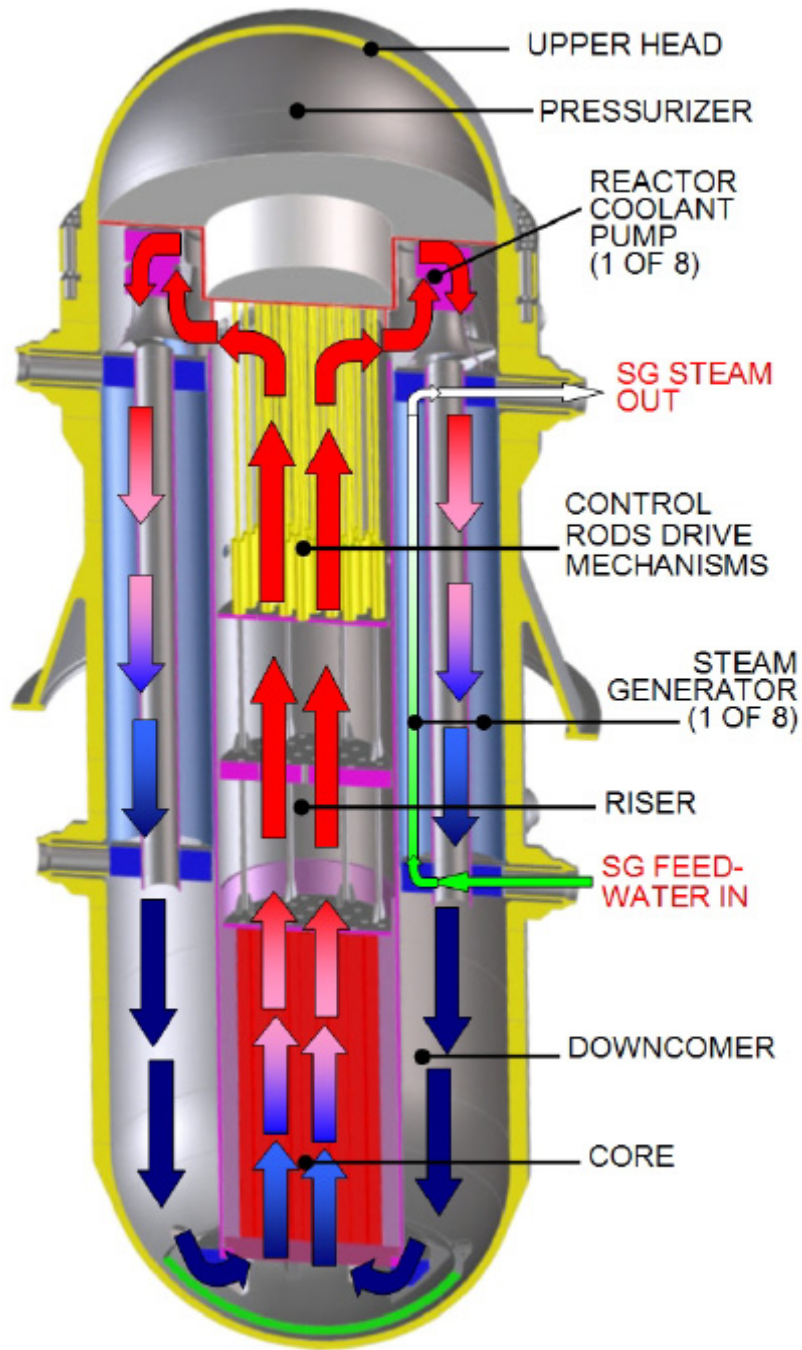


Figure 1. Layout of the IRIS Primary System

## 1. 2. Motivation

Estimating nuclear reactor performance during a transient has been the main issue in thermal hydraulic safety research since nuclear energy was first used to produce electricity. For the IRIS reactor that may be built and operated for the first time, simulation models have been developed and tested for the safety research using multiple thermal-hydraulic equations coupled to each other [2], [3]. The quality of the plant system simulator predictions will impact the reactor economy through the introduction of margins on the reactor design to ensure an operation, in which the safety and operational limits are satisfied with a high degree of certainty. How tight or relaxed these margins are depends on how accurate the predictions of reactor behavior are. The uncertainties of reactor simulator calculations are thus important to the determination of these margins. The IRIS research has been focused on a design that provides the highest degree of safety and cost effective arrangement. That is, by reducing uncertainties, safety can be maintained while costs are reduced.

The fidelity of the prediction cannot be evaluated directly unless the validation is performed using suitable measurements in nuclear plants. A great deal could be learned from experimental data to enhance simulation fidelity for a nuclear reactor. In particular, input parameters can be refined assuming it is the major source of uncertainties. Using adjusted thermal hydraulic input parameters and their reduced uncertainties, subsequent reactor simulation improves the prediction of key system attributes. The objective of this work is to reduce the uncertainties on limiting system attributes during accident transients. To accomplish this experiments are to be performed, data collected, and the data utilized to



complete data assimilation on the thermal-hydraulic input parameters to the system simulation code, in our case the IRIS system simulator. This was done by using the IRISN.Ver08.Mod06 [2] simulator developed at NC State to complete virtual experiments and generate their associated experimental data. This code predicts the performance of the IRIS reactor by solving multiple thermal hydraulic equations for both the primary and the secondary systems. The primary side responses, e.g. pressure, temperature, coolant flow rate, etc., are calculated based on the mass, momentum and internal energy equations, which are introduced in Appendix B. Historical research on the thermal hydraulic reactor system indicates that the system responses are usually nonlinear, which adds complexity to data assimilation. To determine whether the nonlinearities would exist for experiments performed at lower power initial conditions, and if so, utilize a data assimilation method capable of addressing nonlinearity, IRIS system simulations can be completed.

### **1. 3. Literature Review**

The uncertainty and sensitivity analysis for the thermal hydraulic reactor system has been widely performed for the uncertainty evaluation of the best estimate LOCA analysis. The best estimate plus uncertainty (BEPU) method was introduced and developed in the 1980s to support licensing. The code scaling, applicability, and uncertainty (CSAU) evaluation method was subsequently developed for application to the LBLOCA in a pressurized water reactor [4]. The CSAU methodology contains 14 steps organized into three major elements: Requirements and Code Capabilities, Assessment and Ranging of Parameters, and Sensitivity and Uncertainty Analysis. It was developed based upon 25 years of experimental data, and

included development of the embedded Phenomena Identification & Ranking Table (PIRT) methodology. The PIRT has become a standard accepted throughout the international nuclear community providing guidance in executing cost effective BEPU applications. In 1996, the USNRC approved a best estimate loss of coolant accident method based upon CSAU and the WCOBRA/TRAC thermal hydraulic code. Since the first uncertainty analysis performed with the CSAU method, several different methods have been proposed for uncertainty and sensitivity analysis. One of them is Uncertainty Analysis Methodology based on Accuracy Extrapolation (UMAE) which addresses model validation [5]. It is based on the extrapolation of the accuracy resulting from a comparison between the code predictions and the experimental data obtained in small scale facilities. Westinghouse developed a new BEPU method called Automated Statistical Treatment of Uncertainty Method (ASTRUM) which was approved in 2004 [6]. The ASTRUM is still based on the WCOBRA/TRAC thermal hydraulic code but it utilizes a non-parametric (distribution free) statistical sampling technique. Since it eliminates the superposition penalty associated with employing a surface response surrogate model, this technique is expected to reduce the predicted Peak Cladding Temperature (PCT). The BEMUSE (Best Estimate Method – Uncertainty and Sensitivity Evaluation) phase 3 benchmark assesses the reliable application of high quality best estimate and uncertainty and sensitivity evaluation methods [7]. It shows the method and results of the peak cladding temperature estimation conducted by ten participants from nine organizations and seven countries. The main characteristic of the approach used by participants is the propagation of the input parameters' uncertainties relying on probabilistic analysis associated with Wilks' formula, the non-parametric statistical sampling technique used in ASTRUM.

In Monte Carlo analysis, a probabilistic based sampling is used to develop a mapping from input parameters to system responses. Several possible sampling methods exist, including simple random sampling, stratified sampling and Latin Hypercube Sampling (LHS). Due to demanding calculation requirements, the Monte Carlo method is usually not applicable, particularly for data assimilation, to a large scale thermal hydraulic system simulation code. For the neutronic problem, a more deterministic approach has been used for the BEPU analysis. In order to deal with the reactor physics problem that has many more parameters than the thermal hydraulic problem has, adjoint sensitivity analysis was developed to reduce the calculational effort [8]. The adjoint method is known to be very powerful for a system that has multiple input parameters and a few responses, but sometimes inapplicable for the large scale thermal hydraulic system due to nonlinearity of the responses over their ranges of uncertainties. The Efficient Subspace Method (ESM) has also been developed for the neutronic problem utilizing Singular Value Decomposition (SVD) to deal with ill conditioned matrices [9], [10]. It was specifically developed for data assimilation for problems with both large parameter and response fields. Nowadays BEPU methods are widely used in the world and the industry is more focusing on development of new licensing BEPU methods. Even though many papers deal with the uncertainty evaluation methods, none of them presents the method which tremendously reduces the computing demand for thermal hydraulic system calculations. In addition, limited research has been conducted to value the benefits of performing additional experiments for the large scale thermal hydraulic

system associated with a power reactor, which can possibly reduce a posteriori uncertainties of the system attributes.

The work reported here presents data assimilation capabilities combined with an optimization technique developed to determine near-optimum thermal hydraulic experiments to perform on IRIS to minimize uncertainties in limiting reactor responses. This capability was developed such that the IRIS design was at the same time reoptimized to utilize the margin introduced. In chapter 2, the description of this analysis is presented. The methods that solve the nonlinear system based on the virtual experimental model using both deterministic and probabilistic methods are presented in sections 2.1 through 2.5. In section 2.6, the optimization methodology used to design the thermal hydraulic system of the IRIS is discussed. Following the discussion, the uncertainty analysis technique for the reactor control problem is presented in section 2.7. In chapter 3, results of data assimilation, optimization, and uncertainty analysis for the reactor control are provided to show the optimum design of the IRIS reactor achieved by reduced uncertainties on the reactor system. Following the results, conclusions and recommendations for future work are outlined in chapter 4. Finally, this dissertation includes appendices A and B providing several mathematical derivations. Appendix A shows the mathematical approach for data assimilation incorporating the parameter-response covariance matrix. In appendix B, the physical models for the primary side of the reactor are introduced, and the mathematical derivations for the numerical calculation of the primary side responses are presented.

## 2. Description of the Actual Work

### 2. 1. Linearity Test for the IRIS Reactor System

Since the preferred method for data assimilation and uncertainty quantification is dependent upon whether the observables, i.e. sensor signals, and attributes, e.g. Departure from Nucleate Boiling Ratio (DNBR), sensitivity equations are nearly linear or not, a Chi-Square test is required to confirm the system sensitivity equations linearity. For the Chi-Square goodness of fit, the observables and system attribute data are divided into K bins and the test statistic is defined as:

$$\chi^2 = \sum_{i=1}^K \frac{(O_i - E_i)^2}{E_i} \quad (2.1)$$

where  $O_i$  is the observed frequency for bin  $i$  and  $E_i$  is the expected frequency for bin  $i$ . If the sensitivity equations are linear and the parameters uncertainty distributions are Gaussian, the sensor and attribute distributions will also be Gaussian. Thus using a Gaussian distribution to obtain values for  $E_i$  and the IRIS simulator to obtain values of  $O_i$ , Chi-Square values can be obtained for the observables and attributes. One observes that not all observables and/or system attributes are within the desired level of the Chi-Square value, i.e. acceptable range of the linearity, if the reactor controllers are on and/or the transient is rapid. The reactor controllers that are associated with safety systems control certain observables, e.g. primary pressure, causing the reactor system to not behave naturally, which results in nonlinearity. Obviously the rapidness of the transients also causes the nonlinearity, e.g. RCP Trip. Note that the safety controllers, e.g. pressurizer heaters and feedwater controllers, could be turned on for certain transient, e.g. feedwater controllers are turned on for a step load

change. For further discussion of the Chi-Squared test, all of the samples are combined and presented in Figures 2 for a 10% step load change simulation. In order to see the impact of the pressurizer heaters on the system, all important control systems were turned off except the feedwater controllers and the pressurizer heaters. Figure 2 indicates that the pressurizer heater, which has a limited capacity as constrained by output capacity, is active during the transient. This causes nonlinearity in the primary pressure as shown in Figure 3 and 4-1. Some of the responses of the observables on the primary side could be affected by this nonlinearity as well. Since the minimum DNBR is a strong function of the system pressure, core flow rate, and coolant temperature, the hot channel minimum DNBR also shows nonlinearity. Similar to the safety control mechanism that produces a nonlinear primary pressure response, active feed pumps and feed control valves actions during the step load change result in nonlinearity that appears especially on the secondary side of the reactor system as shown in Figure 4-2.

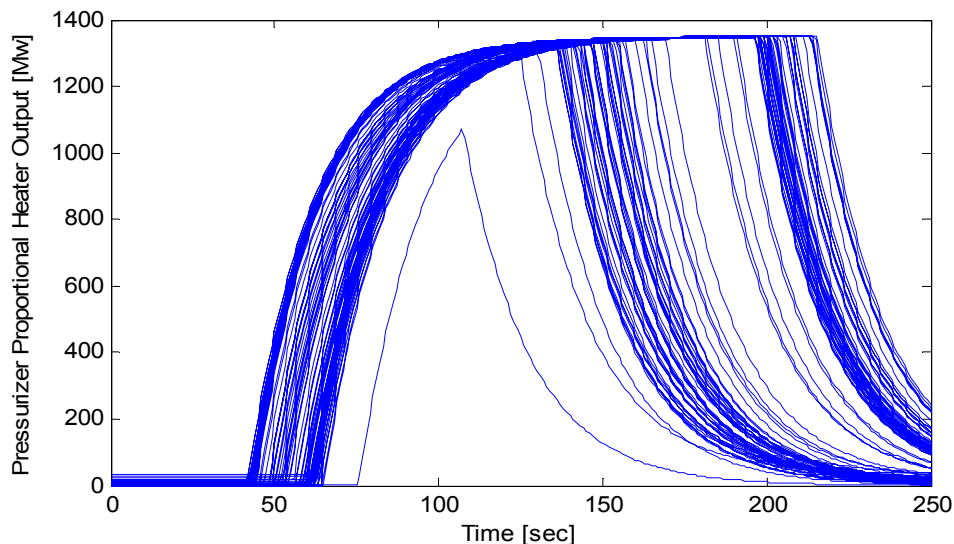


Figure 2. Pressurizer Heater Output

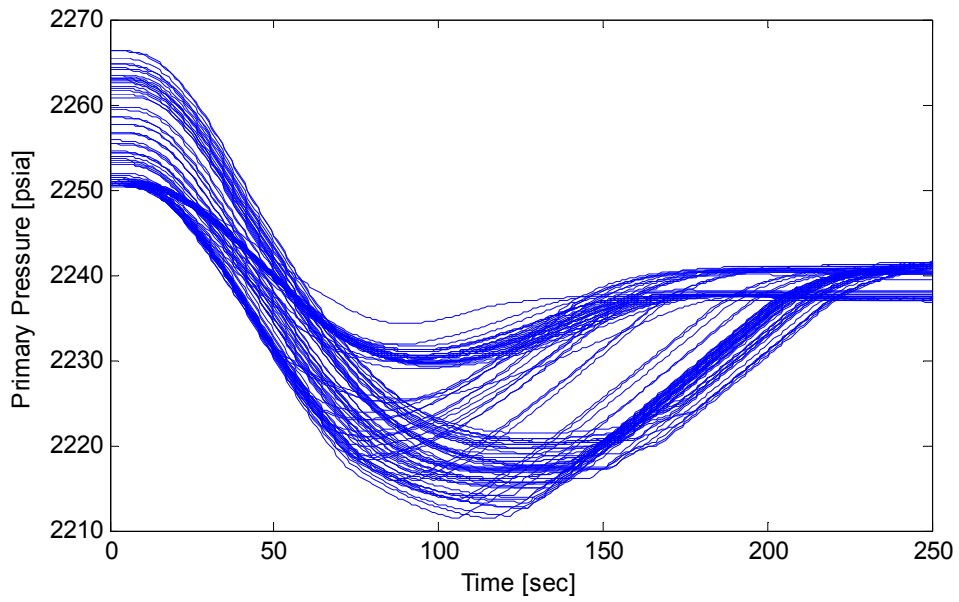


Figure 3. Primary Pressure

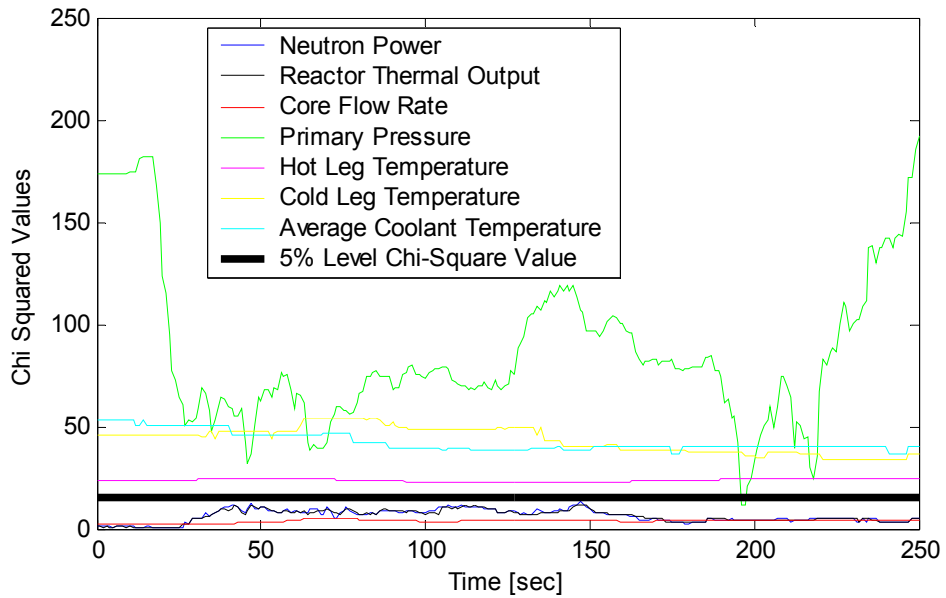


Figure 4-1. Chi-Squared Values for the Primary Side of the System for the 10% Step Load Change

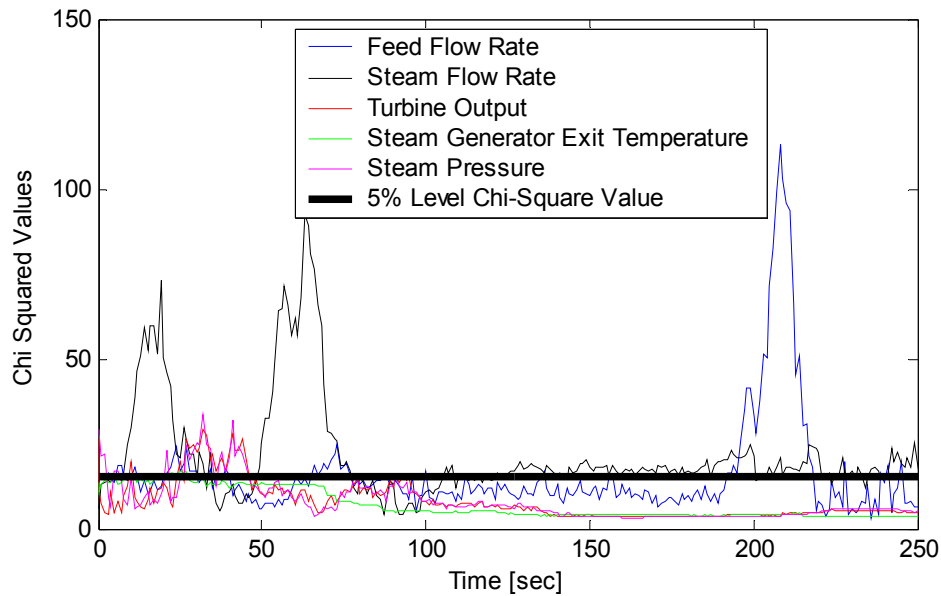


Figure 4-2. Chi-Squared Values for the Secondary Side of the System for the 10% Step Load Change

In order to simulate natural responses of the reactor system, IRIS simulations for several transients assuming inactive reactor controllers were completed for 100 samples of the parameters using Latin Hypercube sampling. Figure 5 illustrate the Chi-Squared values of the observables as a function of time for the uncontrolled rod bank withdrawal transient. With the safety controller, e.g. pressurizer heaters, as well as the reactor system controllers assumed to be turned off, the reactor system behaves naturally and the Chi-Square values for most observables and the system attributes decrease versus if these controllers are on (see Figure 6 for comparison).



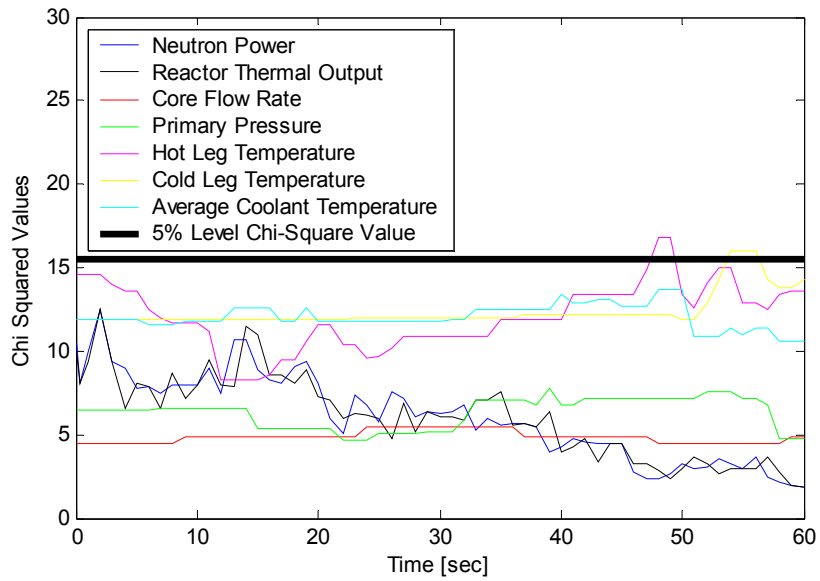


Figure 5-1. Chi-Squared Values for the Primary Side of the System for the Uncontrolled Rod Bank Withdrawal obtained with Inactive Controllers

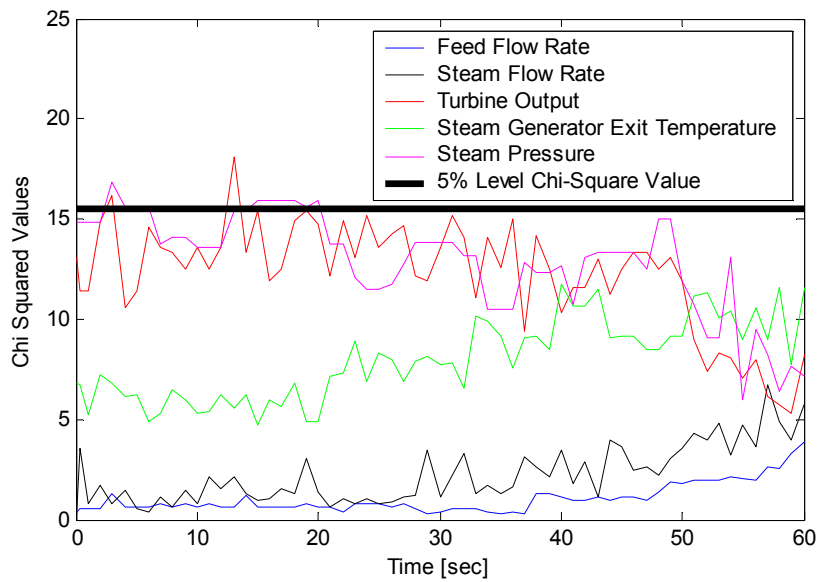


Figure 5-2. Chi-Squared Values for the Secondary Side of the System for the Uncontrolled Rod Bank Withdrawal obtained with Inactive Controllers

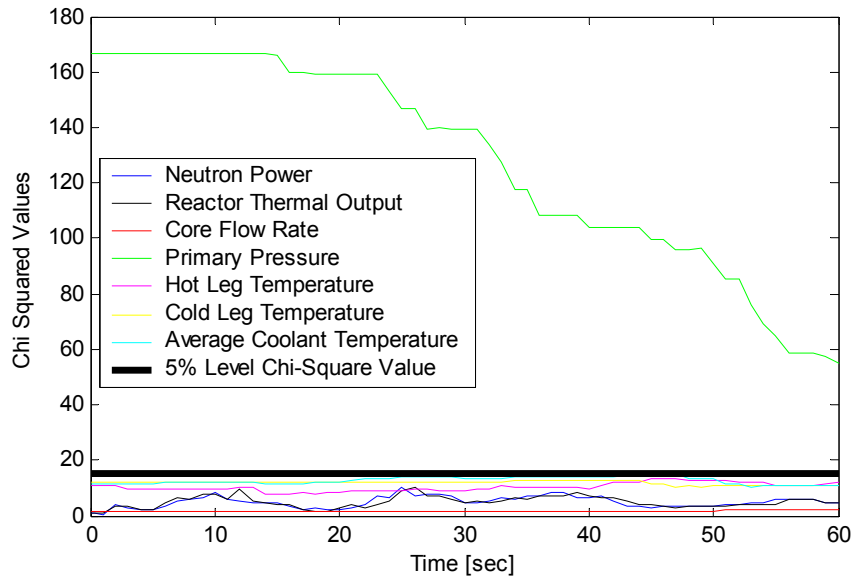


Figure 6-1. Chi-Squared Values for the Primary Side of the System for the Uncontrolled Rod Bank Withdrawal obtained with Active Controllers

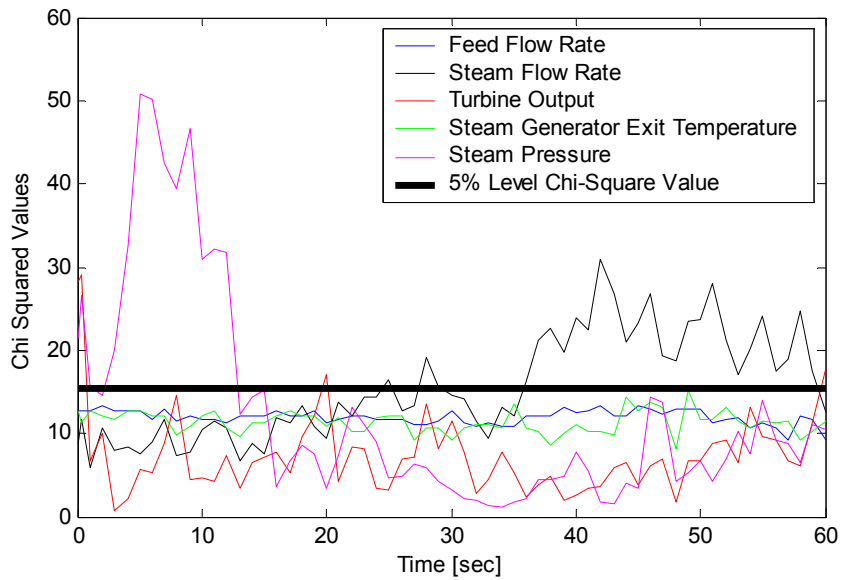


Figure 6-2. Chi-Squared Values for the Secondary Side of the System for the Uncontrolled Rod Bank Withdrawal obtained with Active Controllers

## 2. 2. Data Assimilation and Uncertainty Quantification

### 2.2.1. Deterministic Method for the Mildly Nonlinear Problems

Nuclear power plant design and operation must accommodate the uncertainties in predicting system performance, those uncertainties originated due to initial conditions, parameters, numerics and modeling uncertainties. Assuming that parameters' uncertainties are the major contributors to observables and attribute uncertainties compared to any other sources of uncertainties, they can be refined to develop a higher fidelity model. Using adjusted thermal hydraulic parameters and their reduced uncertainties, subsequent reactor simulation improves the prediction of key system attributes if closely related to the system observables. In order to accomplish this, given measurements of the observables and a priori distributions of the parameters, one solves an inverse problem adjusting the parameter values to achieve better agreement between measured and predicted sensor response values [11]. Since IRIS is not operational anywhere, to generate the experimental values of the observables a virtual reactor is employed. By this is implied that a computer simulation is used to predict the experimental values, where perturbed parameter values have been used that are consistent with their uncertainties.

The distribution of the parameters (assumed Gaussian), whose mean is  $\bar{p}_0$  and whose covariance matrix is  $\bar{C}_p$ , is given by:

$$\rho(\bar{p}) = C_1 \exp \left[ -\frac{1}{2} \left\{ \frac{\bar{p} - \bar{p}_0}{\bar{p}_0} \right\}^T \bar{C}_p^{-1} \left\{ \frac{\bar{p} - \bar{p}_0}{\bar{p}_0} \right\} \right] = C_1 \exp \left[ -\frac{1}{2} \{ \bar{p} - \bar{p}_0 \}^T \bar{C}_p^{-1} \{ \bar{p} - \bar{p}_0 \} \right] \quad (2.2)$$

where  $\bar{p} \equiv \bar{p}/\bar{p}_0$  implying  $\bar{p}$  are relative values with respect to the a priori parameters value, and  $\bar{p}_0$  is the unit vector. The constant  $C_1$  serves as the normalization constant valued such the  $\rho(\bar{p})$  when integrated over all  $\bar{p}$  values equals 1.0. Note that an overline indicates a vector and a double overline denotes a matrix. In general, the expectation of function  $f(\bar{x})$ , denoted as  $\langle f(\bar{x}) \rangle$ , is defined as:

$$\langle f(\bar{x}) \rangle \equiv \int_{S_{\bar{x}}} f(\bar{x}) P(\bar{x}) d\bar{x} \quad (2.3)$$

where  $S_{\bar{x}}$  represents the space formed by all possible values of  $\bar{x}$ .  $P(\bar{x})$  is recognized as a joint probability density function. The first moment, i.e.  $f(\bar{x}) = \bar{x}$ , renders the mean value, and the second moment, i.e.  $f(\bar{x}) = [\bar{x} - \langle \bar{x} \rangle][\bar{x} - \langle \bar{x} \rangle]^T$ , renders the covariance matrix.

Using these generalized definitions, the a priori parameter covariance matrix is defined as follows:

$$\bar{\bar{C}}_p^{prior} \equiv \left\langle [\bar{p} - \bar{p}_0][\bar{p} - \bar{p}_0]^T \right\rangle = \int_{S_p} [\bar{p} - \bar{p}_0][\bar{p} - \bar{p}_0]^T \rho(\bar{p}) d\bar{p} \quad (2.4)$$

where  $S_p$  is the parameter space.

The sampling model for the observations whose uncertainties can be represented by a Gaussian probability distribution centered at  $\bar{r}$  and with experimental uncertainty covariance matrix  $\bar{\bar{C}}_m$  is:

$$\rho(\bar{r}_m | \bar{r}) = C_2 \exp \left[ -\frac{1}{2} \{ \bar{r}_m - \bar{r} \}^T \bar{C}_m^{-1} \{ \bar{r}_m - \bar{r} \} \right] \quad (2.5)$$

where,  $\bar{r}_m$  and  $\bar{r}$  denote the virtual experiment sensor signal vector and the mean value vector (taken as the design (simulator) model prediction vector), respectively, with the  $\bar{p}$  dependence of  $\bar{r}$  suppressed. The constant  $C_2$  is again the normalization constant. In this work,  $\bar{C}_m$  is assumed diagonal and variance values set to those typical of nuclear power plant sensors. Note that to obtain the virtual reactor sensor signals accounting for observation uncertainty, observation errors are applied to the virtual reactor simulators predicted signal values,  $\bar{r}_m$ . The virtual experiments that were modeled are presented in section 2.3. For  $J$  distinct sensors and  $T$  discrete times each system response vector  $\bar{r}_j$  can be represented as follows:

$$\bar{r}_j = \{ r_j^{(t)} | t = 1, 2, \dots, T \} \quad (2.6)$$

Then the vector  $\bar{r}$  which contains all of the system responses is:

$$\bar{r} = \begin{bmatrix} \bar{r}_1^T & \bar{r}_2^T & \dots & \bar{r}_J^T \end{bmatrix}^T \quad (2.7)$$

If the system is linear or mildly nonlinear, the design model can be linearized by the following first-order Taylor series expansion:

$$\bar{r} \cong \bar{r}(\bar{p}_0) + \left( \bar{S} \right)_{\bar{p}_0} \delta \bar{p} = \bar{r}_0 + \left( \bar{S} \right)_{\bar{p}_0} \delta \bar{p} \quad (2.8)$$

where  $\left(\overline{S}\right)_{\overline{p}_0}$  is the time dependent sensitivity matrix computed about the nominal value of the a priori parameters and  $\delta \overline{p} \triangleq \overline{p} - \overline{p}_0$ . Using the a priori distribution of the parameters, the a priori system attribute covariance can be calculated by the sandwich rule as follows:

$$\begin{aligned}
\overline{C}_a^{prior} &\equiv \left\langle \left[ \overline{a} - \langle \overline{a} \rangle \right] \left[ \overline{a} - \langle \overline{a} \rangle \right]^T \right\rangle \\
&= \left\langle \left[ \overline{a} - \overline{a}_0 \right] \left[ \overline{a} - \overline{a}_0 \right]^T \right\rangle \\
&= \left\langle \left( \overline{S}_a \right)_{\overline{p}_0} \delta \overline{p}_0 \delta \overline{p}_0^T \left( \overline{S}_a \right)_{\overline{p}_0}^T \right\rangle \\
&= \left( \overline{S}_a \right)_{\overline{p}_0} \overline{C}_p^{prior} \left( \overline{S}_a \right)_{\overline{p}_0}^T
\end{aligned} \tag{2.9}$$

where  $\overline{a} \cong \overline{a}(\overline{p}_0) + \left( \overline{S}_a \right)_{\overline{p}_0} \delta \overline{p} = \overline{a}_0 + \left( \overline{S}_a \right)_{\overline{p}_0} \delta \overline{p}$

Following the Bayesian approach, a posteriori distribution for the parameter vector  $\overline{p}$  is then given by:

$$\begin{aligned}
\rho(\overline{p} | \overline{r}_m) &= \frac{\rho(\overline{r}_m | \overline{r}(\overline{p})) \times \rho(\overline{p})}{\rho(\overline{r}_m)} \\
&= \frac{\rho(\overline{r}_m | \overline{p}) \times \rho(\overline{p})}{\int_{S_p} \rho(\overline{r}_m | \overline{p}) d\overline{p}} \\
&= C_3 \exp \left[ -\frac{1}{2} \left( \left\{ \overline{r}_m - \overline{r}(\overline{p}) \right\}^T \overline{C}_m^{-1} \left\{ \overline{r}_m - \overline{r}(\overline{p}) \right\} + \left\{ \overline{p} - \overline{p}_0 \right\}^T \overline{C}_p^{-1} \left\{ \overline{p} - \overline{p}_0 \right\} \right) \right]
\end{aligned} \tag{2.10}$$

In order to determine the parameter vector that maximizes the Gaussian distribution, i.e. the mean values of the parameters, the parameter vector that minimizes the following expression is sought.

$$\left[ \{\bar{r}_m - \bar{r}(\bar{p})\}^T \bar{C}_m^{-1} \{\bar{r}_m - \bar{r}(\bar{p})\} + \{\bar{p} - \bar{p}_0\}^T \bar{C}_p^{-1} \{\bar{p} - \bar{p}_0\} \right] \quad (2.11)$$

In general, the minimization problem can be formulated with the parameter-response combined vector  $\bar{z}$  and the corresponding block covariance matrix  $\bar{C}$  as follows [12]:

$$\bar{z} \equiv \begin{bmatrix} \bar{p} - \bar{p}_0 \\ \bar{r} - \bar{r}_m \end{bmatrix}, \quad \bar{C} = \begin{bmatrix} \bar{C}_p & \bar{C}_{pr} \\ \bar{C}_{rp} & \bar{C}_m \end{bmatrix} \quad (2.12)$$

where,  $\bar{C}_{pr} = \bar{C}_{rp}^T$  is the parameter-response covariance matrix. This correlation occurs due to the successive linearization iterations one utilizes in solving the weakly nonlinear data assimilation problem, associated with updating the observables sensitivity matrix as updated parameter values become available. If the a priori distribution for the parameters and for the sampling model can be represented by a Gaussian distribution and the system responses are linear to the parameters, then the Gaussian probability density function describes the posteriori uncertainty of  $\bar{p}$ .

$$\rho(\bar{p} | \bar{r}_m) = const \cdot \exp \left\{ -\frac{1}{2} \bar{z}^T \bar{C}^{-1} \bar{z} \right\} \quad (2.13)$$

The mathematical approach for this analysis is presented in Appendix A. Since the thermal-hydraulic reactor system model is not highly nonlinear, the a posteriori parameters approach the converged solution quickly and their uncertainties significantly decrease after the first iteration. This makes the parameter adjustments associated with the second linearization iteration small; furthermore, significantly reduced uncertainties of the parameters after the first iteration will cause small parameter-response uncertainties as well. Thus, adding the parameter-response uncertainties does not affect very much the solution to the IRIS thermal-

hydraulic inverse problem [13]. Solution to the minimization problem is then accomplished by differentiating expression (2.11) with respect to  $\bar{p}$ .

Generalizing, the problem can also include a regularization parameter,  $\alpha$ , to address any ill-conditioning and to control the amount of parameter adjustments allowed. Thus the minimization problem becomes:

$$\min_p \left[ \{\bar{r}_m - \bar{r}(\bar{p})\}^T \bar{C}_m^{-1} \{\bar{r}_m - \bar{r}(\bar{p})\} + \alpha^2 \{\bar{p} - \bar{p}_0\}^T \bar{C}_p^{-1} \{\bar{p} - \bar{p}_0\} \right] \quad (2.14)$$

The first term in this equation is the mismatch term between the virtual experiment sensor readings and the design model predictions. The second term in the equation is the regularization term, which shows the change in a priori to a posteriori values of the parameters with respect to the matrix norm of the parameters covariance matrix. Tikhonov regularization [14] was employed, where the weighting sum of the mismatch term and regularization term is minimized by selection of the posteriori input parameter values. The regularization parameter indicates the degree of weighting between the mismatch term and the regularization term. For large  $\alpha$  values, a posteriori parameter values will not deviate greatly from their a priori values. This implies the mismatch term will not be reduced very much by data assimilation. For small alpha values, the reverse behavior occurs. The Tikhonov regularization parameter was selected experimentally based on the characteristic L-curve [15]. For a Bayesian approach, one would set  $\alpha = 1$  to produce unbiased a posteriori values. Assuming linearity of the sensitivity equations, the a posteriori parameter vector is obtained without the parameter-response uncertainties as follows [16]:



$$\bar{p}_0^{post} = \bar{p}_0 + \left[ \bar{S}^T \bar{C}_m \bar{S} + \alpha^2 \bar{C}_p \right]^{-1} \bar{S}^T \bar{C}_m \left[ \bar{r}_m - \bar{r}_0 \right] \quad (2.15)$$

and a posteriori system responses and attributes are given as:

$$\bar{r}^{post} \cong \bar{r}(\bar{p}_0^{post}) + \left( \bar{S} \right)_{\bar{p}_0^{post}} \delta \bar{p}^{post} = \bar{r}_0^{post} + \left( \bar{S} \right)_{\bar{p}_0^{post}} \delta \bar{p}^{post} \quad (2.16)$$

and

$$\bar{a}^{post} \cong \bar{a}(\bar{p}_0^{post}) + \left( \bar{S}_a \right)_{\bar{p}_0^{post}} \delta \bar{p}^{post} = \bar{a}_0^{post} + \left( \bar{S}_a \right)_{\bar{p}_0^{post}} \delta \bar{p}^{post} \quad (2.17)$$

respectively. The a posteriori parameter covariance matrix can be also computed by:

$$\bar{C}_p^{post} \cong \left\langle \left[ \bar{p} - \bar{p}_0^{post} \right] \left[ \bar{p} - \bar{p}_0^{post} \right]^T \right\rangle \quad (2.18)$$

Substituting Equation (2.15) for the posteriori parameters into Equation (2.18) produces the

following expression for  $\bar{C}_p^{post}$  :

$$\begin{aligned} \bar{C}_p^{post} = & \left\langle \left[ \bar{p} - \bar{p}_0 - \left\{ \bar{S}^T \bar{C}_m \bar{S} + \alpha^2 \bar{C}_p \right\}^{-1} \bar{S}^T \bar{C}_m \left\{ \bar{r}_m - \bar{r}_0 \right\} \right] \right. \\ & \left. \times \left[ \bar{p} - \bar{p}_0 - \left\{ \bar{S}^T \bar{C}_m \bar{S} + \alpha^2 \bar{C}_p \right\}^{-1} \bar{S}^T \bar{C}_m \left\{ \bar{r}_m - \bar{r}_0 \right\} \right]^T \right\rangle \end{aligned}$$

$$\begin{aligned}
&= \overline{\overline{C_p}}^{prior} - \left\langle \left[ \overline{\overline{p}} - \overline{\overline{p_0}} \right] \left[ \overline{\overline{r_m}} - \overline{\overline{r}} + \overline{\overline{S}} \left( \overline{\overline{p}} - \overline{\overline{p_0}} \right) \right]^T \right\rangle \overline{\overline{C_m}} \overline{\overline{S}} \left[ \overline{\overline{S}} \overline{\overline{C_m}} \overline{\overline{S}} + \alpha^2 \overline{\overline{C_p}} \right]^{-T} \\
&\quad - \left[ \overline{\overline{S}} \overline{\overline{C_m}} \overline{\overline{S}} + \alpha^2 \overline{\overline{C_p}} \right]^{-1} \overline{\overline{S}} \overline{\overline{C_m}} \left\langle \left[ \overline{\overline{r_m}} - \overline{\overline{r}} + \overline{\overline{S}} \left( \overline{\overline{p}} - \overline{\overline{p_0}} \right) \right] \left[ \overline{\overline{p}} - \overline{\overline{p_0}} \right]^T \right\rangle \\
&\quad + \left[ \overline{\overline{S}} \overline{\overline{C_m}} \overline{\overline{S}} + \alpha^2 \overline{\overline{C_p}} \right]^{-1} \overline{\overline{S}} \overline{\overline{C_m}} \\
&\quad \times \left\langle \left[ \overline{\overline{r_m}} - \overline{\overline{r}} + \overline{\overline{S}} \left( \overline{\overline{p}} - \overline{\overline{p_0}} \right) \right] \left[ \overline{\overline{r_m}} - \overline{\overline{r}} + \overline{\overline{S}} \left( \overline{\overline{p}} - \overline{\overline{p_0}} \right) \right]^T \right\rangle \\
&\quad \times \overline{\overline{C_m}} \overline{\overline{S}} \left[ \overline{\overline{S}} \overline{\overline{C_m}} \overline{\overline{S}} + \alpha^2 \overline{\overline{C_p}} \right]^{-T} \\
&= \overline{\overline{C_p}}^{prior} + \left[ \overline{\overline{C_{pr}}} - \overline{\overline{C_p}} \overline{\overline{S}} \right] \overline{\overline{C_m}} \overline{\overline{S}} \left[ \overline{\overline{S}} \overline{\overline{C_m}} \overline{\overline{S}} + \alpha^2 \overline{\overline{C_p}} \right]^{-T} \\
&\quad + \left[ \overline{\overline{S}} \overline{\overline{C_m}} \overline{\overline{S}} + \alpha^2 \overline{\overline{C_p}} \right]^{-1} \overline{\overline{S}} \overline{\overline{C_m}} \left[ \overline{\overline{C_{rp}}} - \overline{\overline{S}} \overline{\overline{C_p}} \right] \\
&\quad + \left[ \overline{\overline{S}} \overline{\overline{C_m}} \overline{\overline{S}} + \alpha^2 \overline{\overline{C_p}} \right]^{-1} \\
&\quad \times \overline{\overline{S}} \overline{\overline{C_m}} \left[ \overline{\overline{C_m}} - \overline{\overline{C_{rp}}} \overline{\overline{S}} - \overline{\overline{S}} \overline{\overline{C_{pr}}} + \overline{\overline{S}} \overline{\overline{C_p}} \overline{\overline{S}} \right] \overline{\overline{C_m}} \overline{\overline{S}} \\
&\quad \times \left[ \overline{\overline{S}} \overline{\overline{C_m}} \overline{\overline{S}} + \alpha^2 \overline{\overline{C_p}} \right]^{-T} \\
&\cong \overline{\overline{C_p}}^{prior} - \overline{\overline{C_p}} \overline{\overline{S}} \overline{\overline{C_m}} \overline{\overline{S}} \left[ \overline{\overline{S}} \overline{\overline{C_m}} \overline{\overline{S}} + \alpha^2 \overline{\overline{C_p}} \right]^{-T} - \left[ \overline{\overline{S}} \overline{\overline{C_m}} \overline{\overline{S}} + \alpha^2 \overline{\overline{C_p}} \right]^{-1} \overline{\overline{S}} \overline{\overline{C_m}} \overline{\overline{S}} \overline{\overline{C_p}} \\
&\quad + \left[ \overline{\overline{S}} \overline{\overline{C_m}} \overline{\overline{S}} + \alpha^2 \overline{\overline{C_p}} \right]^{-1} \overline{\overline{S}} \overline{\overline{C_m}} \left[ \overline{\overline{C_m}} + \overline{\overline{S}} \overline{\overline{C_p}} \overline{\overline{S}} \right] \overline{\overline{C_m}} \overline{\overline{S}} \left[ \overline{\overline{S}} \overline{\overline{C_m}} \overline{\overline{S}} + \alpha^2 \overline{\overline{C_p}} \right]^{-T}
\end{aligned} \tag{2.19}$$

As noted earlier, to address mild nonlinearity, sensitivity coefficient values were redetermined linearizing about the previous iteration a posteriori parameter values, and inverse theory was once again used to obtain updated a posteriori parameters values. These linearization iterations were continued until a stopping criteria was satisfied.

Best-estimate accident analysis requires not only values of limiting system attributes during accident transients, e.g. Minimum Departure from Nucleate Boiling Ratio (MDNBR), but also their uncertainties. To obtain those, given a posteriori parameter uncertainties, one can propagate the parameter uncertainties through the simulation model to predict a posteriori uncertainties on core observables and system attributes. If the a posteriori parameter uncertainties are Gaussian and the system responds linearly over the range of the parameter uncertainties, the system attribute uncertainties are Gaussian, which is characterized by the mean values and covariance at the operating power level for the accident “acc” given by:

$$\left( \overline{C}_a^{acc\ post} \right)^o = \left( \overline{S}_a^{acc} \right)_{p_0}^o \overline{C}_p^{post} \left( \overline{S}_a^{acc} \right)_{p_0}^{oT} \quad (2.20)$$

where  $\left( \overline{S} \right)^o$  denotes the sensitivity matrix at operating power. If the system is highly nonlinear, one should propagate parameter uncertainties by Monte Carlo simulation. As done in this work, data assimilation was completed using experiments conducted mostly at lower powers, since experiments actually corresponding to higher power accident conditions would be prohibited. In this case, one should always pay attention to the similarity of physics. If the physics at operating power is significantly different from that at lower power, the calculated a posteriori system attribute uncertainty would in general not represent that associated with the actual transient starting at operating power. Thus the similarity of physics should always be demonstrated if possible when completing an uncertainty analysis.

Literature reviews were completed to identify the uncertainties on parameters and correlations within the model, and which system responses and attributes would need to be considered. The following parameters/correlations [4], [17], [18], [19] were selected to have their values adjusted via data assimilation:

1. Chen Heat Transfer Correlation for nucleate boiling heat transfer coefficient on the secondary side of steam generator
2. Dittus-Boelter Heat Transfer Correlation for single phase (liquid or gas) heat transfer coefficient on the secondary side of steam generator
3. Fuel Thermal Conductivity
4. Friction Factors
5. Gap Conductance
6. Pellet Diameter
7. Cladding Diameter
8. Cladding Thermal Conductivity
9. Pump Head (RCP and FP)
10. Moderator Temperature Coefficient

The following observables were selected for usage during data assimilation:

1. Neutron Power
2. Reactor Thermal Output
3. Core Flow Rate
4. Primary Pressure
5. Hot Leg Temperature

6. Cold Leg Temperature
7. Average Coolant Temperature
8. Feed Flow Rate per Steam Generator
9. Steam Flow Rate per Steam Generator
10. Turbine Output
11. Steam Generator Exit Temperature
12. Steam Pressure

In addition the following system attributes were selected for uncertainty quantification:

1. Average Reactor Fuel Temperature
2. Hot Channel Fuel Center Line Temperature
3. Hot Channel Minimum Departure from Nucleate Boiling Ratio

Table I. Uncertainties of Observables

Observables	Measurement Uncertainties ( $1\sigma$ )
Neutron Power	2%
Reactor Thermal Output	2%
Core Flow Rate	2.74%
Primary Pressure	18.2 psia
Hot Leg Temperature	2.43 F
Cold Leg Temperature	2.43 F
Average Coolant Temperature	2.43 F
Feed Flow Rate per Steam Generator	1.6%
Steam Flow Rate per Steam Generator	1.6%
Turbine Output	2%
Steam Generator Exit Temperature	2% (assumed)
Steam Pressure	2% (assumed)

Table I presents the sensors' uncertainties employed, which are based upon the instrumentation used in operating PWRs [30]. In addition, calculations were also completed using a larger uncertainty on core flow rate, 6%, since it was judged that with an integral PWR this uncertainty would be larger than for loop configured PWR.

### 2.2.2. MCMC Method for the Nonlinear Problems

All of the above discussion is based upon the parameters and observables uncertainties being Gaussian and the system sensitivity equations being mildly nonlinear i.e. nearly linear. However according to the linearity test, nonlinear behaviors were observed at the lower power experimental condition, especially on the secondary side of the reactor. The deterministic approach, based upon a first order truncated Taylor series representation for the responses, to uncertainty analysis is inappropriate to treat this behavior due to the nonlinear relationship between the system responses and the parameters, hence the potential non-Gaussian nature of the a posteriori distribution. This provides motivation that the transients that generate nonlinear system responses be differentiated from those that behave relatively linearly. To address the nonlinear responses in both data assimilation and determining the a posteriori uncertainties of the parameters, the following approach was employed.

Following the Bayesian approach, a posteriori distribution for the parameter vector  $\bar{p}$  is then given by Equation (2.10). If the system observables are linear with respect to the parameters, then solutions to the inverse problem could be obtained analytically as presented in section 2.2.1. If the system observables are nonlinear with respect to the parameters for certain

transients, given a priori parameter uncertainty information, one needs to propagate the parameter uncertainties through the simulation model to predict the a posteriori uncertainties of the parameters using Monte Carlo simulations [20]. This is conducted using the Markov Chain Monte Carlo (MCMC) method which seeks to determine the steady-state Markov distribution by generating Markov chains, which coincides with the target distribution, i.e. the a posteriori distribution of the parameters. A simple MCMC implementation uses the Metropolis algorithm which is presented as follows:

1. Initialize the parameter vector by guessing it at some value.
2. Given the current parameter vector is  $\bar{p}^i$ , generate a new parameter vector  $\bar{p}^*$  in  $\left[ \bar{p}^i - \bar{m}, \bar{p}^i + \bar{m} \right]$ , where  $\bar{m}$  is a random number vector.
3. Compute the Metropolis acceptance probability using the following expression:

$$\alpha = \min \left\{ 1, \frac{\rho(\bar{p}^* | \bar{r}_m)}{\rho(\bar{p}^i | \bar{r}_m)} \right\}$$

4. Define  $\bar{p}^{i+1} = \begin{cases} \bar{p}^* & \text{with probability } \alpha \\ \bar{p}^i & \text{with probability } 1 - \alpha \end{cases}$  selecting which value to assign via a random number [0,1]
5. Return to step 2.

At the beginning of the sequence, one needs to run MCMC for awhile to achieve convergence to the target probability density function (pdf). After convergence, one

considers a certain number of the first iterations to be discarded as the burn in stage to remove the bias from the initially chosen starting point. The size of the perturbation, i.e. the trial space, can be adapted during the burn in phase to a value that provides a desired acceptance percentage. It has been claimed that, for a wide variety of problems, acceptance probability near 50% indicates that the chain has good mixing [21], [22], [23]. When the percentage is less than 30%, i.e. when the trial space is much larger than the target space, the  $\bar{p}^i$  does not move for long periods, but jumps are large, which implies that one should perform a large number of simulations to obtain a reasonable number of accepted samples that illustrate the a posteriori. When the percentage is more than 70%, i.e. when the trial space is much smaller than the target space, movement across the target pdf is slow, so called unconstrained random walk, and will not efficiently span the full range of the target distribution unless the total number of trials is extremely large. In both cases the MCMC simulation is computationally time consuming since the total number of trials should be sufficiently large to estimate the a posteriori distribution properly. When simulations do not provide the desired acceptance percentage, it is possible to improve mixing by properly adjusting the trial space. Various heuristic rules have been suggested for fixing these problems during a simulation by monitoring the frequency of acceptances in the simulation. While the Metropolis algorithm is running, one can monitor the frequency of acceptances of the Metropolis algorithm; if the acceptance rate is much less or much more than 50%, one can alter the size of the perturbation by decreasing or increasing its trial space, respectively.



MCMC has proven effective for nonlinear response problems with multiple parameters to adjust. However this method is not applicable if there are many parameters and the simulation model requires substantial CPU time to execute due to the computational burden.

### **2. 3. Virtual Experiments**

Data assimilation and uncertainty quantification were completed by defining the experiments, defining the limiting accidents, and determining the a posteriori uncertainties of the key system attributes for the limiting accidents. In order to identify the limiting accidents, the Updated Final Safety Analysis Report (UFSAR) [24] and IRIS Preliminary Safety Assessment Report [25] were reviewed. Simulations were performed to determine virtual sensor signals which are surrogates for unavailable experimental values. A single sample of all the parameter values was used to determine the perturbed parameter values for the virtual reactor (simulator), from which the virtual reactor sensors' readings were obtained. In order to adjust parameters, the following four experiments were simulated using the IRIS system simulation code.

#### **A. Reactor Coolant Pump (RCP) Trip at 30 % and 80% Power**

The simulation is performed for 8 seconds. As mass flow rate decreases below Low Reactor Coolant Flow Trip Set Point, control rods are inserted and the reactor trips. All control systems and safety controllers are assumed to be inactive. Note that RCP trip at 80% power would not be allowed since it is performed at too high a power level, but the simulation was

done at relatively high power level to compare the result with that of RCP trip at a lower power and to minimize computation induced noise from the simulator.

#### B. Control Bank Withdrawal at 70% Power

The simulation is performed for 60 seconds. The control rod worth was assumed to be  $0.893\% \Delta\rho$ . The maximum power reached during the transient is slightly below 845 MWt which is approximately 85% of the operating power and 113% of the nominal power at 70% power level. The simulation shows that the reactor does not trip during the experiment since the large volume of the pressurizer accommodates the primary water volume increase due to the limited heat sink (The pressurizer steam volume to reactor power ratio is five times larger in IRIS than in current PWRs). All important control systems are assumed to be inactive except the control bank.

#### C. Feed Control Valve (FCV) Failed Open at 15% Power

The simulation is performed for 120 seconds. The feed control valve position is assumed to experience a +3% step change. All control systems and safety controllers are assumed to be inactive.

#### D. Turbine Control Valve (TCV) Failed Open at 15% Power

The simulation is performed for 120 seconds. The turbine control valve position changes from the initial value of 5% to the final value of 10%. All control systems and safety controllers are assumed to be inactive.

## 2. 4. Uncertainty Contribution to the System Attributes

Since identifying major sources of uncertainty, as done in this work, is important in deciding where additional efforts should be given to reduce these uncertainties, each parameter's uncertainty contribution to the system attributes was determined as well. This was evaluated for a specific parameter's uncertainty contribution by determining the system attribute's uncertainty propagated from all parameters and subtracting that obtained by propagating from all but the specific parameter of interest. The associated mathematical derivation is now given.

Assuming no uncertainty for parameter  $\alpha_k$ , the joint distribution function between  $\alpha_k$  and  $\alpha_j$  is defined using a Dirac-delta function.

$$P(\alpha_k, \alpha_j) = \delta(\alpha_k - \langle \alpha_k \rangle) P(\alpha_j) \quad (2.21)$$

The  $(k, j)$  elements of a posteriori parameter covariance matrix are then zeros for all  $j$  s.

$$\left( \overline{C}_p^{post} \right)_{k,j} = \int_{S_{\alpha_j}} \int_{S_{\alpha_k}} (\alpha_k - \langle \alpha_k \rangle) (\alpha_j - \langle \alpha_j \rangle) \delta(\alpha_k - \langle \alpha_k \rangle) P(\alpha_j) d\alpha_k d\alpha_j = 0 \quad (2.22)$$

Likewise  $\left( \overline{C}_p^{post} \right)_{i,k}$  are zeros for all  $i$  s. Thus the matrix  $\left( \overline{C}_p^{post} \right)_k$  which does not account for uncertainty on  $\alpha_k$  is defined as:

$$\left(\overline{\overline{C}}_p^{post}\right)_k \equiv \begin{bmatrix} c_{1,1} & c_{1,2} & \cdots & c_{1,k-1} & 0 & c_{1,k+1} & \cdots & c_{1,Np} \\ c_{2,1} & c_{2,2} & \cdots & c_{2,k-1} & 0 & c_{2,k+1} & \cdots & c_{2,Np} \\ \vdots & \vdots & \ddots & \vdots & \vdots & \vdots & & \vdots \\ c_{k-1,1} & c_{k-1,2} & \cdots & c_{k-1,k-1} & 0 & c_{k-1,k+1} & \cdots & c_{k-1,Np} \\ 0 & 0 & \cdots & 0 & 0 & 0 & \cdots & 0 \\ c_{k+1,1} & c_{k+1,2} & \cdots & c_{k+1,k-1} & 0 & c_{k+1,k+1} & \cdots & c_{k+1,Np} \\ \vdots & \vdots & & \vdots & \vdots & \vdots & \ddots & \vdots \\ c_{Np,1} & c_{Np,2} & \cdots & c_{Np,k-1} & 0 & c_{Np,k+1} & \cdots & c_{Np,Np} \end{bmatrix} \quad (2.23)$$

The “ $k$  th parameter’s uncertainty contribution matrix” is then derived as follows:

$$\left(\Delta \overline{\overline{C}}_a^{post}\right)_k \equiv \overline{\overline{C}}_a^{post} - \left(\overline{\overline{C}}_a^{post}\right)_k = \overline{S}_0 \left[ \overline{\overline{C}}_p^{post} - \left(\overline{\overline{C}}_p^{post}\right)_k \right] \overline{S}_0^T = \overline{S}_0 \left(\Delta \overline{\overline{C}}_p^{post}\right)_k \overline{S}_0^T \quad (2.24)$$

$$\text{where, } \left(\Delta \overline{\overline{C}}_p^{post}\right)_k = \begin{bmatrix} 0 & \cdots & 0 & c_{1,k} & 0 & \cdots & 0 \\ \vdots & \ddots & \vdots & \vdots & \vdots & & \vdots \\ 0 & \cdots & 0 & c_{k-1,k} & 0 & \cdots & 0 \\ c_{k,1} & \cdots & c_{k,k-1} & c_{k,k} & c_{k,k+1} & \cdots & c_{k,Np} \\ 0 & \cdots & 0 & c_{k+1,k} & 0 & \cdots & 0 \\ \vdots & & \vdots & \vdots & \vdots & \ddots & \vdots \\ 0 & \cdots & 0 & c_{Np,k} & 0 & \cdots & 0 \end{bmatrix}$$

## 2. 5. Mathematical Review for the Inverse Method

While the forward problem has a unique solution, the inverse problem could have multiple solutions. In other words, there could be different sets of values of input parameters that give the same responses. The regularization term addition addresses this situation making the problem well-posed. Because of this, one needs to make explicit any available a priori uncertainty information on the input parameters. If the information, e.g. input parameter covariances, is not available, the solution of the inverse problem could be misled. The

following presentation provides insight into understanding the difficulty that the absence of a priori information on input parameters may cause.

Assuming data assimilation is performed using one time dependent observable, two input parameters and their covariances, the posterior input parameter vector can be calculated as follows:

$$\bar{p}_0^{post} = \bar{p}_0 + \begin{bmatrix} \sum_{t=1}^T \frac{s_1^{(t)2}}{c_r^{(t)}} + \frac{\alpha^2 c_{2,2}}{c_{1,1}c_{2,2} - c_{1,2}c_{2,1}} & \sum_{t=1}^T \frac{s_1^{(t)}s_2^{(t)}}{c_r^{(t)}} - \frac{\alpha^2 c_{1,2}}{c_{1,1}c_{2,2} - c_{1,2}c_{2,1}} \\ \sum_{t=1}^T \frac{s_2^{(t)}s_1^{(t)}}{c_r^{(t)}} - \frac{\alpha^2 c_{2,1}}{c_{1,1}c_{2,2} - c_{1,2}c_{2,1}} & \sum_{t=1}^T \frac{s_2^{(t)2}}{c_r^{(t)}} + \frac{\alpha^2 c_{1,1}}{c_{1,1}c_{2,2} - c_{1,2}c_{2,1}} \end{bmatrix}^{-1} \begin{bmatrix} \sum_{t=1}^T \frac{s_1^{(t)}}{c_r^{(t)}} \Delta r^{(t)} \\ \sum_{t=1}^T \frac{s_2^{(t)}}{c_r^{(t)}} \Delta r^{(t)} \end{bmatrix} \quad (2.25)$$

where,  $s_i^{(t)}$  is the time ( $t$ ) dependent sensitivity coefficient with respect to the input parameter  $i$ ,  $c_{i,j}$  is the input parameter ( $i, j$ ) covariance (note  $c_{1,2} = c_{2,1}$ ),  $c_r^{(t)}$  is the time dependent experimental uncertainty covariance, and  $\Delta r^{(t)}$  is the mismatch,  $r_m^{-(t)} - r_0^{-(t)}$ . Note that it is assumed that the off diagonal elements of the measurement uncertainty covariance matrix are zeros, which means that the measurement errors do not have correlation. Defining matrix  $\bar{Q}$  and vector  $\bar{\gamma}$  as:

$$\bar{Q} \equiv \begin{bmatrix} \sum_{t=1}^T \frac{s_1^{(t)2}}{c_r^{(t)}} + \frac{\alpha^2 c_{2,2}}{c_{1,1}c_{2,2} - c_{1,2}c_{2,1}} & \sum_{t=1}^T \frac{s_1^{(t)}s_2^{(t)}}{c_r^{(t)}} - \frac{\alpha^2 c_{1,2}}{c_{1,1}c_{2,2} - c_{1,2}c_{2,1}} \\ \sum_{t=1}^T \frac{s_2^{(t)}s_1^{(t)}}{c_r^{(t)}} - \frac{\alpha^2 c_{2,1}}{c_{1,1}c_{2,2} - c_{1,2}c_{2,1}} & \sum_{t=1}^T \frac{s_2^{(t)2}}{c_r^{(t)}} + \frac{\alpha^2 c_{1,1}}{c_{1,1}c_{2,2} - c_{1,2}c_{2,1}} \end{bmatrix} \quad (2.26)$$

$$\bar{\gamma} \equiv \begin{bmatrix} \sum_{t=1}^T \frac{s_1^{(t)}}{c_r^{(t)}} \Delta r^{(t)} \\ \sum_{t=1}^T \frac{s_2^{(t)}}{c_r^{(t)}} \Delta r^{(t)} \end{bmatrix} \quad (2.27)$$

and inverting the matrix  $\bar{Q}$  produces the following expression for the posterior input parameter vector:

$$\begin{aligned} \bar{p}_0^{post} &= \bar{p}_0 + \bar{Q}^{-1} \bar{\gamma} \\ &= \bar{p}_0 + \frac{1}{\det(\bar{Q})} \Delta \bar{p}' \end{aligned} \quad (2.28)$$

Each component of the vector  $\Delta \bar{p}'$ , which shows the parameter adjustment is then:

$$\begin{aligned} \Delta p'_1 &= \sum_{t=1}^T \sum_{t'=1}^T \Delta r^{(t)} \frac{s_1^{(t)}}{c_r^{(t)}} \frac{s_2^{(t')2}}{c_r^{(t')}} - \sum_{t=1}^T \sum_{t'=1}^T \Delta r^{(t)} \frac{s_2^{(t)}}{c_r^{(t)}} \frac{s_1^{(t')} s_2^{(t')}}{c_r^{(t')}} \\ &+ \frac{\alpha^2 c_{1,1}}{c_{1,1} c_{2,2} - c_{1,2} c_{2,1}} \sum_{t=1}^T \Delta r^{(t)} \frac{s_1^{(t)}}{c_r^{(t)}} + \frac{\alpha^2 c_{1,2}}{c_{1,1} c_{2,2} - c_{1,2} c_{2,1}} \sum_{t=1}^T \Delta r^{(t)} \frac{s_2^{(t)}}{c_r^{(t)}} \end{aligned} \quad (2.29)$$

$$\begin{aligned} \Delta p'_2 &= \sum_{t=1}^T \sum_{t'=1}^T \Delta r^{(t)} \frac{s_2^{(t)}}{c_r^{(t)}} \frac{s_1^{(t')2}}{c_r^{(t')}} - \sum_{t=1}^T \sum_{t'=1}^T \Delta r^{(t)} \frac{s_1^{(t)}}{c_r^{(t)}} \frac{s_2^{(t')} s_1^{(t')}}{c_r^{(t')}} \\ &+ \frac{\alpha^2 c_{2,2}}{c_{1,1} c_{2,2} - c_{1,2} c_{2,1}} \sum_{t=1}^T \Delta r^{(t)} \frac{s_2^{(t)}}{c_r^{(t)}} + \frac{\alpha^2 c_{2,1}}{c_{1,1} c_{2,2} - c_{1,2} c_{2,1}} \sum_{t=1}^T \Delta r^{(t)} \frac{s_1^{(t)}}{c_r^{(t)}} \end{aligned} \quad (2.30)$$

Now assume that the two parameters affect the observable in a similar way, i.e.  $s_2^{(t)} \cong \Gamma s_1^{(t)}$ , where  $\Gamma$  is a constant. This relation is frequently observed in the thermal hydraulic system, e.g. time dependent sensitivity to the Chen heat transfer coefficient and to the Dittus-Boelter heat transfer coefficient, and will lead to the following:

$$\Delta p'_1 \cong \frac{\alpha^2 c_{1,1}}{c_{1,1} c_{2,2} - c_{1,2} c_{2,1}} \sum_{t=1}^T \Delta r^{(t)} \frac{s_1^{(t)}}{c_r^{(t)}} + \frac{\alpha^2 c_{1,2}}{c_{1,1} c_{2,2} - c_{1,2} c_{2,1}} \sum_{t=1}^T \Delta r^{(t)} \frac{s_2^{(t)}}{c_r^{(t)}} \quad (2.31)$$

$$\Delta p'_2 \cong \frac{\alpha^2 c_{2,2}}{c_{1,1}c_{2,2} - c_{1,2}c_{2,1}} \sum_{t=1}^T \Delta r^{(t)} \frac{s_2^{(t)}}{c_r^{(t)}} + \frac{\alpha^2 c_{2,1}}{c_{1,1}c_{2,2} - c_{1,2}c_{2,1}} \sum_{t=1}^T \Delta r^{(t)} \frac{s_1^{(t)}}{c_r^{(t)}} \quad (2.32)$$

or

$$\Delta p'_1 \cong \frac{\alpha^2}{1 - \Omega_p^2} \left( \frac{1}{c_{2,2}} + \frac{\Gamma \Omega_p}{\sqrt{c_{1,1}} \sqrt{c_{2,2}}} \right) \sum_{t=1}^T \Delta r^{(t)} \frac{s_1^{(t)}}{c_r^{(t)}} \quad (2.33)$$

$$\Delta p'_2 \cong \frac{\alpha^2}{1 - \Omega_p^2} \left( \Gamma \frac{1}{c_{1,1}} + \frac{\Omega_p}{\sqrt{c_{1,1}} \sqrt{c_{2,2}}} \right) \sum_{t=1}^T \Delta r^{(t)} \frac{s_1^{(t)}}{c_r^{(t)}} \quad (2.34)$$

where the correlation coefficient is given by  $\Omega_p \equiv c_{1,2} / (\sqrt{c_{1,1}} \sqrt{c_{2,2}}) = c_{2,1} / (\sqrt{c_{1,1}} \sqrt{c_{2,2}})$ . In this case the input parameter adjustment will be determined by the sensitivities, mismatch, variances and covariances. The behavior of the adjustments is as expected. As  $\alpha$  increases the magnitude of the adjustments increase. As  $c_r^{(t)}$  increase the magnitude of the adjustments decrease. Now consider the case of no correlation, i.e.  $c_{1,2} = c_{2,1} = 0$ . This condition would exist if the parameter values were determined by ideal single effect experiments. Under this condition, if  $c_{1,1}$  increases relative to  $c_{2,2}$ ,  $p'_1$  is adjusted more relative to  $p'_2$ . For the reverse situation, the reverse adjustment occurs. Again assuming no correlation, if  $\Gamma > 0$ , then the two parameters are adjusted in the same direction; however, if  $\Gamma < 0$ , then the two parameters are adjusted in counter direction. The just noted behaviors are all as expected, but those behaviors could mislead the solution since the a posteriori of each input parameter is obtained using only the sensitivity to the parameter itself and a priori uncertainty of the other parameter. For example, consider the case that the virtual experiment input parameters  $p_1 = 1 + \delta p_1$  and  $p_2 = 1 + \delta p_2$ , where  $\delta p_1$  and  $\delta p_2$  are all positive, and  $\delta p_1 \cong \delta p_2$ . Also

assume that  $s_1^{(t)}$  is negative,  $s_2^{(t)}$  is positive and  $\Gamma < -1$ .  $\Delta r^{(t)}$  will be then positive, which results in negative  $\Delta p'_1$  and positive  $\Delta p'_2$ . In this case the behavior of one parameter offsets the behavior of the other parameter, implying several combinations of the input parameters can generate the same responses. Now consider the case of positive correlation, i.e.  $\Omega_p > 0$ . For  $\Gamma > 0$ , as the correlation becomes stronger the magnitude of the parameter adjustments increase. For  $\Gamma < 0$ , as the correlation becomes stronger the magnitude of the parameter adjustments is decreased from that when  $\Gamma > 0$ . Now consider the case of anti-correlation, i.e.  $\Omega_p < 0$ . For  $\Gamma > 0$ , as the anti-correlation becomes stronger the magnitude of the parameter adjustment is decreased from that when there is positive correlation. Finally, for  $\Gamma < 0$ , as the anti-correlation becomes stronger, the  $\Delta p'_1$  and  $\Delta p'_2$  magnitude adjustments both become larger but in opposite direction.

Attention is now directed to the a posteriori input parameter covariance matrices. If the regularization parameter is one, a posteriori input parameter covariance matrix is simply:

$$\overline{C}_p^{post} = \left[ \overline{S}^T \overline{C}_r \overline{S} + \overline{C}_p \right]^{-1} \quad (2.35)$$

Defining matrix  $\overline{R}$  as:

$$\overline{R} \equiv \begin{bmatrix} \sum_{t=1}^T \frac{s_1^{(t)2}}{c_r^{(t)}} + \frac{c_{2,2}}{c_{1,1}c_{2,2} - c_{1,2}c_{2,1}} & \sum_{t=1}^T \frac{s_1^{(t)}s_2^{(t)}}{c_r^{(t)}} - \frac{c_{1,2}}{c_{1,1}c_{2,2} - c_{1,2}c_{2,1}} \\ \sum_{t=1}^T \frac{s_2^{(t)}s_1^{(t)}}{c_r^{(t)}} - \frac{c_{2,1}}{c_{1,1}c_{2,2} - c_{1,2}c_{2,1}} & \sum_{t=1}^T \frac{s_2^{(t)2}}{c_r^{(t)}} + \frac{c_{1,1}}{c_{1,1}c_{2,2} - c_{1,2}c_{2,1}} \end{bmatrix} \quad (2.36)$$

a posteriori input parameter covariance matrix can be calculated as follows:



$$\overline{C}_p^{post} = \frac{1}{\det(\overline{R})} \begin{bmatrix} \sum_{t=1}^T \frac{s_2^{(t)2}}{c_r^{(t)}} + \frac{c_{1,1}}{c_{1,1}c_{2,2} - c_{1,2}c_{2,1}} & -\sum_{t=1}^T \frac{s_1^{(t)}s_2^{(t)}}{c_r^{(t)}} + \frac{c_{1,2}}{c_{1,1}c_{2,2} - c_{1,2}c_{2,1}} \\ -\sum_{t=1}^T \frac{s_2^{(t)}s_1^{(t)}}{c_r^{(t)}} + \frac{c_{2,1}}{c_{1,1}c_{2,2} - c_{1,2}c_{2,1}} & \sum_{t=1}^T \frac{s_1^{(t)2}}{c_r^{(t)}} + \frac{c_{2,2}}{c_{1,1}c_{2,2} - c_{1,2}c_{2,1}} \end{bmatrix} \quad (2.37)$$

Analysis was performed to observe how the two parameters are correlated assuming  $s_2^{(t)} \cong \Gamma s_1^{(t)}$ . The a posteriori input parameter correlation is:

$$\Omega_p^{post} = \frac{\Gamma \sum_{t=1}^T \frac{s_1^{(t)2}}{c_r^{(t)}} - \frac{\Omega_p}{\sqrt{c_{1,1}}\sqrt{c_{2,2}}(1-\Omega_p^2)}}{\sqrt{\left( \Gamma^2 \sum_{t=1}^T \frac{s_1^{(t)2}}{c_r^{(t)}} + \frac{1}{c_{2,2}(1-\Omega_p^2)} \right) \left( \sum_{t=1}^T \frac{s_1^{(t)2}}{c_r^{(t)}} + \frac{1}{c_{1,1}(1-\Omega_p^2)} \right)}} \quad (2.38)$$

The denominator is noted to always be positive, so whether posterior is correlated or anti-correlated depends on the sign of the numerator. Assuming no a priori correlation, the posteriori correlation is anti-correlated if  $\Gamma > 0$  and positively correlated if  $\Gamma < 0$ . When prior correlation exists, i.e.  $\Omega_p \neq 0$ , for  $\Gamma > 0$  the posteriori is anti-correlated for a small magnitude of  $\Omega_p$ . Positive correlation occurs if now  $\Gamma < 0$  and  $|\Omega_p|$  small. As  $\Omega_p$  grows positive posteriori can become positively correlated, whereas, if it grows negative the posteriori remains anti-correlated. For  $\Omega_p$  with a large magnitude versus  $\Gamma$ 's magnitude, the posteriori correlation approaches the a priori correlation. An increase in the magnitude of  $\Gamma$  will weaken the posteriori correlation with respect to the a priori correlation if both  $\Gamma$  and  $\Omega_p$  have the same signs, and strengthen the posteriori correlation with respect to the a priori correlation if  $\Gamma$  and  $\Omega_p$  have different signs.

What the previous discussion reveals is that although the variance of the posteriori may decrease, the correlation may increase. The implication is that a system attribute of interest posteriori uncertainty may not decrease from a priori depending on the magnitude of parameters' posteriori correlation and attribute sensitivities to the parameters. Thus just observing the parameters' posteriori variance magnitude could lead to an improper conclusion regarding magnitude of attributes' uncertainty reduction.

## 2. 6. Design Optimization

It is proved that uncertainties on the key system attributes can be significantly reduced if the experimental data is properly utilized for data assimilation. This topic will be focused on a design on the sensor deployment and experiments that provides maximum savings via design modifications that effectively utilize the increased design freedom obtained from the reduced uncertainties achieved, while retaining safety margin. The design feature one is especially interested in is electric power rating, which is limited by not only normal operation but by transient conditions due to safety limits, e.g. CHF during LOFA. Control systems can correct for some changes in NSSS conditions due to accident initiators, but they eventually exceed the capability to control the reactor system, e.g. turbine CV fully open. If it is assumed that the reactor controllers are inactive, then the system will be even more limited. As noted, the degree of design freedom can be increased by performing additional measurements, thereby decreasing the uncertainties on key system attributes via reducing the uncertainties on input parameters to the system simulation code. This gives a posteriori probability distribution of the safety parameter, i.e.  $\tilde{\rho}(a^{post})$ . The mean value of a posteriori,

$\langle a^{post} \rangle$ , could be larger or smaller than the mean value of a priori,  $\langle a \rangle$ , implying it could get better or worse from the safety point of view. The standard deviation of  $a^{post}$  will generally decrease, which is a benefit. Note that if actual experimental data do not exist, mean values of a posteriori system responses and system attributes determined by simulation are not meaningful. So we will assume that  $\langle a^{post} \rangle$  is identical to  $\langle a \rangle$ , making only the standard deviation relevant.

The basic idea is that even though a new, more economical design of the system could shift the mean value of the system attribute to be closer to the safety limit, e.g. 95% confidence level of not experiencing DNB, the reduced uncertainty on the system attribute could more than compensate for it. Quantitatively this can be stated as:

$$\int_{S_a} p(a) da = \int_{S_a} \tilde{p}(a^{post} - \delta a) da^{post} \quad (2.39)$$

where  $S_a$  denotes the allowed range of the system attributes,  $p(a)$  the a priori probability distribution for the current design,  $\tilde{p}(a^{post} - \delta a)$  the a posteriori probability distribution for the new design, and  $\delta a$  the “margin saving.” When  $\delta a > 0$  this implies the system attribute is constrained by an upper safety limit; whereas, when  $\delta a < 0$  this implies it is constrained by a lower safety limit. For safety limits,  $\int_{S_a} p(a) da$  is usually  $\geq 0.95$ . Using Equation (2.39)

to determine the value of  $\delta a$ , it can be used to constrain a modified IRIS design as follows:

$$|\delta a(\bar{l}, \bar{x})| \equiv \left| \langle a^{post\ mod}(\bar{l}, \bar{x}) \rangle - \langle a^{post}(\bar{l}, \bar{x}) \rangle \right| \quad (2.40)$$

where  $\langle a^{post\ mod}(\bar{l}, \bar{x}) \rangle$  is the nominal (mean) value of the modified design of a posteriori system attribute obtained using the larger degree of design freedom, and  $\langle a^{post}(\bar{l}, \bar{x}) \rangle$  is the nominal value of a posteriori system attribute for the original design. Vector  $\bar{l}$ , which has 0 or 1 values, indicates where a certain type of sensor is used at a specific location; and,  $\bar{x}$  is a vector, whose elements are 0 or 1, indicates whether experiment type  $n$  is to be completed. In this work  $\langle a^{post} \rangle$  is assumed identical to the a priori mean,  $\langle a \rangle$ , for lack of real experiments being performed and to isolate the benefits of uncertainty reduction via experiments. Figure 7 visualizes this concept.

The optimization problem decision variables include the selection of sensor types and locations, and experiment type imposing realistic constraints, with the objective of maximizing the savings achieved by utilizing the larger degree of the plant operational freedom created by system attribute uncertainty reduction, offset by the cost of sensors and experiments. To implement the above, one needs to obtain the a posteriori system attribute covariance matrix  $\bar{C}_a^{post}(\bar{l}, \bar{x})$  as a function of the sensors and experiments utilized, i.e. a function of  $(\bar{l}, \bar{x})$ . Assuming that a Gaussian distribution is applicable for the system attributes, implying the system is linear,  $\bar{C}_a^{post}(\bar{l}, \bar{x})$  can be obtained using Equations (2.19)

and (2.20), where  $\bar{S}^T \bar{C}_m^{-1} \bar{S} = \sum_{n=1}^{N_n} \sum_{j=1}^{N_j} (\bar{x})_n (\bar{l})_j \bar{S}_{(n,j)}^T \bar{C}_{m(n,j)}^{-1} \bar{S}_{(n,j)}$ . Next, the maximum margin

saving, which is defined for the most limiting system attribute and accident, and the most concerned time step, is determined as follows:

$$\left| \langle a^{post\ mod}(\bar{l}, \bar{x}) \rangle - \langle a \rangle \right| = |L - \langle a \rangle| - 1.96\sigma_a^{post}(\bar{l}, \bar{x}) \quad (2.41)$$

where  $L$  is the safety limit for the most limiting system attribute, and  $\sigma_a^{post}(\bar{l}, \bar{x})$  is the a posteriori standard deviation of the limiting system attribute. If the current system is designed based on a 95/95 safety criteria and all the margin was properly utilized,  $|L - \langle a \rangle|$  is equal to  $1.96\sigma_a^{prior}$ , where  $\sigma_a^{prior}$  is the a priori standard deviation of the limiting system attribute. In this case, the safety limits are defined as:

$$L = \begin{cases} \langle a \rangle + 1.96\sigma_a^{prior} & \text{if } L > \langle a \rangle \\ \langle a \rangle - 1.96\sigma_a^{prior} & \text{if } L < \langle a \rangle \end{cases} \quad (2.42)$$

The maximum allowed mean value of the system attribute that satisfies the 95/95 safety criteria is then calculated using Equation (2.41):

$$\langle a^{post\ mod}(\bar{l}, \bar{x}) \rangle = \begin{cases} \langle a \rangle + 1.96[\sigma_a^{prior} - \sigma_a^{post}(\bar{l}, \bar{x})] & \text{if } L > \langle a \rangle \\ \langle a \rangle - 1.96[\sigma_a^{prior} - \sigma_a^{post}(\bar{l}, \bar{x})] & \text{if } L < \langle a \rangle \end{cases} \quad (2.43)$$

The algorithm presented above is the outer iteration which seeks to determine optimum sensor and experiment sets. Note that it is assumed that the a posteriori uncertainty is unaltered by system design modifications, an assumption in practice easily removed but clouds the intuitive understanding.

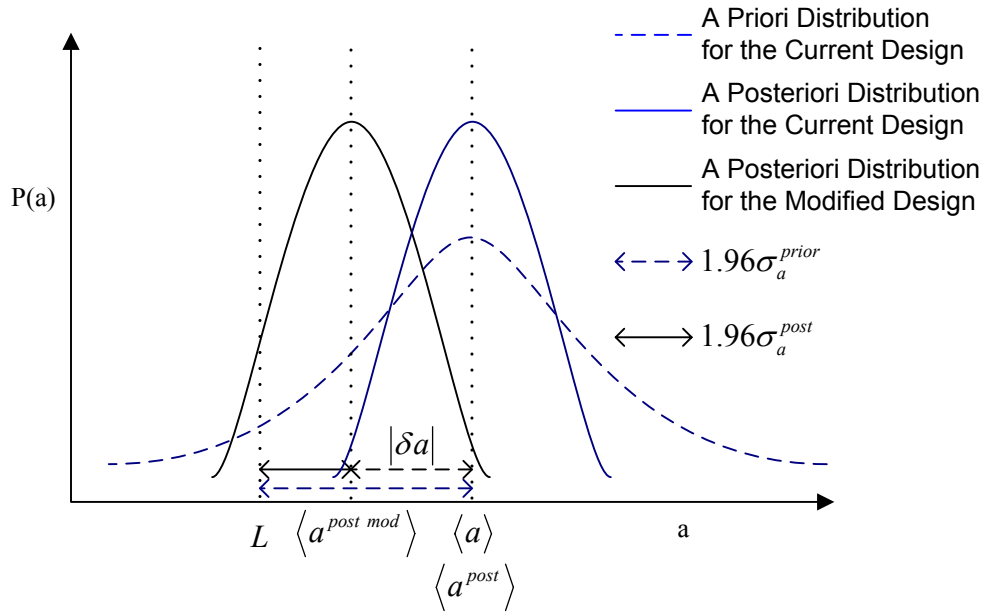


Figure 7. A Priori and A Posteriori System Attribute Distributions

Now, the best modified design specs, which maximize the savings, constrained by the safety criteria will be decided by solving the suboptimization problem, which will be the inner iteration of the algorithm. The modified design specs which are a function of the system attribute uncertainties can be determined by perturbing the specs, which are the decision variables, with the constraint of not exceeding the maximum allowed value of the mean of the system attribute. The allowed difference between the current and modified design specs will eventually become larger as more sensors are used and more experiments are conducted, since additional experimental data reduces a posteriori system attribute uncertainties.

To formulate the objective function, one begins by defining  $\bar{\mu}_d$  as the savings associated with each of the design specs. For example one of the elements of the design specs could be

the pump force, then the corresponding value in  $\bar{\mu}_d$  would be the savings achieved by reducing the size of the pump. The total savings originating from the a posteriori optimum design specs is then:

$$\mu_D(\bar{l}, \bar{x}) = \bar{\mu}_d^T \bar{\delta d}(\bar{l}, \bar{x}) = \bar{\mu}_d^T \left[ \bar{d}^{mod}(\bar{l}, \bar{x}) - \bar{d}_0 \right] \quad (2.44)$$

where  $\bar{d}^{mod}$  is the optimum design specs that satisfy all the a posteriori safety margins, and  $\bar{d}_0$  is current design specs. The total savings is obviously a function of the sensor and experiment vectors since the a posteriori system attribute uncertainties which determine the maximum allowed value of the system attribute depend on those vectors. Let vector  $\bar{C}_i$  denotes the cost of each sensor. Then  $C_I$ , the total sensor cost, is given by:

$$C_I = \bar{C}_i^T \bar{l} \quad (2.45)$$

Likewise, defining  $(\bar{C}_e)_n$  as the cost of performing experiment  $n$ , then  $C_E$ , the total cost of conducting all the experiments, is given by:

$$C_E = \bar{C}_e^T \bar{x} \quad (2.46)$$

The total cost for the sensors and experiments is then:

$$C_T = C_I + C_E \quad (2.47)$$

The objective is to maximize the savings achieved from the tighter safety margin, i.e. larger degree of the design freedom, offset by the costs of sensors and experiments, which can be expressed as the following objective:

$$\begin{aligned} & \max_{\bar{l}, \bar{x}} \left[ \max_{\bar{d}} \left\{ \mu_D(\bar{l}, \bar{x}) \right\} - C_T \right] \\ & = \max_{\bar{l}, \bar{x}} \left[ \max_{\bar{d}^{mod}} \left\{ \mu_d^{-T} \left( \bar{d}^{mod}(\bar{l}, \bar{x}) - \bar{d}_0 \right) - \left\{ \bar{C}_i^T \bar{l} + \bar{C}_e^T \bar{x} \right\} \right\} \right] \end{aligned} \quad (2.48)$$

constrained to Equation (2.39). In evaluating Equation (2.48), one proceeds as follows. For all the accidents being considered, the posteriori values for each safety attribute must satisfy the safety criteria, e.g. 95/95, at all times during the accident progression for the modified IRIS design. There may be several alternative designs that satisfy the constraints, but we seek the design that maximizes the savings of the modified design. Thus embedded within the optimization expressed by Equation (2.48), whose decision variables are the sensors' selection and locations, and the experiments to conduct, is the suboptimization to determine the optimum design specs  $\bar{d}^{mod}$ .

The optimization problem can be solved using the simulated annealing [26] algorithm which was introduced to find the equilibrium configuration of particles at a given temperature. Each configuration of the system is represented by the Boltzmann factor:

$$P(E_i) = \exp\left(-\frac{E_i}{k_B T}\right) \quad (2.49)$$

where  $E_i$  is the energy of state  $i$ ,  $k_B$  is the Boltzmann's constant and  $T$  is the temperature.

The Boltzmann factor is a weighting factor that determines the relative probability of a particle to be in a state  $i$  in a multi-state system in thermodynamic equilibrium at temperature  $T$ . The Metropolis algorithm, which was introduced in section 2.2.2, can be used to obtain an efficient simulation of a collection of atoms at a given temperature.



Following the Metropolis algorithm, atoms are given small random displacements and the resulting change,  $\Delta E$ , in the energy of the system is computed in each trial. The probability that the configuration is accepted is:

$$P(\Delta E) = \exp\left(-\frac{\Delta E}{k_B T}\right) \quad (2.50)$$

By iterating this procedure, one can simulate the thermal motion of atoms at temperature  $T$ . Physically and mathematically it is obvious that the fluctuation of the energy is large at higher temperature; however, the energy will be converged to the lower state as temperature decreases. Simulations that determine the low energy state of the atom are done by careful annealing, first melting the system, then lowering the temperature slowly. This allows the solution to avoid becoming trapped in local minima. For the optimization problem, the objective function plays the role of energy and the decision variables, e.g. power rating, pump size, etc., replace the atoms.

The suboptimization problem, i.e.  $\max_{\bar{d}^{mod}} \bar{\mu}_d^T \left\{ \bar{d}^{mod}(\bar{l}, \bar{x}) - \bar{d}_0 \right\}$  in Equation (2.48), can be solved imposing constraints on the attributes' values by using penalty functions and an augmented objective function as follows [27]:

$$\max_{\bar{d}^{mod}} \bar{\mu}_d^T \left\{ \bar{d}^{mod}(\bar{l}, \bar{x}) - \bar{d}_0 \right\} + \sum_i \lambda_i \nu_i \quad (2.51)$$

where  $\lambda_i$  is the penalty function multiplier and  $\nu_i$  is the penalty function  $i$ . Penalty function  $i$  is chosen to be:

$$v_i = \begin{cases} L - \langle a^{post}(\bar{l}, \bar{x}, \bar{d}) \rangle - 1.96\sigma_a^{post}(\bar{l}, \bar{x}) & \text{if } L \text{ is upper safety limit} \\ \langle a^{post}(\bar{l}, \bar{x}, \bar{d}) \rangle - 1.96\sigma_a^{post}(\bar{l}, \bar{x}) - L & \text{if } L \text{ is lower safety limit} \end{cases} \quad (2.52)$$

where,  $\langle a^{post}(\bar{l}, \bar{x}, \bar{d}) \rangle$  is the nominal value of the perturbed system attribute, which is a function of the perturbed design specs,  $\bar{d}$ , during the simulated annealing process. The penalty function multiplier is initially very small allowing simulated annealing to search the entire solution space without constraint, and increases to direct the search toward feasible space as the search progresses.

The above can be implemented via the following algorithm steps:

D.1 Design the reactor system and simulate it with design specs  $\bar{d}^{D_g}$ , where the  $D_g$  is the design iteration index and  $g = 0, 1, 2, \dots$ . The design specs will be updated by solving the optimization problem. Let the system with design specs  $\bar{d}^{D_g}$  be denoted  $R(\bar{d}^{D_g})$ . Note that if the  $g$  is zero, then the system is designed using the original design specs.

O.1 Perform data assimilation for the system  $R(\bar{d}^{O_j})$ , where  $R(\bar{d}^{O_0}) = R(\bar{d}^{D_g})$ , by perturbing the sensor and experiment vectors  $\bar{l}^{O_j}$  and  $\bar{x}^{O_j}$ , respectively, where the  $O_j$  is the outer iteration index and  $j = 0, 1, 2, \dots$ .

O.2 Obtain the mean and the standard deviation of the a posteriori system attributes as a function of time  $t$ , i.e.  $\langle a^{att, acc post}(\bar{l}^{O_j}, \bar{x}^{O_j}, \bar{d}^{O_j}, t) \rangle$  and  $\sigma_a^{att, acc post}(\bar{l}^{O_j}, \bar{x}^{O_j}, \bar{d}^{O_j}, t)$ , for all system attributes *att* and accidents *acc*.

I.1 Calculated the augmented inner objective function after perturbing the design specs (decision variables):

$$F^* = \bar{\mu}_d^T (\bar{d}^* - \bar{d}^{D_g}) + \sum_i \lambda_i \nu_i$$

where  $\bar{d}^* = \bar{d}^{I_i} + \Delta \bar{d}$  and  $\bar{d}^{I_0} = \bar{d}^{O_j}$ . The  $I_i$  denotes the inner iteration index.

I.2 Calculate the acceptance probability:

$$P = \exp\left(-\frac{F^{I_i} - F^*}{T}\right)$$

I.3 If  $F^* \geq F^{I_i}$ , define  $\bar{d}^{I_{i+1}} = \bar{d}^*$  and  $F^{I_{i+1}} = F^*$ . Otherwise generate a random number between 0 and 1 to decide on acceptance.

I.4 When the inner objective function converges and all the constraint violations are removed, terminate the inner iteration, and save the solution as  $\tilde{F}$  and the decision variables as  $\tilde{d}$ . Otherwise return to Step I.1.

O.3 Calculate the outer objective function:

$$F^{**} = \tilde{F} - \bar{C}_i^T \bar{l}^{O_j} + \bar{C}_e^T \bar{x}^{O_j}$$

O.4 Calculate the acceptance probability for the outer optimization:

$$P = \exp\left(-\frac{F^{O_j} - F^{**}}{T}\right)$$

O.5 If  $F^{**} \geq F^{O_j}$ , define  $\bar{d}^{O_{j+1}} = \tilde{d}$  and  $F^{O_{j+1}} = F^{**}$ . Otherwise generate a random number between 0 and 1 to decide on acceptance.

O.6 When the outer objective function converges, terminate the outer iteration, and save the solution as  $\widehat{F}$  and the decision variables as  $\widehat{d}$ . Otherwise return to step O.1.

D.2 Define  $\overline{d}^{D_{g+1}} = \widehat{d}$  and  $F^{D_g} = \widehat{F}$ .

D.3 If  $\left\| \overline{d}^{D_{g+1}} - \overline{d}^{D_g} \right\|_{\infty} < \varepsilon_d$  and  $|F^{D_g}| < \varepsilon_F$ , terminate the design iteration. Otherwise return to step D.1.

Note that the penalty function multiplier  $\lambda_i$  and the temperature  $T$  were updated following the method introduced in the FORMOSA-B Code Methodology and Usage Manual [27]. During the optimization and the suboptimization those values are held at a constant until either a given number of acceptance have been achieved or a given number of trials have been attempted, whichever occurs first.

The conclusion is in order to maximize the total savings resulting from a new design specs, one should minimize the a posteriori system attribute uncertainty by conducting data assimilation and uncertainty quantification. However since the input parameter uncertainties do not go to zero and eventually converge to a certain level due to the measurement error, the rate of the uncertainty reduction deceases as more sensors are deployed and more experiments are performed. At a certain point, due to the technical limitation described above and due to the sensors and the experiments cost, it is not economically attractive to add more sensors and to conduct more experiments.

## 2. 7. Uncertainty Analysis for Reactor Control

The uncertainty analysis was conducted for reactor control problems. The reactors are controlled by several control algorithms, e.g.  $T_{ave}$  Control, Pressurizer Level Control, Steam Pressure Control and Turbine Control (RPM Control). The purpose of control is to move the system from its current state to the desired state. Controlling some observables, e.g. average coolant temperature, assures future system states, e.g. relative core power, have their desired values. Given a set of alternative control algorithms, our interest is to select the algorithm that minimizes the time integrated deviation of the actual state from the desired state. These deviations originate due to inadequacy of the control system, and uncertainties in the observable values, e.g. average coolant temperature, feed flow rate, steam flow rate, etc. When the system responses change their trajectories following the control algorithm, it could result in the reactor controllers exceeding their capability, for example the pressurizer heater capacity, resulting in a lack of control. To ascertain whether this occurs, the capability to complete high fidelity simulation, i.e. small uncertainty, accounting for prediction and measurement uncertainties of the control algorithm utilized detector signals is required. In assessing which control algorithm is preferred, those uncertainties in the observable values used as input to the control algorithms must be considered. When simulating the plant, there are also uncertainties in the predicted actual state that could effect the selection of the best control algorithm to utilize.

### 2.7.1. Control Algorithms in the Simulator

A Westinghouse report [28] and the simulation code were reviewed to identify the control algorithms in the IRISN.Ver08.Mod06. The main equipment that the control system controls in the IRIS reactor system are:

1. Control Rods
2. Feed Pumps
3. Feed Control Valves (FCV)
4. Turbine Control Valves (TCV)
5. Pressurizer Heaters

and the main control algorithms for the IRIS reactor are:

1. Feed and Turbine Control
2. Steam Pressure Control
3. Reactor Power Control
4. Pressure Control

The algorithms in the simulator are presented below.

#### 1) Feed and Turbine Control

Generally the feed flow rate follows feed flow demand. The feed flow demand  $D_f$  is defined

as:

$$D_f \equiv \dot{m}_{SG0} \frac{W_{load}}{W_{ref}} + \int_{t_0}^{t_c} K_{shim} \dot{m}_{SG0} \frac{W_{load} - W_{turb}}{W_{ref}} dt$$

where  $t_0$  and  $t_c$  denote initial and current time, respectively,  $\dot{m}_{SG0}$  the nominal steam flow rate ( $4.96 \times 10^5$  lbm/hr),  $W_{ref}$  the reference turbine load (335 MWe),  $W_{load}$  the turbine load,  $W_{turb}$  the turbine output, and  $K_{shim}$  integral gain of turbine ( $10 \text{ hr}^{-1}$ ). Note that the values in parentheses indicate the nominal values for the current IRIS reactor design. The feed shim  $S$  is defined as:

$$S \equiv \int_{t_0}^{t_c} K_{shim} \dot{m}_{SG0} \frac{W_{load} - W_{turb}}{W_{ref}} dt$$

Thus the feed flow demand follows the turbine load and it is corrected by the feed shim. The feed control valve position change  $\Delta V_{FCV}$  at each time step is determined by:

$$\Delta V_{FCV} = g_o^{FCV} + g_p^{FCV} \delta \dot{m} + g_i^{FCV} \int \delta \dot{m} dt$$

where  $g_o^{FCV}$  is controller offset (0),  $g_p^{FCV}$  is FCV proportional gain (0.05), and  $g_i^{FCV}$  is FCV integral gain ( $0.07 \text{ hr}^{-1}$ ). The  $\delta \dot{m}$  is the flow error which is defined as:

$$\delta \dot{m} = \frac{D_f - \dot{m}_F}{D_{f0}} = \frac{D_f - \dot{m}_F}{\dot{m}_{SG0}}$$

where  $\dot{m}_F$  is the feed flow rate per steam generator and  $D_{f0}$  is the nominal flow demand.

Note that the nominal flow demand is identical to the nominal steam flow rate.

The feed flow rate per steam generator is controlled by not only the feed control valves but also the feed pumps. The feed pump speed change  $\Delta \Omega$  is determined by:

$$\Delta \Omega = g_p \delta P_D$$

where  $g_p$  is the feed pump speed proportional gain (0.1) and  $\delta P_D$  is the secondary side pressure drop error which is defined as:

$$\delta P_D = \Delta P_{ref} - \Delta P = \Delta P_{ref} + P_{SG} - P_{discharge}$$

where  $P_{SG}$  is the steam pressure. Feed line discharge pressure  $P_{discharge}$  is defined as:

$$P_{discharge} = P_{CD} + \Delta P_{CP} + \Delta P_{HWP} + \Delta P_{FP} - l_{FL}$$

where  $P_{CD}$  indicates condenser pressure,  $\Delta P_{CP}$  condensate pump pressure change,  $\Delta P_{HWP}$  hotwell pump pressure change,  $\Delta P_{FP}$  feed pump pressure change, and  $l_{FL}$  feed line loss.

$\Delta P_{ref}$  is the reference (desired) pressure drop across feedwater inlet (122 psia) and  $\Delta P$ , which is defined as  $\Delta P = P_{discharge} - P_{SG}$ , is the actual pressure drop across the feedwater inlet.

## 2) Steam Pressure Control

The turbine control valve position change,  $\Delta \tilde{V}_{TCV}$  at each time step is determined by:

$$\Delta \tilde{V}_{TCV} = g_o^{TCV} + g_p^{TCV} \delta P_{SG} + g_i^{TCV} \int \delta P_{SG} dt$$

where  $g_o^{TCV}$  is controller offset (0),  $g_p^{TCV}$  is TCV proportional gain (0.0002), and  $g_i^{TCV}$  is TCV integral gain (0 hr<sup>-1</sup>). The  $\delta P_{SG}$  is the steam generator pressure error which is defined as:

$$\delta P_{SG} = P_{SG} - P_{SG}^{ref}$$

where  $P_{SG}^{ref}$  is the reference steam generator pressure (862 psia). If  $\Delta \tilde{V}_{TCV} \geq 0$ , the actual turbine control valve position change  $\Delta V_{TCV}$  is determined by:



$$\Delta V_{TCV} = \min \left\{ \Delta \tilde{V}_{TCV}, \Delta \tilde{\tilde{V}}_{TCV} \right\}$$

where  $\Delta \tilde{\tilde{V}}_{TCV} = \dot{V}_{\max} \Delta t$ , and  $\dot{V}_{\max}$  is the maximum speed of the turbine control valve. If

$\Delta \tilde{V}_{TCV} < 0$ ,  $\Delta V_{TCV}$  is determined by:

$$\Delta V_{TCV} = \max \left\{ \Delta \tilde{V}_{TCV}, \Delta \tilde{\tilde{V}}_{TCV} \right\}.$$

### 3) Reactivity (Power) Control

The reactor power is controlled based on the average coolant temperature error and the mismatch between the relative electric power and the relative thermal power. The mismatch between the relative electric power and the relative thermal power is:

$$e_1 = \frac{W_{turb}}{W_{ref}} - \frac{Q_{th}}{Q_{th0}}$$

where  $Q_{th}$  is the reactor thermal output and  $Q_{th0}$  is the nominal full power (1000 MWt). The average coolant temperature mismatch is defined as:

$$e_2 = T_{ave}^{ref} - T_{ave}$$

where  $T_{ave}^{ref}$  is the reference average temperature defined as:

$$T_{ave}^{ref} = a_0 + b_0 \frac{W_{turb}}{W_{ref}}$$

where  $a_0$  and  $b_0$  are constants which are designated to be  $575.6 \text{ } ^\circ F$  and  $14.4 \text{ } ^\circ F$ , respectively, for the average temperature program. The total error is then:

$$e = \omega \cdot e_1 + e_2$$

where  $\omega$  is the weight which is selected as 5. The control rod speed  $v_{Rod}$  is then determined by:

$$v_{Rod} = g_{Rod} \left| |e| - 0.5 \right| v_{Rod}^{max} \quad \text{if } |e| > 0.5$$

where  $g_{Rod}$  is the rod gain (0.005) and  $v_{Rod}^{max}$  is the maximum rod speed (45 inches/min). The control rod speed is bounded by its minimum and maximum values. In other words if  $v_{Rod} > v_{Rod}^{max}$  at a certain time step,  $v_{Rod} = v_{Rod}^{max}$ , or if  $v_{Rod} < v_{Rod}^{min}$ , then  $v_{Rod} = v_{Rod}^{min}$ , where  $v_{Rod}^{min}$  is the minimum rod speed (3.75 inches/min). The control rod depth  $d_{Rod}$  at time  $t$  is determined by:

$$d_{Rod}^t = \begin{cases} d_{Rod}^{t-\Delta t} + v_{Rod}^t \Delta t & \text{if } e < 0 \\ d_{Rod}^{t-\Delta t} - v_{Rod}^t \Delta t & \text{otherwise} \end{cases}$$

The control rod depth is also constrained by the core geometry, i.e. if  $d_{Rod}^t > l_{Rod}$ , then  $d_{Rod}^t = l_{Rod}$ , or if  $d_{Rod}^t < 0$ , then  $d_{Rod}^t = 0$ , where  $l_{rod}$  is the control rod length.

#### 4) Primary System Pressure Control

Figure 8 shows the pressurizer heater setpoints used for the IRIS reactor simulations.

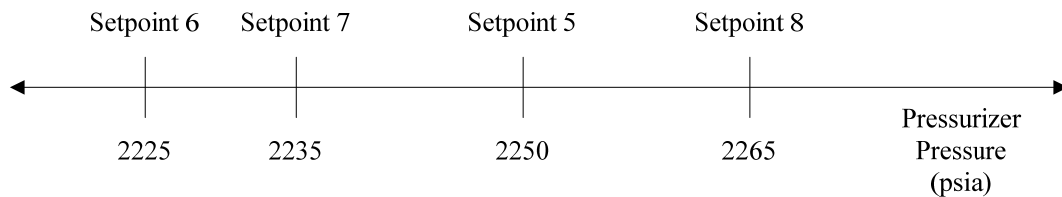


Figure 8. Pressurizer Heater Setpoints

Heater demand is calculated based on the pressurizer pressure ranges shown in the figure.

The demands for four different cases are identified and presented as follows:

*Case 1:  $P_x \geq \text{Pressure Setpoint } 8$ , where  $P_x$  is the pressurizer pressure*

In this case,  $D_p^{PH} = D_p^{BH} = 0$ , where  $D_p^{PH}$  is proportional heater demand and  $D_p^{BH}$  is backup heater demand. This means that all heaters are off in this pressure range.

*Case 2:  $\text{Pressurizer Setpoint } 8 > P_x \geq \text{Pressurizer Setpoint } 7$*

Pressurizer pressure error  $\delta P$  is defined as:

$$\delta P = P_x^{ref} - P_x$$

where  $P_x^{ref}$  is pressurizer reference pressure (2250 psia). The pressure demand  $D_p$  is then determined by:

$$D_p = D_{p0} + g_o^P + g_p^P \delta P + g_i^P \int \delta P dt$$

where  $g_o^P$  is controller offset (0),  $g_p^P$  is heater proportional gain (0.07), and  $g_i^P$  is heater integral gain (0.07 hr<sup>-1</sup>). Nominal pressurizer demand  $D_{p0}$  is defined as:

$$D_{p0} = \frac{Q_{PH}}{Q_{PHC}}$$

where  $Q_{PH}$  is pressurizer proportional heater output and  $Q_{PHC}$  is proportional heater capacity (1350 KW). The proportional heater demand is then:

$$D_P^{PH} = D_P Q_{PHC}$$

and the backup heater demand is zero. Note that if  $D_P^{PH} > Q_{PHC}$ , then  $D_P^{PH} = Q_{PHC}$ , or if

$$D_P^{PH} < 0, \text{ then } D_P^{PH} = 0.$$

*Case 3: Pressurizer Setpoint 7 >  $P_x$  > Pressurizer Setpoint 6*

$$D_P^{PH} = Q_{PHC}$$

and the backup heater demand is zero.

*Case 4:  $P_x \leq$  Pressurizer Setpoint 6*

$$D_P^{PH} = Q_{PHC}$$

$$D_P^{BH} = Q_{BHC}$$

where  $Q_{BHC}$  is backup heater capacity (1080 KW).

Pressurizer heaters output is then determined using the demand. Pressurizer proportional heater output at time  $t$  is:

$$Q_{PH}^t = Q_{PH}^{t-\Delta} e^{-\frac{\Delta}{\tau_h}} + D_P^{PH} t \left( 1 - e^{-\frac{\Delta}{\tau_h}} \right)$$

and pressurizer backup heater output at time  $t$  is:

$$Q_{BH}^t = Q_{BH}^{t-\Delta} e^{-\frac{\Delta}{\tau_h}} + D_P^{BH} t \left( 1 - e^{-\frac{\Delta}{\tau_h}} \right)$$

where  $\tau_h$  is the heater time constant (20 sec). The primary system pressure is also controlled by the pressurizer safety relief valves. Opening setpoints for pressurizer safety relief valves are all 2500 psia.

Perturbing gains or shim results in different trajectories of the system responses, e.g. feed flow rate. Note that if the gains are all zeros, all reactor controllers are inactive. The idea is one can generate several different control algorithms by perturbing those parameters, which can include the inactive control algorithms. To minimize the deviation from the desired values, multiple control algorithms will be tested and the optimum control algorithm will be identified. The algorithm for determining the controller gains accounting for sensor and simulator introduced uncertainties in the sensor readings used by the control systems is presented in the following section.

### 2.7.2. Optimum Control Algorithm

1. Define desired values (target values) of the system responses:  $\bar{r}^d$
2. Identify reactor control algorithm  $\tau$  ( $\tau = 1, \dots, N\tau$ ) by perturbing the gains and the shim etc.
3. Simulate transient whose system responses are controlled by the algorithm  $\tau$ , and obtain time dependent system responses  $\bar{r}(t)$  and its distribution  $\rho(\bar{r}, t)$  using the uncertainty

propagation method presented below. Note that one should confirm that the system attribute limits, e.g. MDNBR, are not violated by the reactor control. One should also confirm that the system responses are controlled within their acceptable band of tolerance.

3.1 Sample parameters  $\bar{p}^k$  using the parameter covariance matrix.

3.2 Sample absolute instrumentation error,  $\delta r_j^k$  using the instrumentation uncertainty for response  $j$ .

3.3 Simulate transient with perturbed parameter  $\bar{p}^k$  and obtain nominal values of the system responses  $\bar{r}^i(t)$ . Note that the time dependent system response vector which is calculated assuming the sensors are perfect, i.e. assuming no sensor uncertainties.

3.3.1 For control system actions, adjust the system responses used by the control systems as follows at time  $t$  before advancing in time:

$$\bar{r}_j^k(t) = \bar{r}_j^i(t) + \delta r_j^k(t)$$

3.4 Return to step 3.1 until a reasonable numbers of samples are simulated.

3.5 Collect all  $\bar{r}^i(t)$  and obtain observables' distributions  $\rho(\bar{r}, t)$ .

4. Calculate the control ability objective:

$$\begin{aligned}
& \frac{1}{t_f - t_0} \int_{t_0}^{t_f} \int_r \left\langle \bar{\omega}, \left( \frac{\bar{r}^d(t) - \bar{r}}{\bar{r}^d(t)} \right)^2 \right\rangle \rho(\bar{r}, t) d\bar{r} dt \\
& \cong \frac{1}{t_f - t_0} \sum_{n=1}^{Nt} \sum_{i_{Nj}=1}^{Nb} \cdots \sum_{i_2=1}^{Nb} \sum_{i_1=1}^{Nb} \left[ \sum_{j \in S^c} \omega_j \left( \frac{r_j^d(t_n) - r_{i_j}}{r_j^d(t_n)} \right)^2 \right] \rho_{i_1, i_2, \dots, i_{Nj}}(t_n) \Delta r_{i_1} \Delta r_{i_2} \cdots \Delta r_{i_{Nj}} \Delta t_n \quad (2.53)
\end{aligned}$$

where  $S^c$  denotes the set of controlled responses indices, together with the safety constraint:

$$\begin{aligned}
& \min_t \int_{\min(r_j)}^{\max(r_j)} \rho(r_j, t) dr_j \geq \rho_j^s \quad \text{for } j \in S^s \\
& \cong \min_n \sum_{i_j=1}^{Nb} \rho_{i_j}(t_n) \Delta r_{i_j} \geq \rho_j^s \quad \text{for } j \in S^s \text{ and } i_j, \text{ where } r_{i_j} \in [\min(r_j), \max(r_j)] \quad (2.54)
\end{aligned}$$

where  $S^s$  denotes the set of safety response indices, and the operational constraint:

$$\begin{aligned}
& \frac{1}{t_f - t_0} \int_{t_0}^{t_f} \int_{r_j^d(t) - \Delta r_j}^{r_j^d(t) + \Delta r_j} \rho(r_j, t) dr_j dt \geq \rho_j^o \quad \text{for } j \in S^o \\
& \cong \frac{1}{t_f - t_0} \sum_{n=1}^{Nt} \sum_{i_j=1}^{Nb} \rho_{i_j, t_n} \Delta r_{i_j} \Delta t_n \geq \rho_j^o \quad \text{for } j \in S^o \text{ and } i_j, \text{ where } r_{i_j} \in [r_j^d(t_n) - \Delta r_j, r_j^d(t_n) + \Delta r_j] \quad (2.55)
\end{aligned}$$

where  $S^o$  denotes the set of operational response indices. In the above equations  $n$  denotes a time index,  $j$  a response index,  $i_j$  a bin index for the observable  $j$ ,  $N_b$  the total number of bins,  $\bar{\omega}$  the importance of each observables (weight vector),  $\min(r_j)$  and  $\max(r_j)$  the safety limits, e.g.  $\min(r_j) = 1.3$  and  $\max(r_j) = \infty$  for the MDNBR, and  $[r_j^d - \Delta r_j, r_j^d + \Delta r_j]$  the

acceptable operational range for observable  $j$ . The  $\rho_j^s$  and  $\rho_j^o$  are the safety and operation limit probability, respectively, for response  $j$  whose values are determined from licensing limits and operational constraints. Since the control maneuvers are completed at normal operating conditions and not accident conditions, the values of the safety limits need to be selected such that there is sufficient margin at normal operating conditions that the safety limit probability is not exceeded when at accident conditions. For example, if the safety limit of concern is MDNBR and the W3 DNB correlation is being used, the  $\min(r_j)$  value appearing in Equation (2.54) should be much greater than the safety limit of 1.3 to introduce sufficient margin to assure  $\text{MDNBR} \geq 1.3$  during a loss of flow accident. The  $\rho(\bar{r}, t)$  and  $\rho(r_j, t)$  are the normalized probability distributions. In other words,

$$\rho(\bar{r}, t) = \hat{\rho}(\bar{r}, t) / \int_{\bar{r}} \hat{\rho}(\bar{r}, t) d\bar{r} \quad (2.56)$$

and

$$\rho(r_j, t) = \hat{\rho}(r_j, t) / \int_{r_j} \hat{\rho}(r_j, t) dr_j. \quad (2.57)$$

where the hatted functions ( $\hat{\rho}$ ) are unnormalized.

5. Go to 2 unless  $\tau = N\tau$ .

Thus one calculates the objective function:



$$\frac{1}{t_f - t_0} \min_{\tau} \int_{t_0}^{t_f} \int_r \left\langle \bar{\omega}, \left( \frac{\bar{r}^{-d}(t) - \bar{r}^{-\tau}}{\bar{r}^{-d}(t)} \right)^2 \right\rangle \rho(\bar{r}^{-\tau}, t) d\bar{r}^{-\tau} dt \quad (2.58)$$

constrained to:

$$\min_t \int_{\min(r_j)}^{\max(r_j)} \rho(r_j^{\tau}, t) dr_j^{\tau} \geq \rho_j^s \quad \text{for } j \in S^s \quad (2.59)$$

and

$$\frac{1}{t_f - t_0} \int_{t_0}^{t_f} \int_{r_j^d - \Delta r_j}^{r_j^d + \Delta r_j} \rho(r_j^{\tau}, t) dr_j^{\tau} dt \geq \rho_j^o \quad \text{for } j \in S^o \quad (2.60)$$

### 3. Results

#### 3.1. Mean and Standard Deviation of A Posteriori Input Parameters

Employing virtual reactor sensor data for the experiments, including the introduction of sensor errors consistent with the sensor signals known uncertainties, the inverse problem using regularization and the iteration method to address mild nonlinearity was solved and a posteriori values were obtained. The virtual experiment model parameters, a posteriori parameters and their errors in a posteriori standard deviation units are presented in Tables II, III, IV and V. Note that the errors defined as follows show us how realistic the a posteriori standard deviation values are.

$$\text{Error} = \frac{|\text{Virtual Experiment Model Parameter} - \text{Posterior Parameter}|}{\text{A Posteriori Standard Deviation of Posterior Parameter}}$$

Due to highly correlated observable sensitivities for two or more parameters, lack of covariance information and weak sensitivities with respect to certain parameters, it was shown that not all adapted parameters are in good agreement with their values used in the corresponding virtual reactor model. Data assimilation was also completed using the data from all four experiments at the same time with results presented in Table VI. Figures 9, 10, 11, 12 and 13 show associated a priori and posteriori standard deviations for the parameters. Note that  $\sigma_0$  indicates a priori standard deviation of the input parameters and  $\sigma_1$  and  $\sigma_{\text{post}}$  denote a posteriori standard deviations of the parameters calculated after the first and second iteration, respectively. It is shown that a large reduction in uncertainty can be achieved for the parameters if data from multiple experiments are utilized for data assimilation; however,

due to the parameters that affect the system in a similar way, it is also shown that the errors with respect to the true values increase as more experimental data are added.

Table II. Virtual Experiment Values and Input Parameters Adapted for Experiment A at 80 % Power

Index	Parameter	Relative Parameter Values		Error
		Virtual Experiment Model	A Posteriori	
1	Chen Correlation	1.129322047	1.014566866	1.398766966
2	Dittus-Boelter Correlation	1.094106177	1.023096863	1.110583282
3	UO <sub>2</sub> Thermal Conductivity	0.985729126	0.975832244	0.2216251
4	Friction Factors	1.05334116	1.021405281	4.45995522
5	Gap Conductance	0.806963659	1.067984217	4.640751644
6	Pellet Diameter	0.996474221	1.000511007	2.201195638
7	Clad Diameter	1.002919827	0.999113131	2.147830424
8	Clad Thermal Conductivity	0.984143372	0.989605984	0.095370202
9	Pump Head	0.987149777	0.993102287	1.088444156
10	MTC	0.953765678	0.933783858	0.64321542

Table III. Virtual Experiment Values and Input Parameters Adapted for Experiment B

Index	Parameter	Relative Parameter Values		Error
		Virtual Experiment Model	A Posteriori	
1	Chen Correlation	0.931916448	1.053354907	1.111678674
2	Dittus-Boelter Correlation	1.157408173	0.99905115	1.71824379
3	UO <sub>2</sub> Thermal Conductivity	0.974167543	1.031411167	1.294815608
4	Friction Factors	1.061389993	1.021863229	0.963023336
5	Gap Conductance	1.253420122	1.203582807	0.653443016
6	Pellet Diameter	0.995822099	1.000070991	2.125072132
7	Clad Diameter	1.005899091	1.00334465	1.678090285
8	Clad Thermal Conductivity	1.081842135	1.002905555	1.314634494
9	Pump Head	1.010500679	1.010349603	0.048116558
10	MTC	0.961641496	0.947026849	0.545035714

Table IV. Virtual Experiment Values and Input Parameters Adapted for Experiment C

Index	Parameter	Relative Parameter Values		Error
		Virtual Experiment Model	A Posteriori	
1	Chen Correlation	0.931916448	1.102411719	2.384703664
2	Dittus-Boelter Correlation	1.157408173	1.050411901	1.458002925
3	UO <sub>2</sub> Thermal Conductivity	0.974167543	0.980325765	0.129547392
4	Friction Factors	1.061389993	1.031049652	0.787225555
5	Gap Conductance	1.253420122	1.073209678	1.310304105
6	Pellet Diameter	0.995822099	1.00011336	2.165726652
7	Clad Diameter	1.005899091	1.004639245	0.898778351
8	Clad Thermal Conductivity	1.081842135	1.002611908	1.343794262
9	Pump Head	1.010500679	1.011085625	0.162505061
10	MTC	0.961641496	0.987027606	1.789849236

Table V. Virtual Experiment Values and Input Parameters Adapted for Experiment D

Index	Parameter	Relative Parameter Values		Error
		Virtual Experiment Model	A Posteriori	
1	Chen Correlation	0.931916448	1.040895622	2.510140746
2	Dittus-Boelter Correlation	1.157408173	1.030214805	3.532199091
3	UO <sub>2</sub> Thermal Conductivity	0.974167543	1.017526037	1.068096784
4	Friction Factors	1.061389993	1.034596433	0.76909746
5	Gap Conductance	1.253420122	1.190837916	0.695937988
6	Pellet Diameter	0.995822099	1.000065947	2.196746966
7	Clad Diameter	1.005899091	1.004139229	1.417847299
8	Clad Thermal Conductivity	1.081842135	1.004909702	1.354266562
9	Pump Head	1.010500679	1.010562695	0.026657208
10	MTC	0.961641496	0.967145026	0.491858142

Table VI. Virtual Experiment Values and Input Parameters Adapted using Experiments A, B, C and D

Index	Parameter	Relative Parameter Values		Error
		Virtual Experiment Model	A Posteriori	
1	Chen Correlation	1.195378183	1.119148506	1.988067533
2	Dittus-Boelter Correlation	1.011952829	1.103939219	3.205750513
3	UO <sub>2</sub> Thermal Conductivity	0.958773877	1.012308383	4.642889236
4	Friction Factors	1.027093277	1.004192396	5.094394314
5	Gap Conductance	1.23124643	1.087465374	9.299896385
6	Pellet Diameter	0.996822389	1.000287263	1.756606297
7	Clad Diameter	1.004890791	1.005074713	0.263385368
8	Clad Thermal Conductivity	1.074114209	1.027732082	0.845520076
9	Pump Head	1.013000419	1.011671655	0.900223765
10	MTC	0.963964368	0.966531435	0.359255024

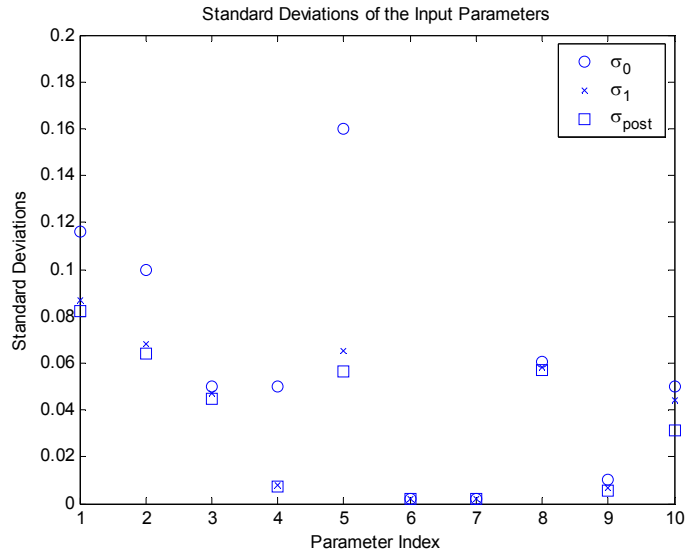


Figure 9. Standard Deviations for the Input Parameters for Experiment A at 80% Power

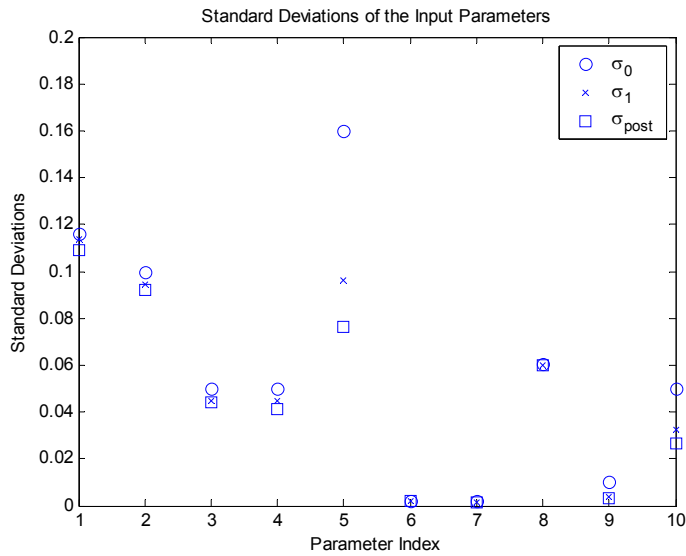


Figure 10. Standard Deviations for the Input Parameters for Experiment B

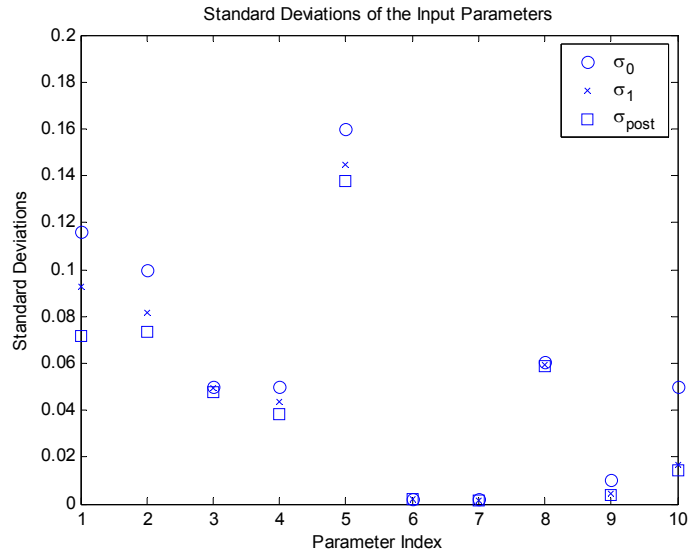


Figure 11. Standard Deviations for the Input Parameters for Experiment C

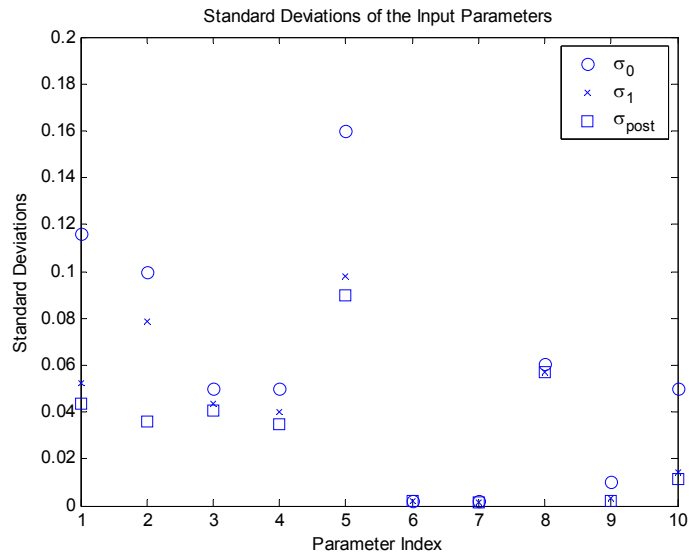


Figure 12. Standard Deviations for the Input Parameters for Experiment D

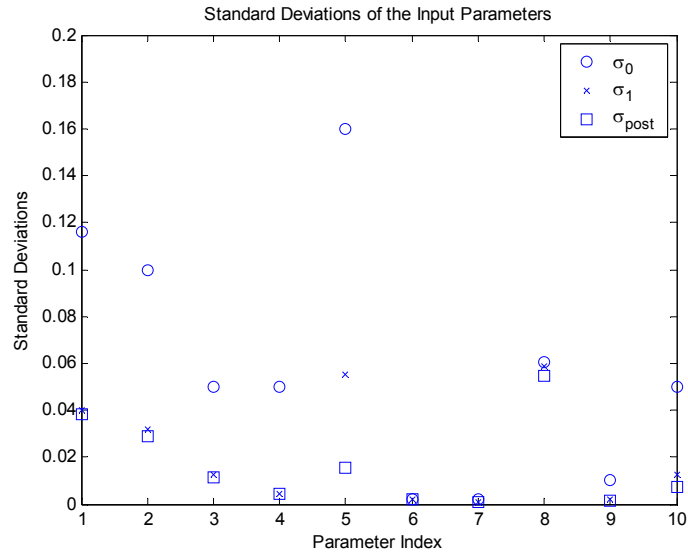


Figure 13. Standard Deviations for the Input Parameters for Experiments A, B, C and D

### 3. 2. Standard Deviation of A Posteriori System Attributes

Utilizing the a posteriori covariance of the parameters, the a posteriori distribution of the key system attributes for each of the accidents can be determined by either a linear or nonlinear approach. The a priori and posteriori standard deviations for three key system attributes at operating power level were obtained based on the assumption that the system responds linearly and are presented in Figures 14, 15, 16 and 17. These figures are obtained based on data assimilation and uncertainty quantification using only a single experiment. Figure 18, 19, 20 and 21 also show the a priori and posteriori standard deviation for the key system attributes at operating power level calculated using all four experimental data at the same time. These figures indicate that the uncertainties are reduced as more experiments are conducted.



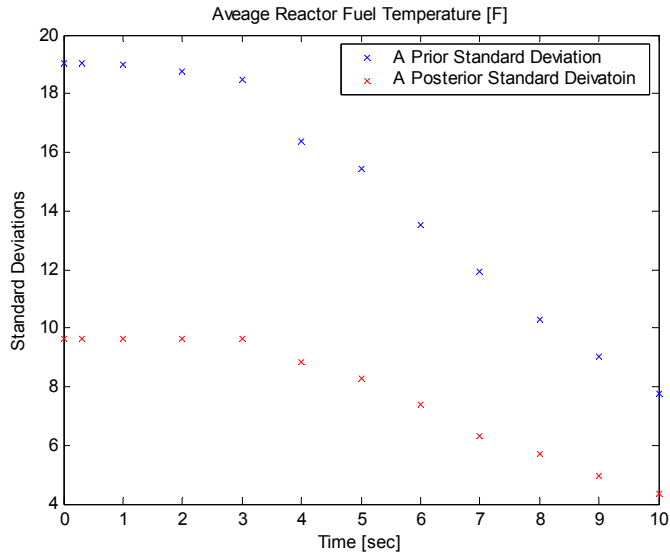


Figure 14-1. Standard Deviations for Average Fuel Temperature for RCP Trip using Experiment A at 80% Power for Data Assimilation

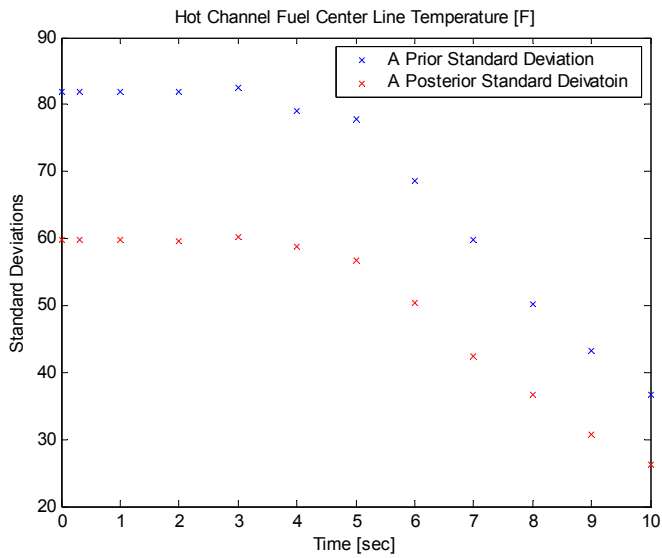


Figure 14-2. Standard Deviations for Hot Channel Fuel Centerline Temperature for RCP Trip using Experiment A at 80% Power for Data Assimilation

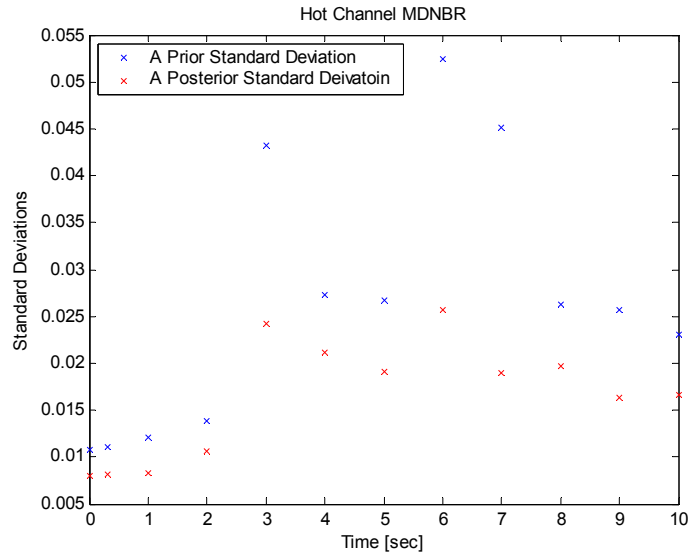


Figure 14-3. Standard Deviations for Hot Channel MDNBR for RCP Trip using Experiment A at 80% Power for Data Assimilation

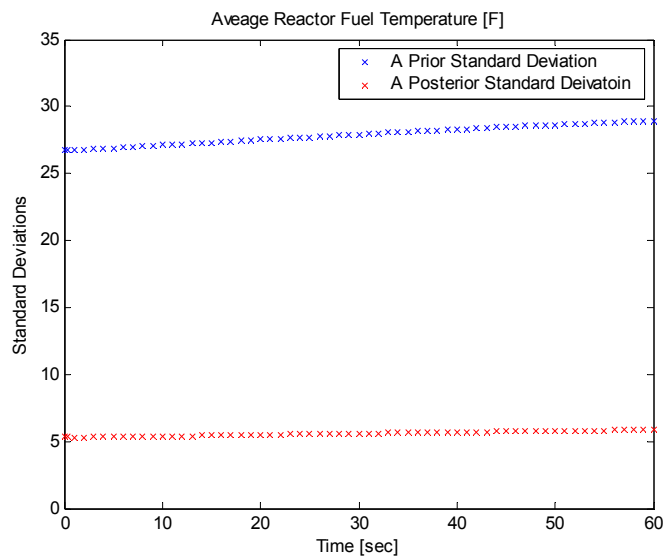


Figure 15-1. Standard Deviations for Average Fuel Temperature for Control Bank Withdrawal using Experiment B for Data Assimilation

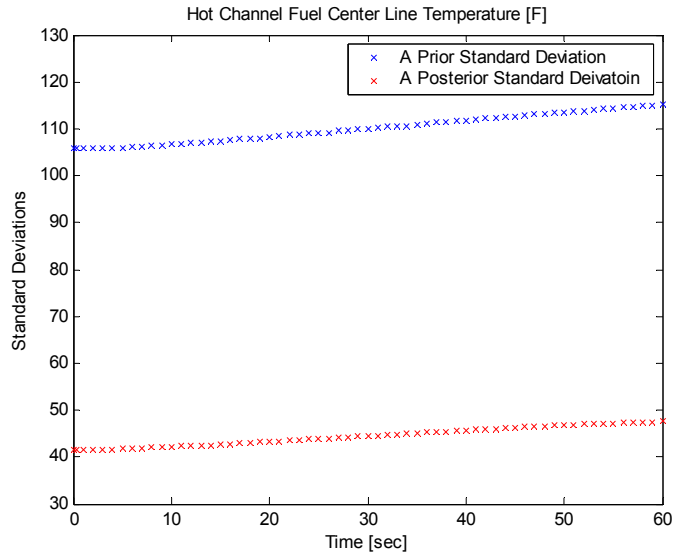


Figure 15-2. Standard Deviations for Hot Channel Fuel Centerline Temperature for Control Bank Withdrawal using Experiment B for Data Assimilation

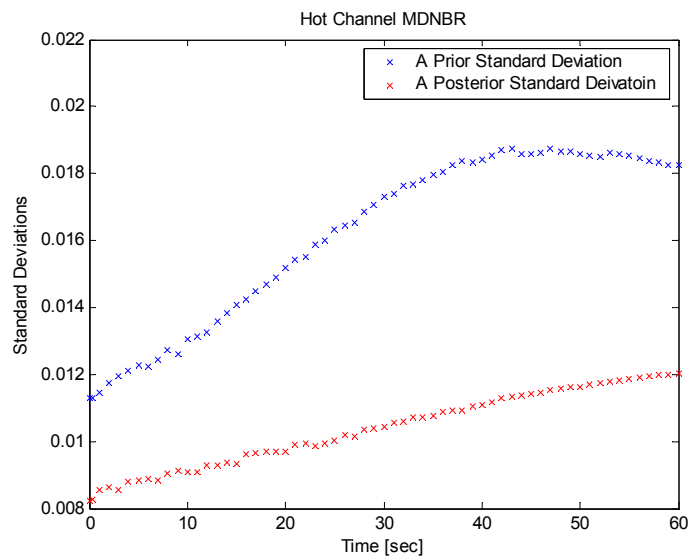


Figure 15-3. Standard Deviations for Hot Channel MDNBR for Control Bank Withdrawal using Experiment B for Data Assimilation

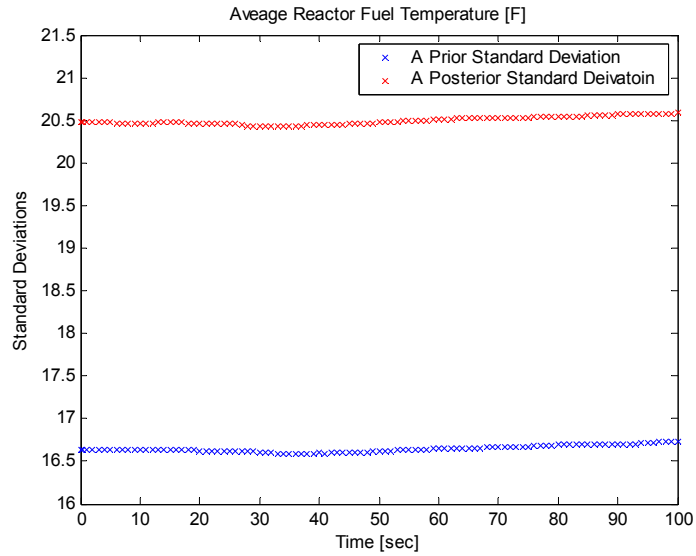


Figure 16-1. Standard Deviations for Average Fuel Temperature for FCV Failed Open using Experiment C for Data Assimilation

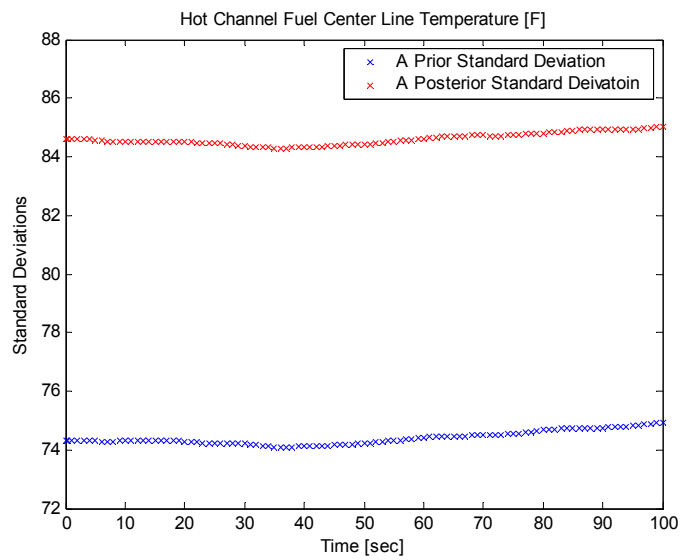


Figure 16-2. Standard Deviations for Hot Channel Fuel Centerline Temperature for FCV Failed Open using Experiment C for Data Assimilation

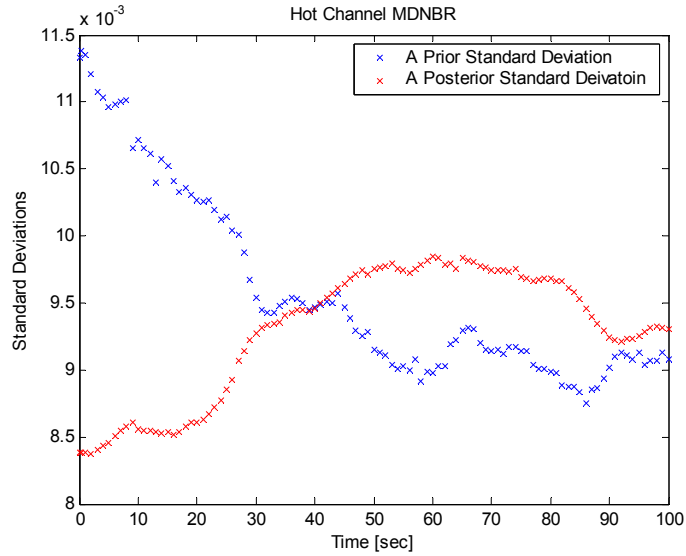


Figure 16-3. Standard Deviations for Hot Channel MDNBR for FCV Failed Open using Experiment C for Data Assimilation

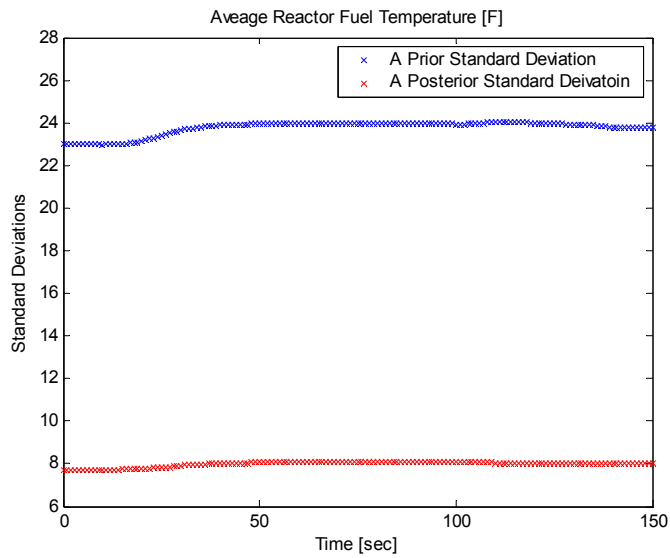


Figure 17-1. Standard Deviations for Average Fuel Temperature for TCV Failed Open using Experiment D for Data Assimilation

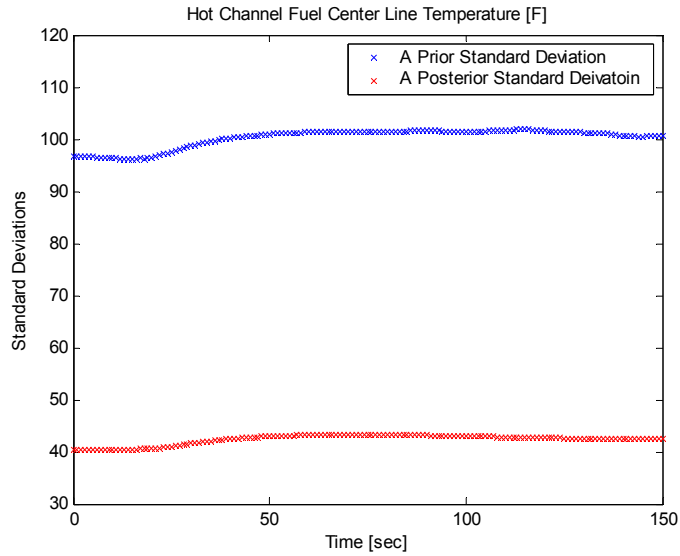


Figure 17-2. Standard Deviations for Hot Channel Fuel Centerline Temperature for TCV Failed Open using Experiment D for Data Assimilation

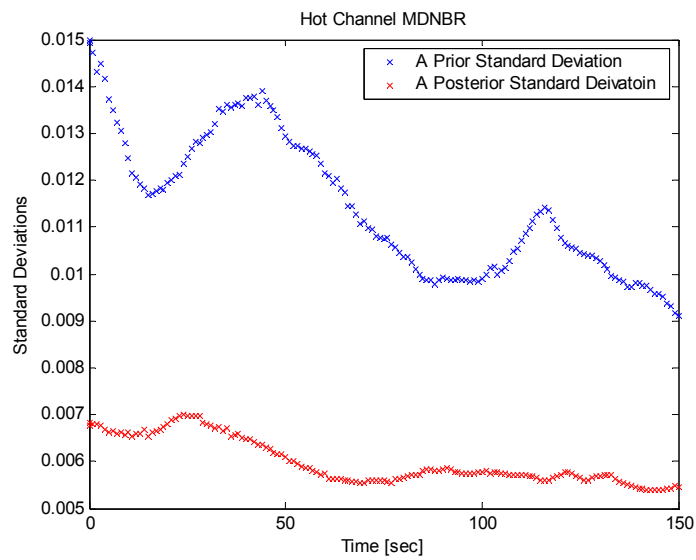


Figure 17-3. Standard Deviations for Hot Channel MDNBR for TCV Failed Open using Experiment D for Data Assimilation

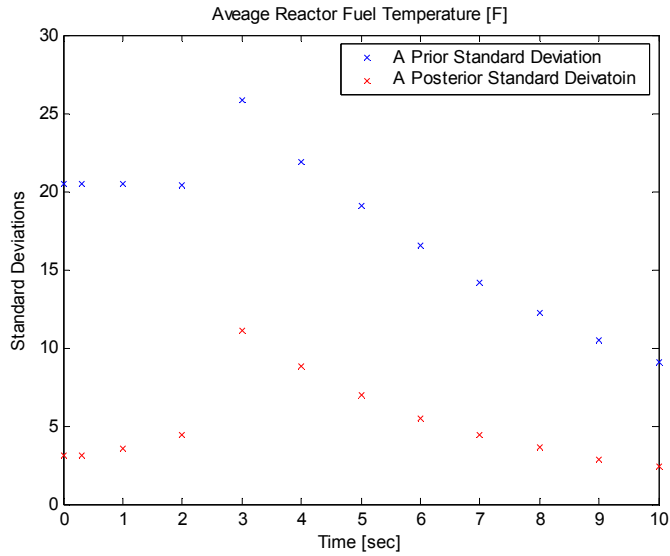


Figure 18-1. Standard Deviations for Average Fuel Temperature for RCP Trip using Experiment A, B, C and D for Data Assimilation

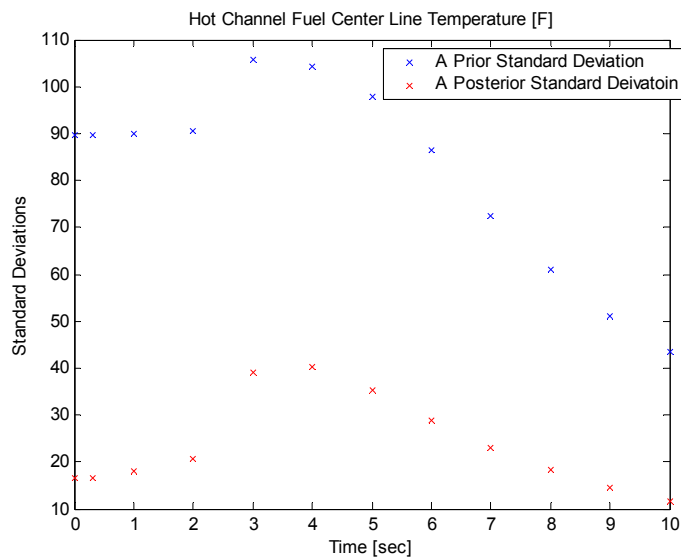


Figure 18-2. Standard Deviations for Hot Channel Fuel Centerline Temperature for RCP Trip using Experiment A, B, C and D for Data Assimilation

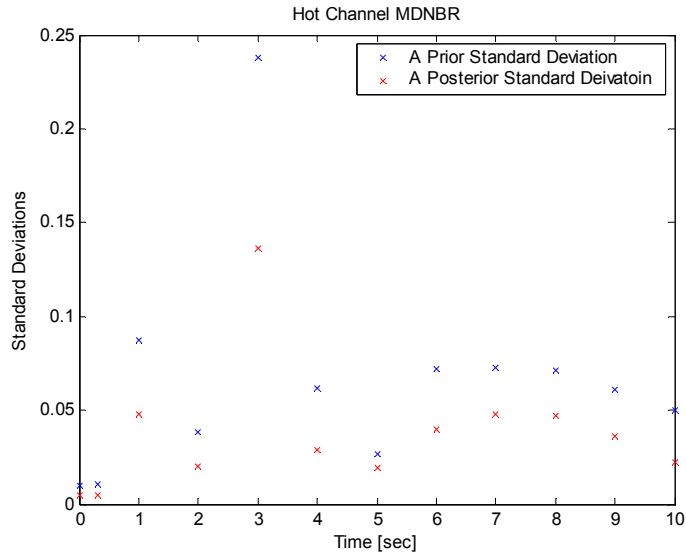


Figure 18-3. Standard Deviations for Hot Channel MDNBR for RCP Trip using Experiment A, B, C and D for Data Assimilation

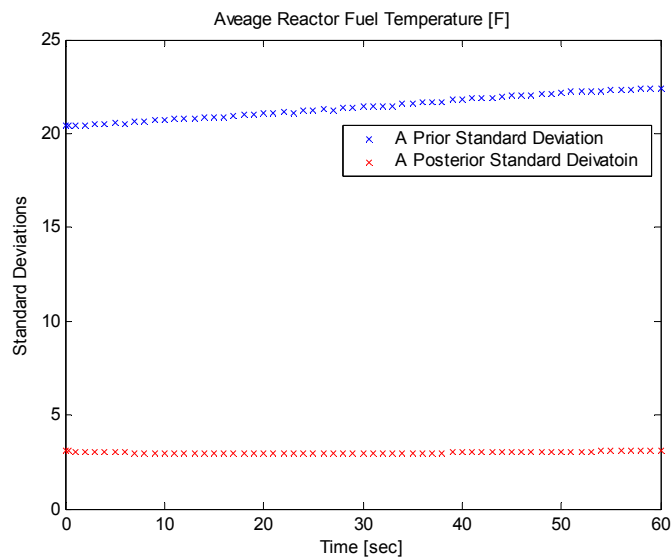


Figure 19-1. Standard Deviations for Average Fuel Temperature for Control Bank Withdrawal using Experiment A, B, C and D for Data Assimilation



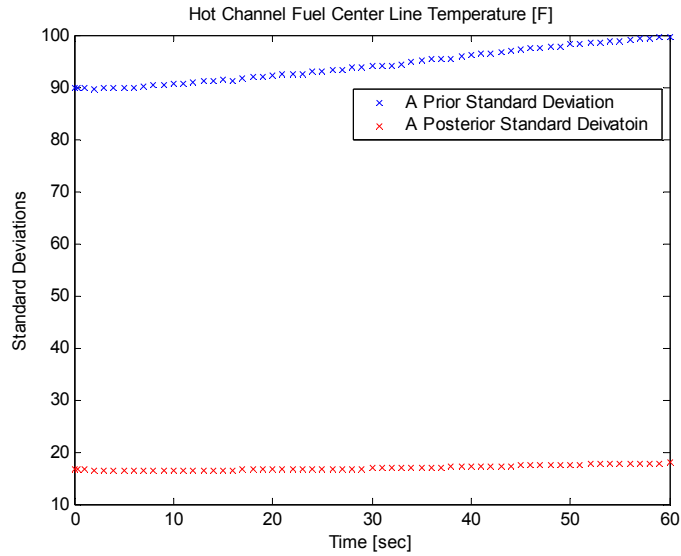


Figure 19-2. Standard Deviations for Hot Channel Fuel Centerline Temperature for Control Bank Withdrawal using Experiment A, B, C and D for Data Assimilation

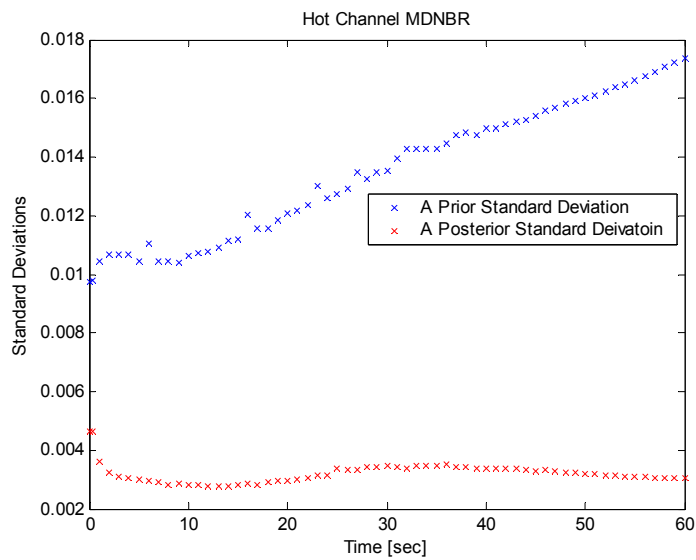


Figure 19-3. Standard Deviations for Hot Channel MDNBR for Control Bank Withdrawal using Experiment A, B, C and D for Data Assimilation

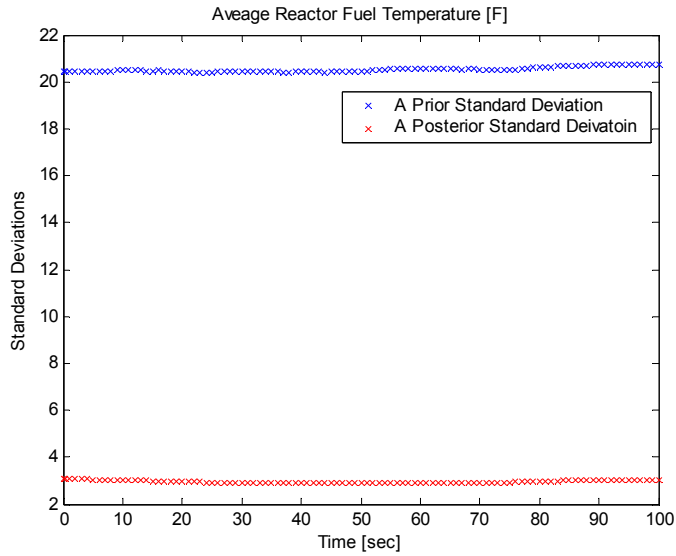


Figure 20-1. Standard Deviations for Average Fuel Temperature for FCV Failed Open using Experiment A, B, C and D for Data Assimilation

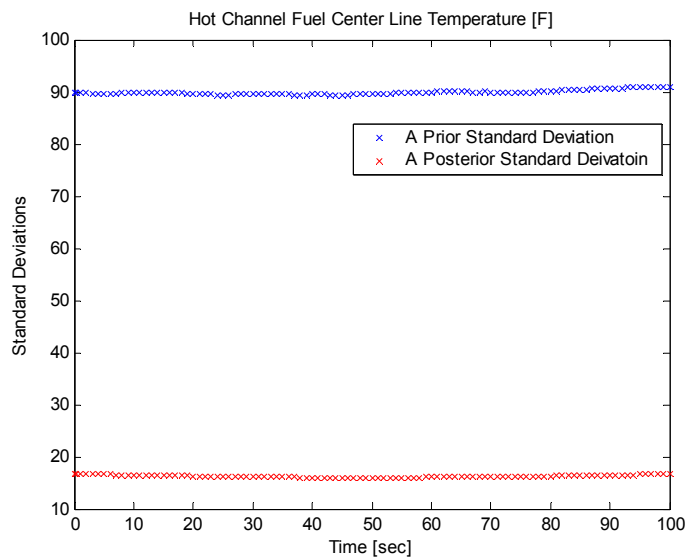


Figure 20-2. Standard Deviations for Hot Channel Fuel Centerline Temperature for FCV Failed Open using Experiment A, B, C and D for Data Assimilation

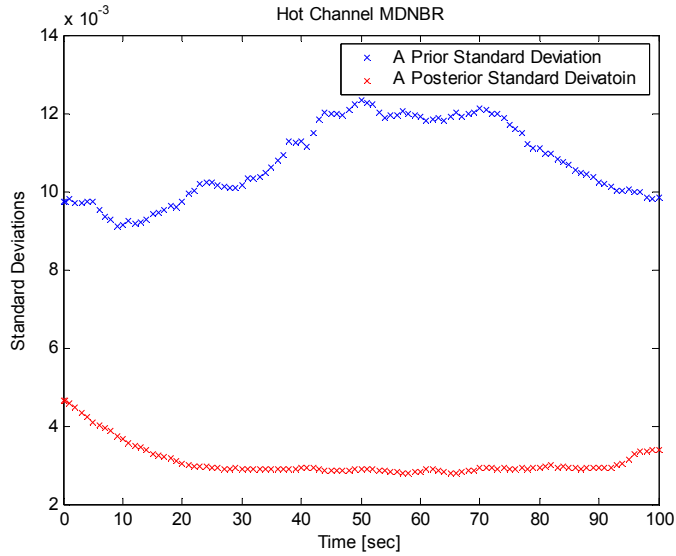


Figure 20-3. Standard Deviations for Hot Channel MDNBR for FCV Failed Open using Experiment A, B, C and D for Data Assimilation

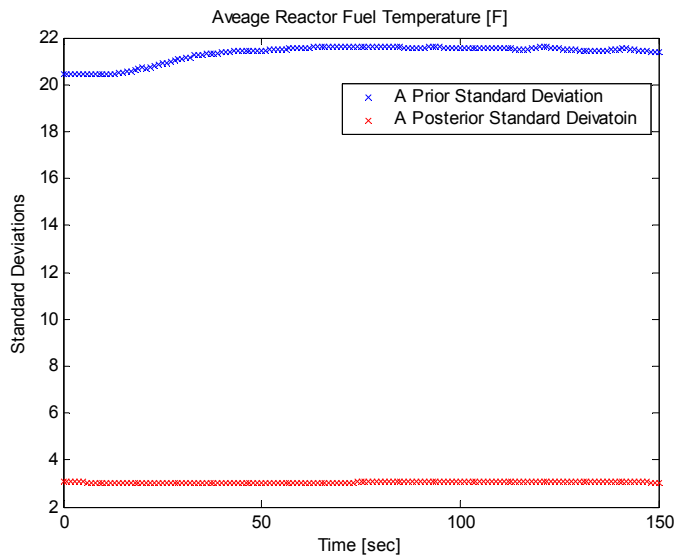


Figure 21-1. Standard Deviations for Average Fuel Temperature for TCV Failed Open using Experiment A, B, C and D for Data Assimilation

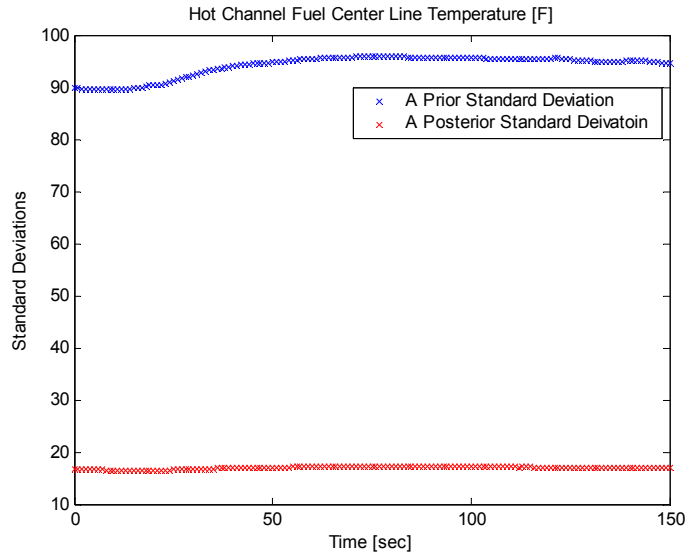


Figure 21-2. Standard Deviations for Hot Channel Fuel Centerline Temperature for TCV Failed Open using Experiment A, B, C and D for Data Assimilation

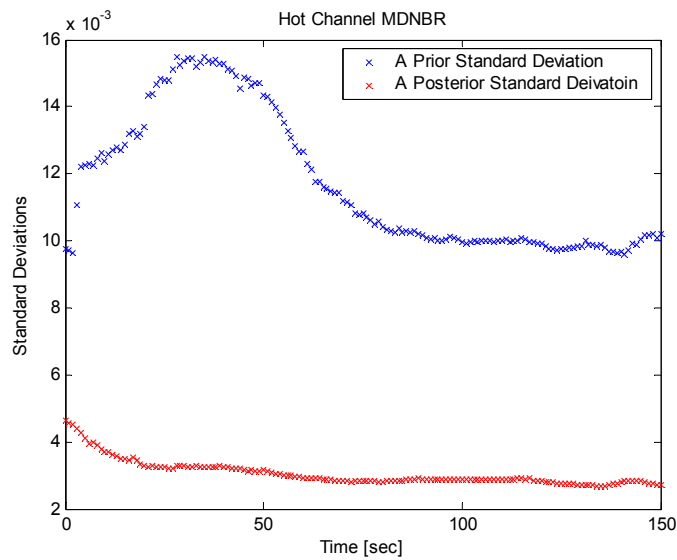


Figure 21-3. Standard Deviations for Hot Channel MDNBR for TCV Failed Open using Experiment A, B, C and D for Data Assimilation

### 3. 3. Individual Parameter's Uncertainty Contribution

Figures 22, 23, 24 and 25 present each parameter's uncertainty contribution to the three system attributes, which are obtained using a single experiment's data. Figure 26, 27, 28 and 29 present each parameter's uncertainty contribution as a result of using multiple experiments' data at the same time. As expected, major sources of uncertainty on the average fuel temperature and the hot channel fuel centerline temperature are fuel thermal conductivity and/or gap conductance. For the hot channel MDNBR, the uncertainty contribution depends upon the accident considered, with usually more than four input parameters significantly contributing to this key system attribute.

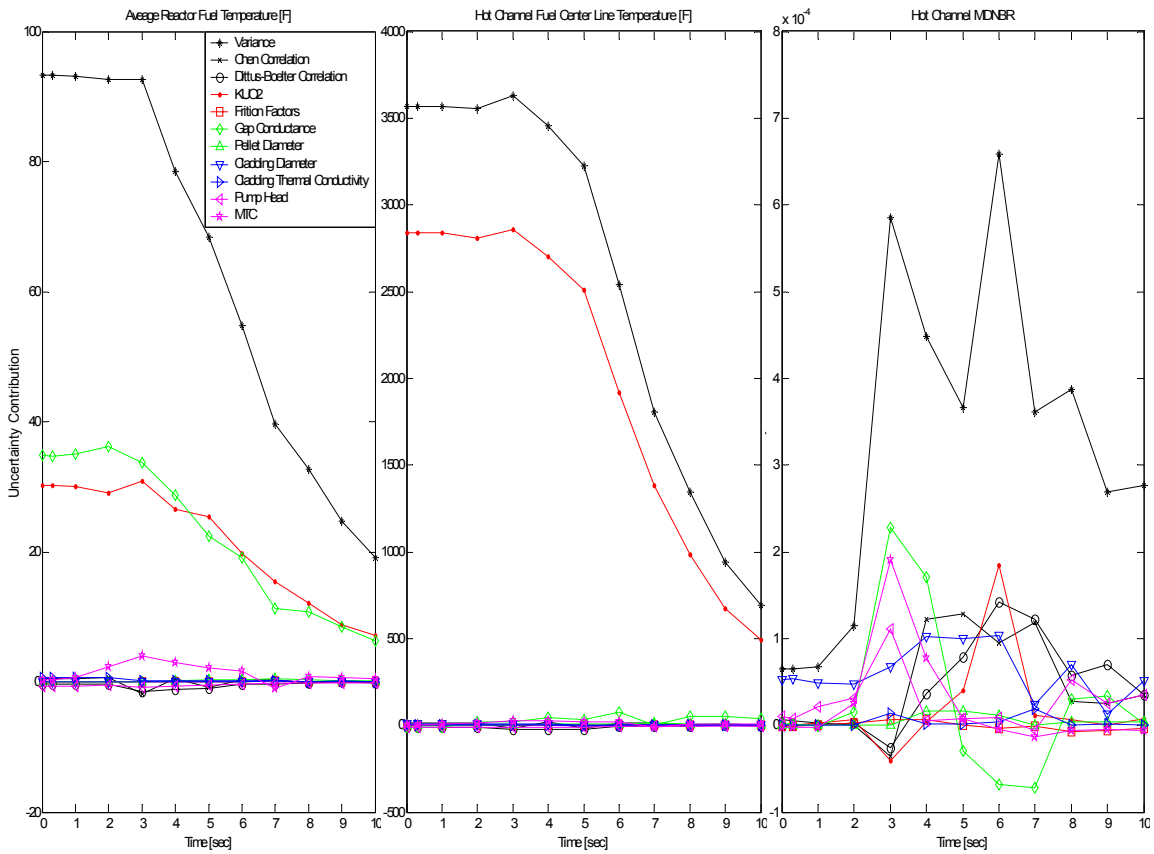


Figure 22. Each Parameter's Uncertainty Contribution to the System Attributes for RCP Trip

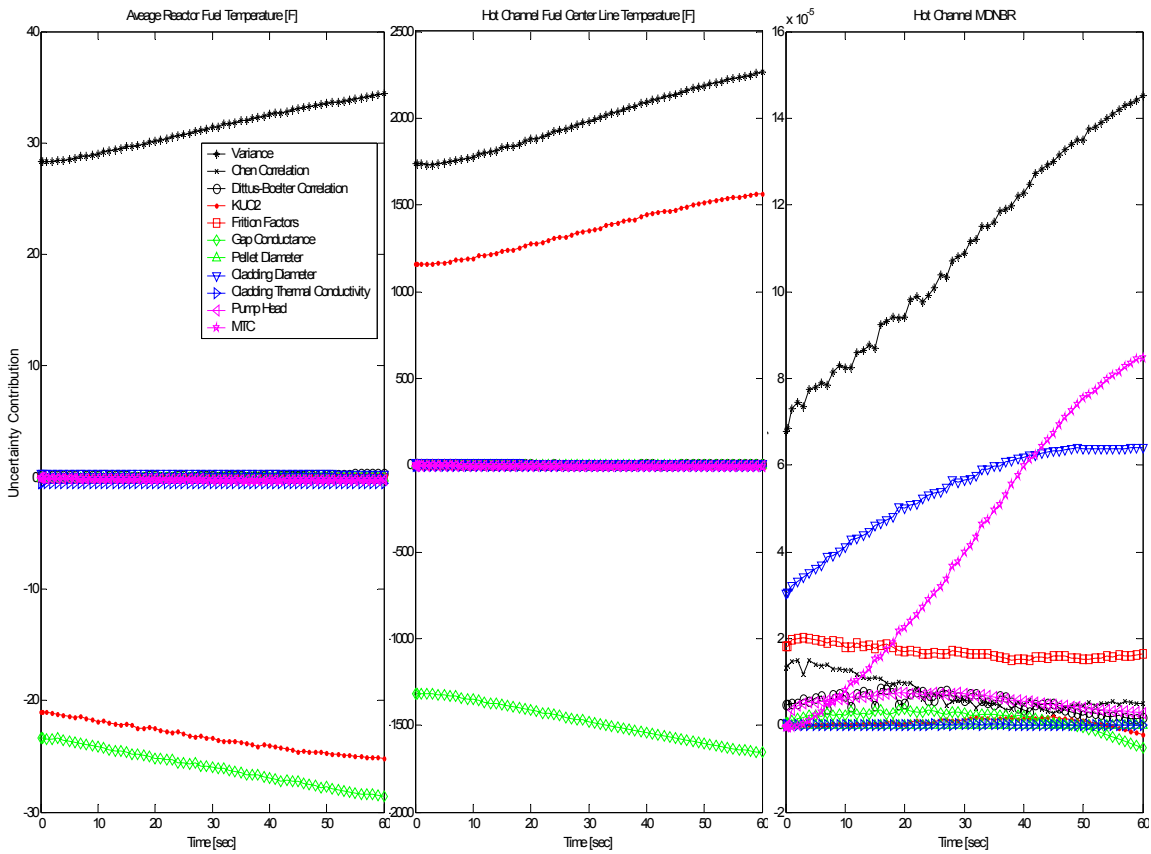


Figure 23. Each Parameter's Uncertainty Contribution to the System Attributes for Control Bank Withdrawal

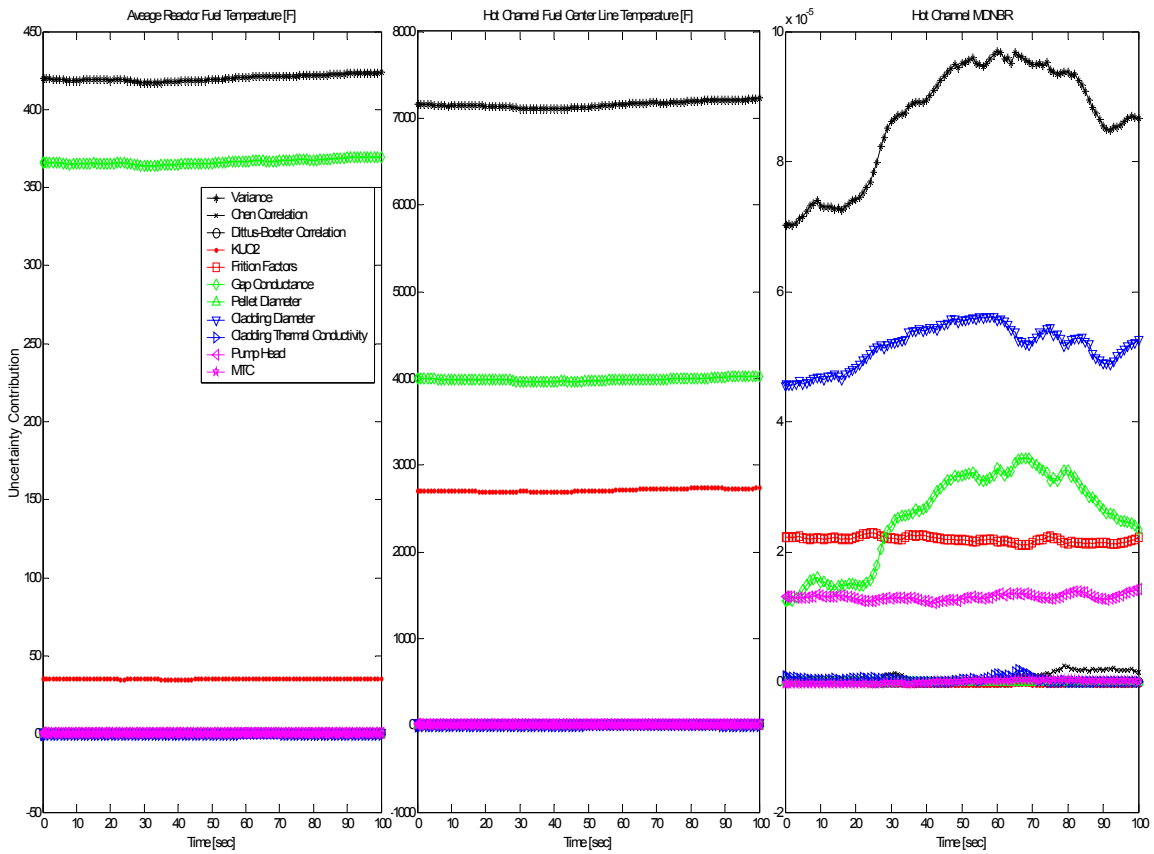


Figure 24. Each Parameter's Uncertainty Contribution to the System Attributes for FCV Failed Open



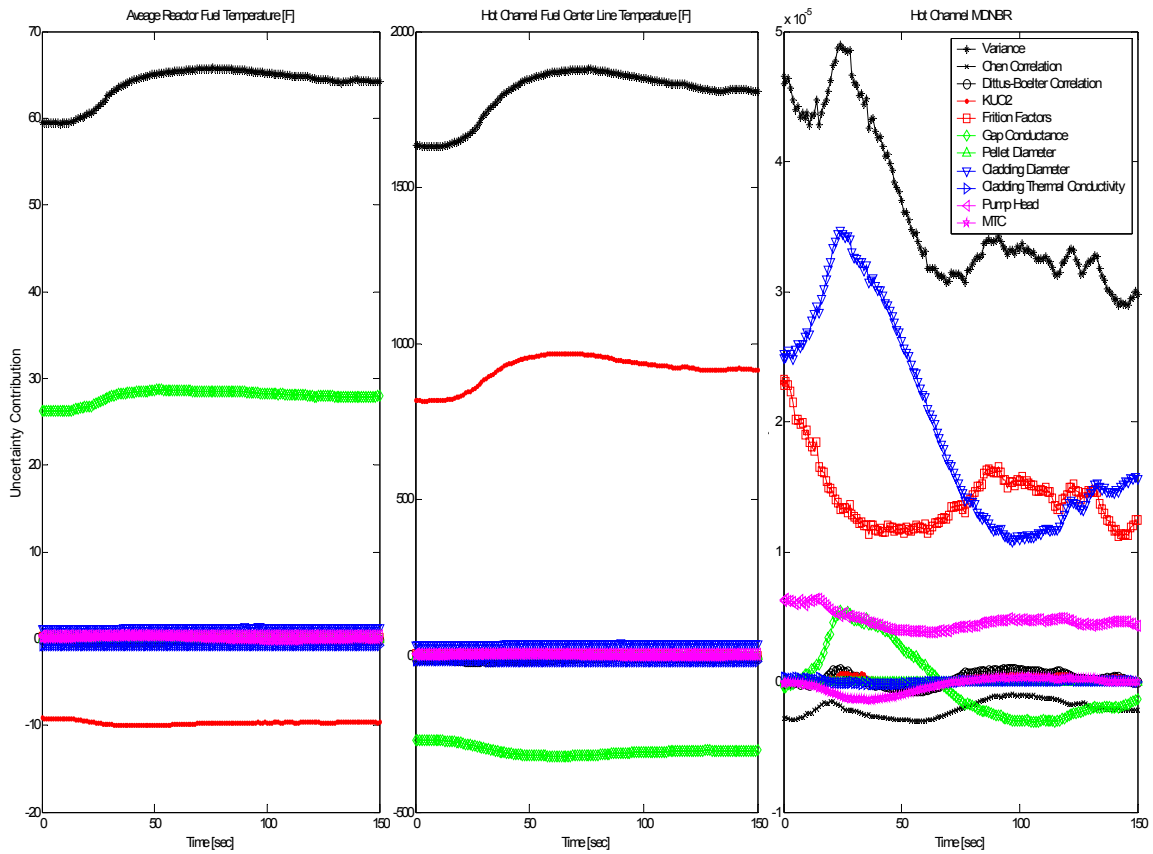


Figure 25. Each Parameter's Uncertainty Contribution to the System Attributes for TCV Failed Open

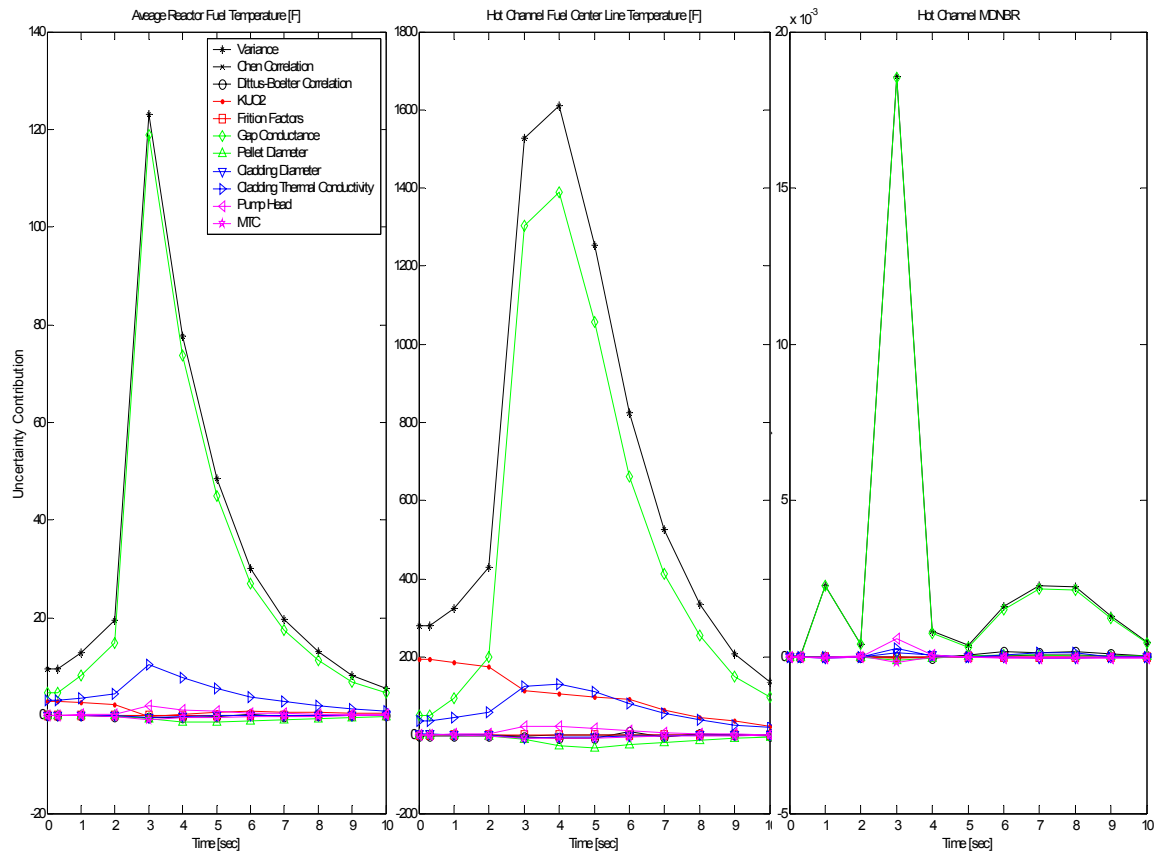


Figure 26. Each Parameter's Uncertainty Contribution to the System Attributes for RCP Trip as a Result of Multiple Experiments

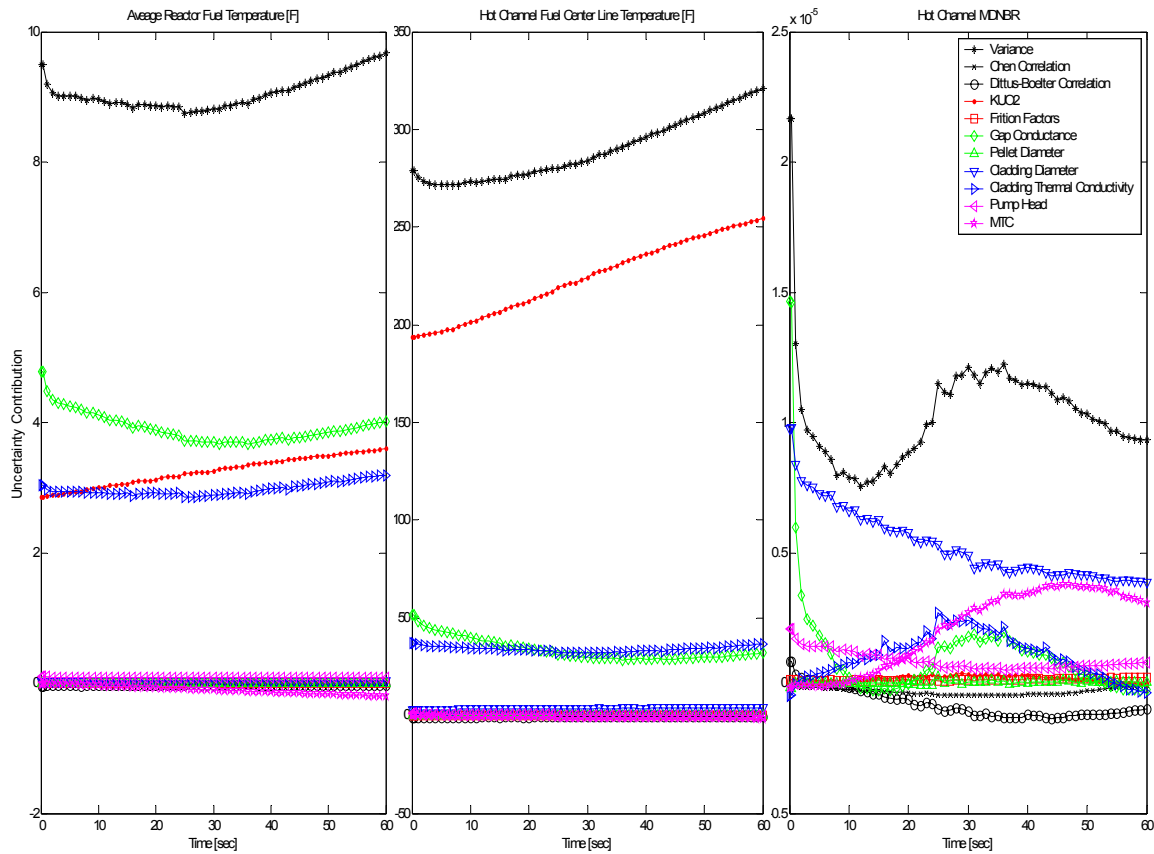


Figure 27. Each Parameter's Uncertainty Contribution to the System Attributes for Control Bank Withdrawal as a Result of Multiple Experiments

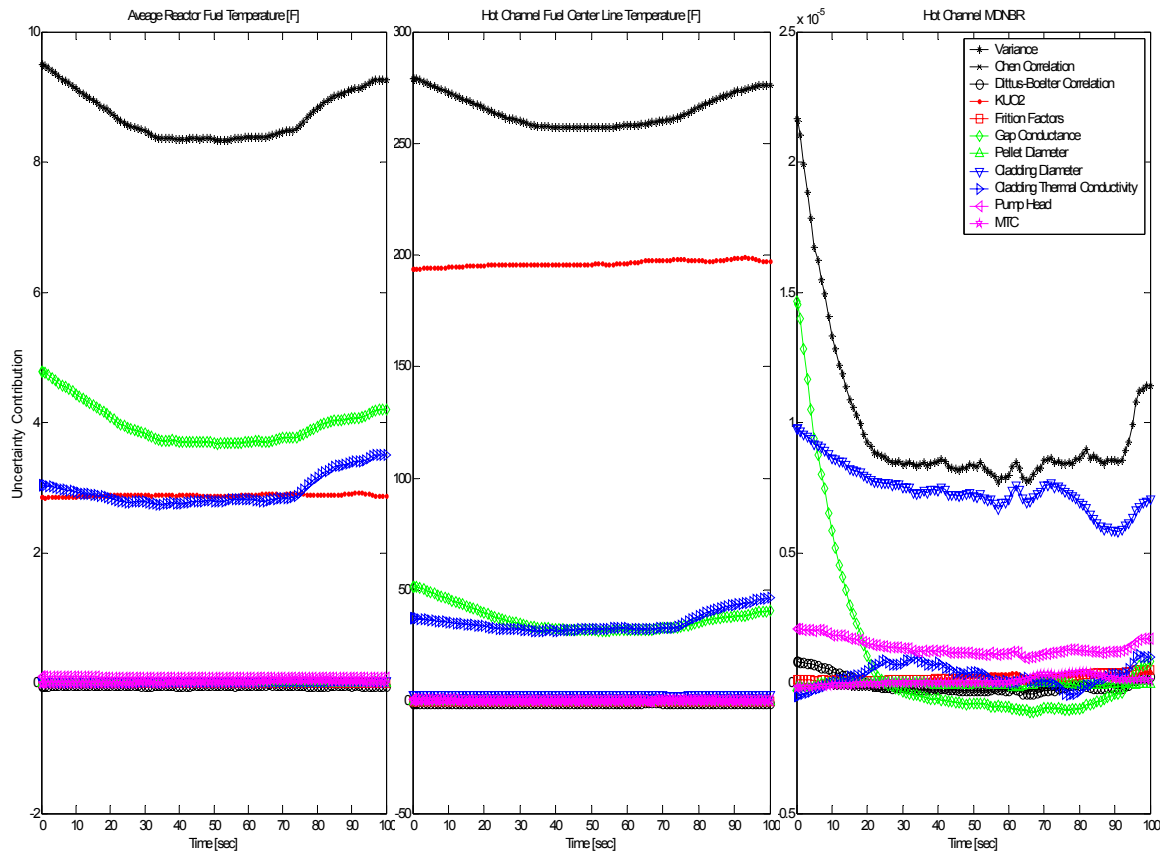


Figure 28. Each Parameter's Uncertainty Contribution to the System Attributes for FCV Failed Open as a Result of Multiple Experiments

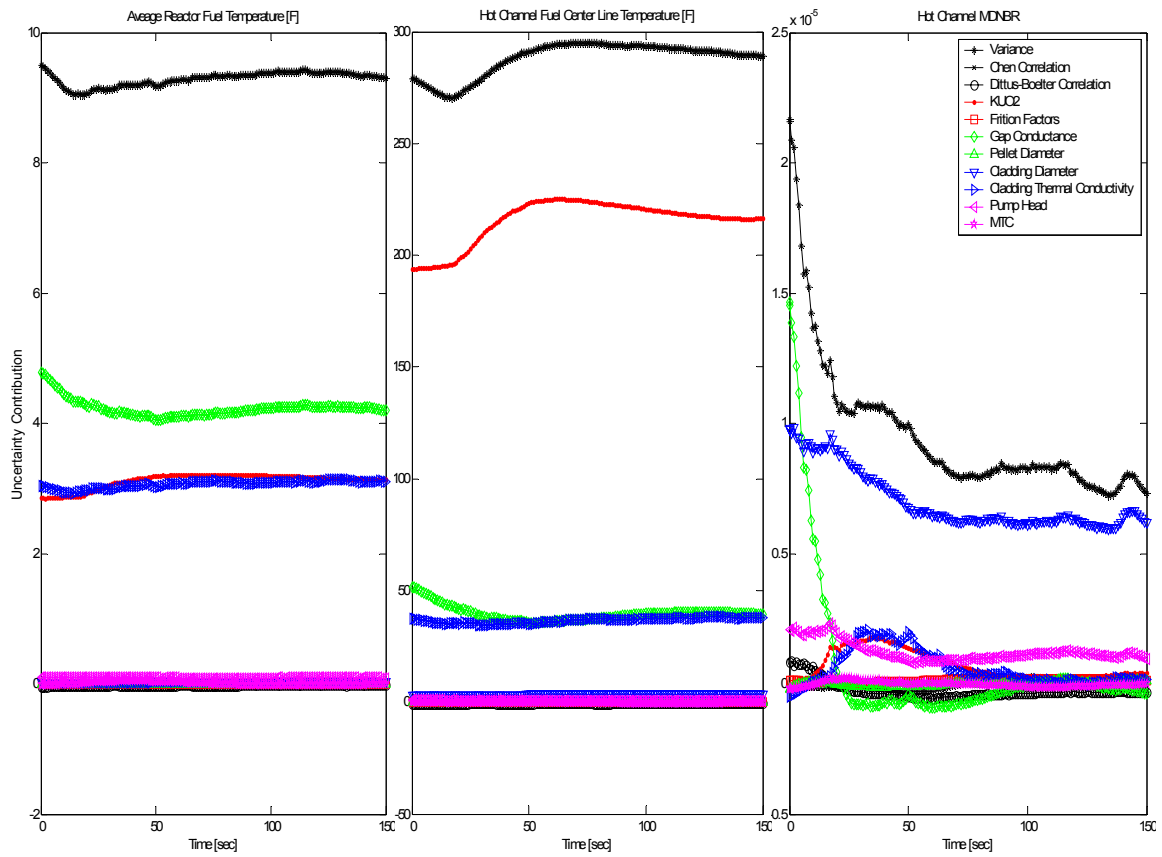


Figure 29. Each Parameter's Uncertainty Contribution to the System Attributes for TCV Failed Open as a Result of Multiple Experiments

### 3. 4. MCMC Simulation

The MCMC simulation was completed for the reactor coolant pump trip transient simulation for which one observed relatively large Chi-Squared values. To obtain a posteriori parameter distribution, the true solution vector  $\bar{e}$  was used for the virtual experiment model, which differs from the previous adaptation. Figure 30 represents the accepted parameter values during the MCMC iteration for the RCP trip at 30% power transient. It shows that the chain starts at random numbers and oscillates around the true solution vector. Figure 31 presents the a posteriori distribution of the parameters using RCP trip at 30% power which was computed using about 2000 MCMC samples. As observed, uncertainties are reduced, but non-Gaussian distributions are observed as well due to the nonlinearity of the system. The a posteriori distributions of the parameters using RCP trip at 80% power which would be prohibited due to safety concerns was calculated for comparison and it is presented in Figure 32. Due to the nonlinearity dependency on power level, the shape of the distributions are not identical, but the standard deviations are not much different (see Table VII), which implies that one can infer the parameter uncertainties at normal operating power from those at lower power level.

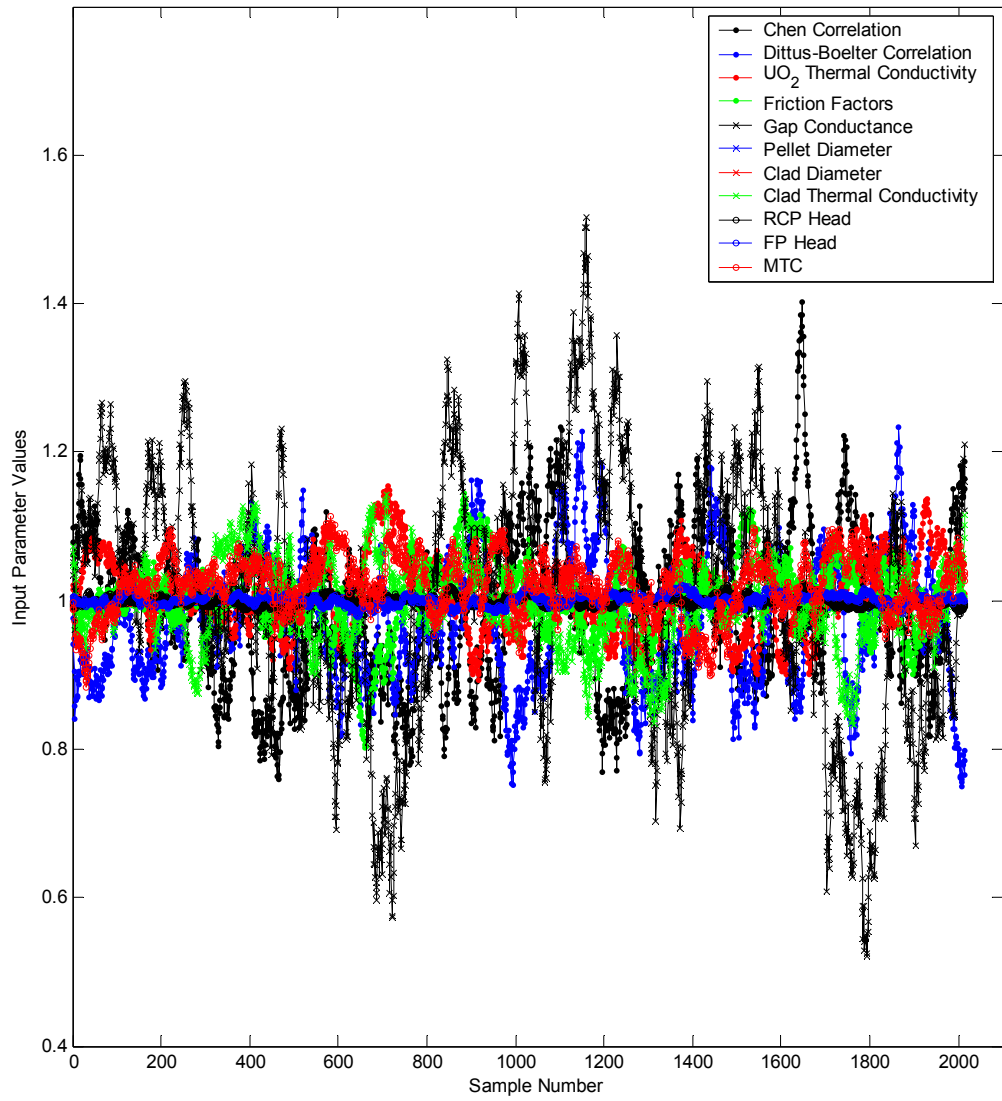


Figure 30. Accepted input parameter vector samples

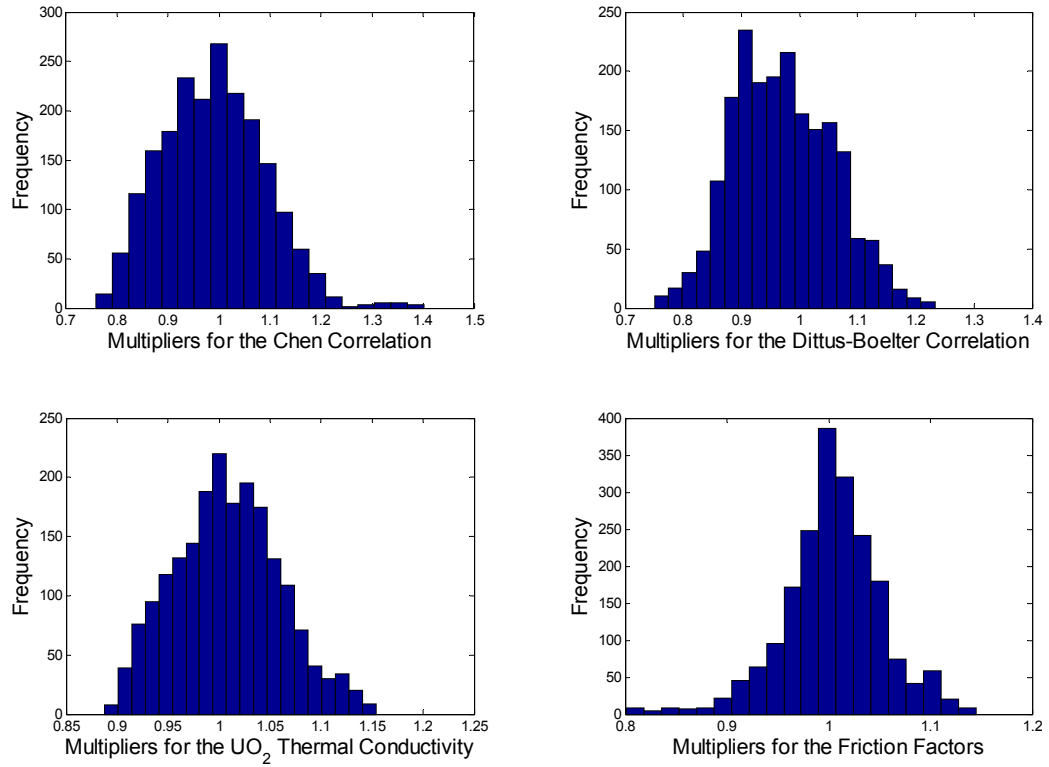


Figure 31. A posteriori distribution of the parameters using RCP Trip at 30% Power



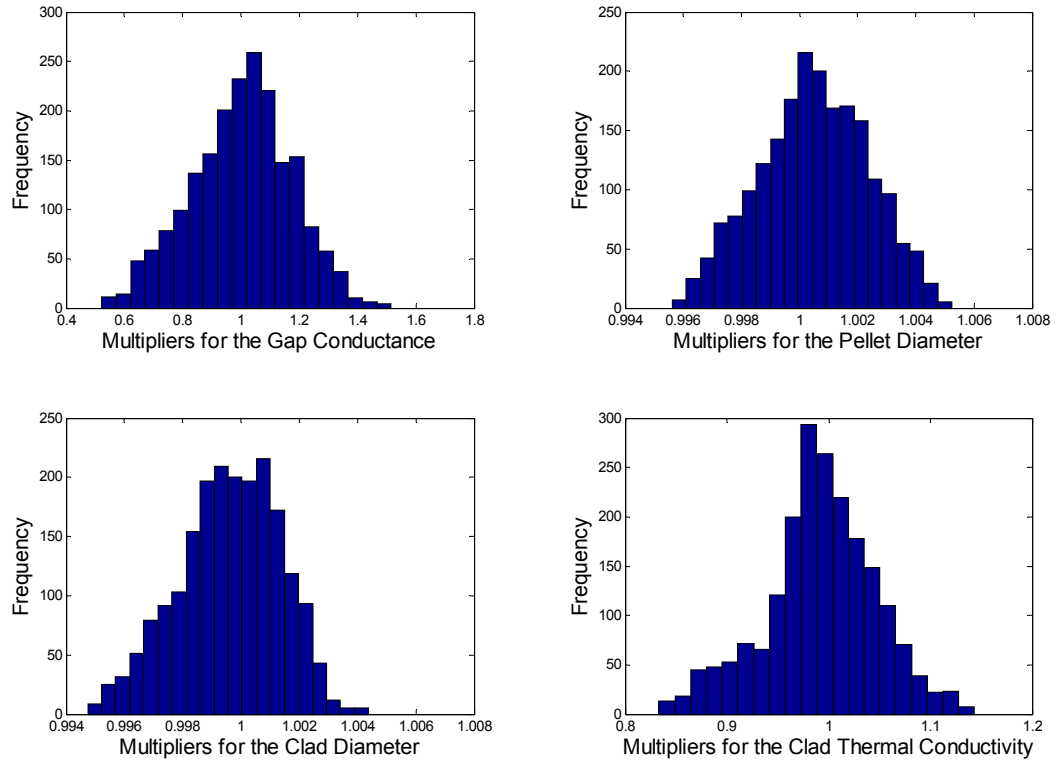


Figure 31. A posteriori distribution of the parameters using RCP Trip at 30% Power (Cont.)

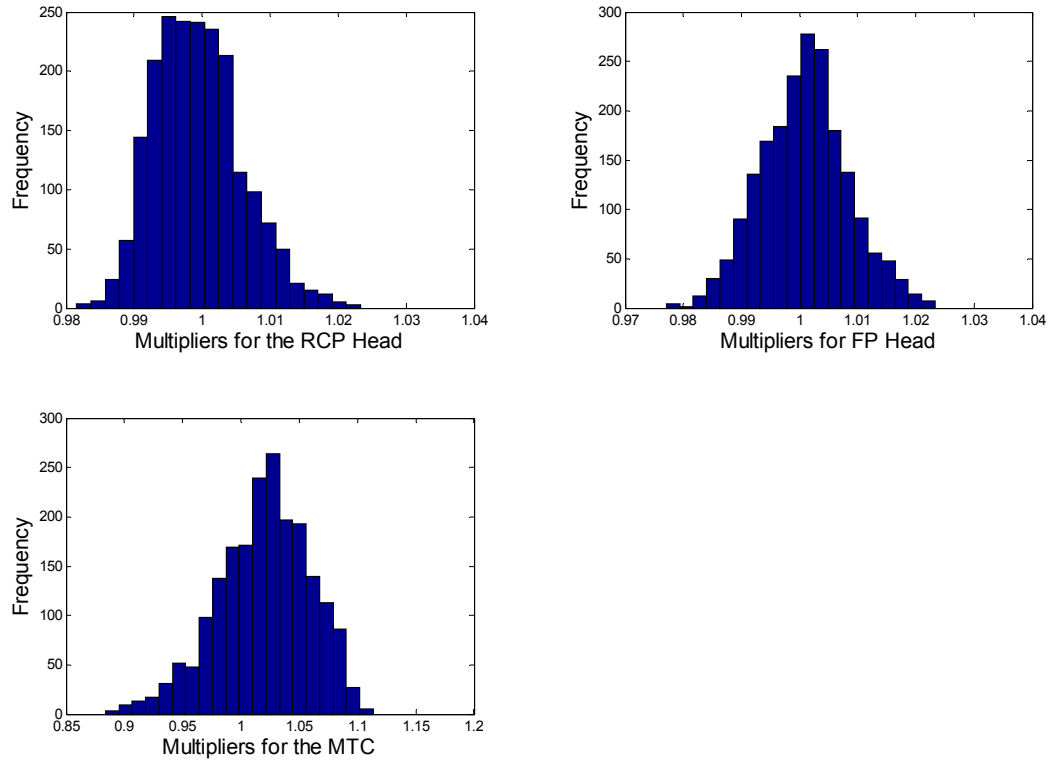


Figure 31. A posteriori distribution of the parameters using RCP Trip at 30% Power (Cont.)

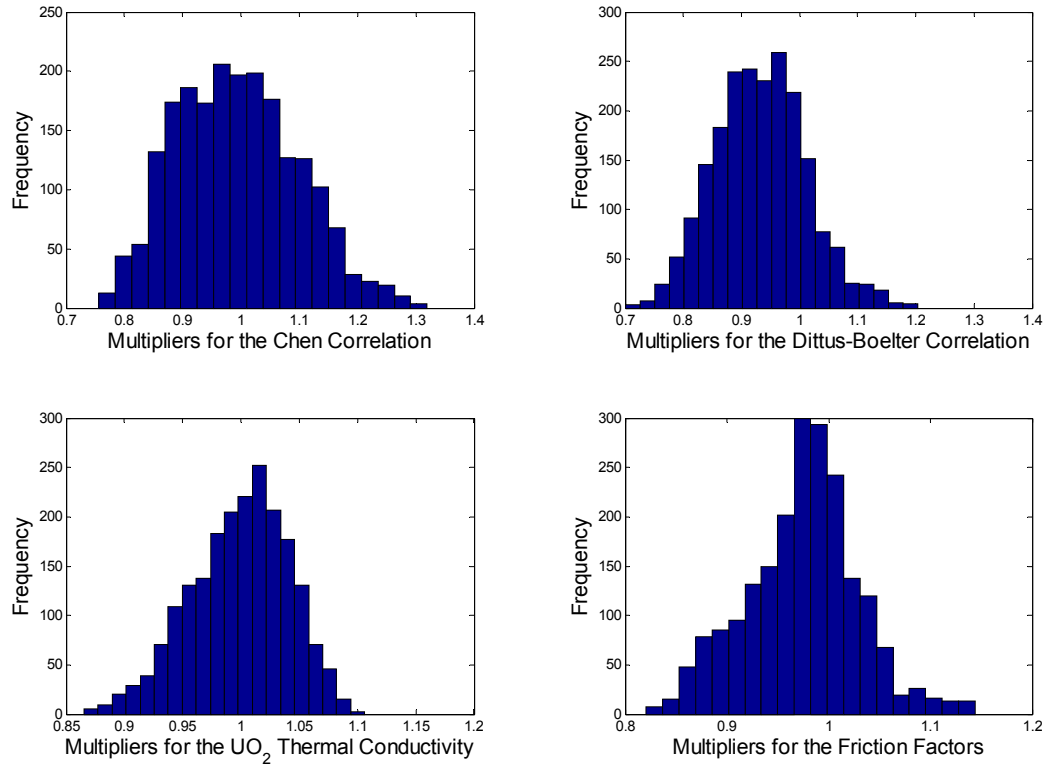


Figure 32. A posteriori distribution of the parameters using RCP Trip at 80% Power

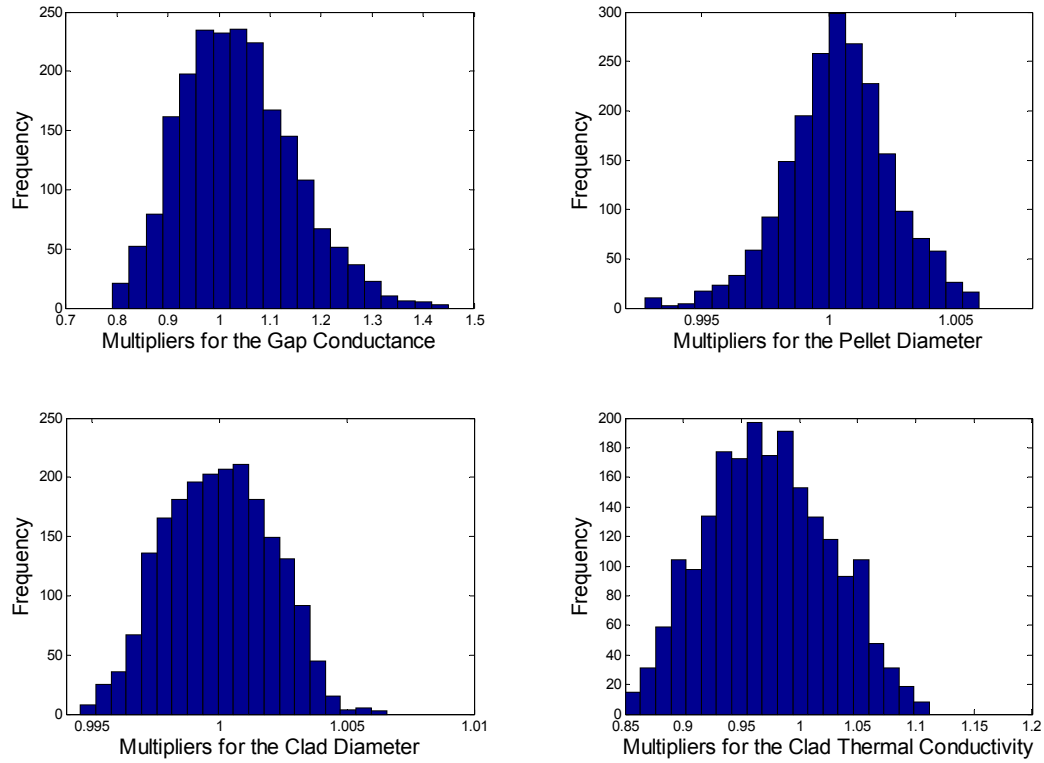


Figure 32. A posteriori distribution of the parameters using RCP Trip at 80% Power (Cont.)

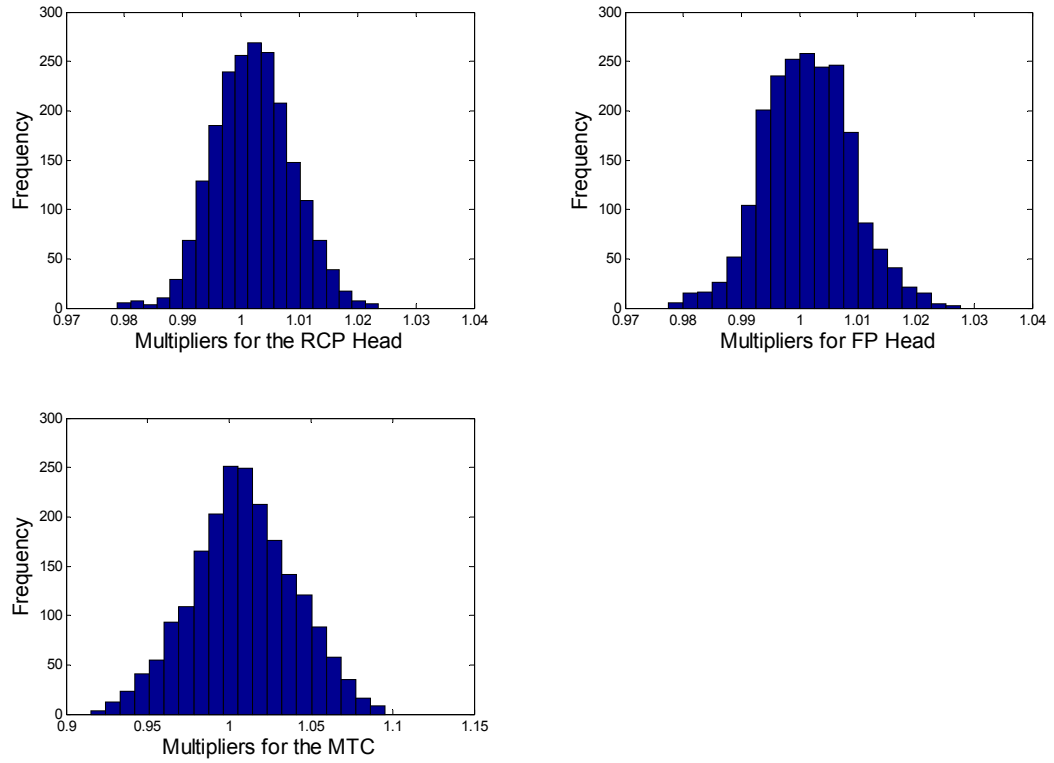


Figure 32. A posteriori distribution of the parameters using RCP Trip at 80% Power (Cont.)

Table VII. A Posteriori Standard Deviations for the Input Parameters using Experiment A for  
MCMC Simulation

Parameter	A Posteriori Standard Deviation	
	Power Level	
	30%	80%
Chen Correlation	0.100181	0.104268
Dittus-Boelter Correlation	0.085573	0.078787
UO <sub>2</sub> Thermal Conductivity	0.051501	0.041972
Friction Factors	0.048655	0.054668
Gap Conductance	0.162357	0.110800
Pellet Diameter	0.001872	0.002078
Clad Diameter	0.001736	0.002068
Clad Thermal Conductivity	0.054656	0.052626
RCP Head	0.006460	0.006667
Feed Pump Head	0.007458	0.007553
MTC	0.039474	0.031353

### 3. 5. Design Optimization

Simulated annealing was implemented to obtain the maximum savings offset by the experiment and sensor costs, and to determine the decision variables that optimize the objective function subject to the limitation imposed by the safety constraint. For the design optimization of the IRIS reactor, a binary 0/1 problem that has 4 experiments and 8 sensors was considered. In addition, three decision variables, power rating, steam generator tube length and RCP size, were considered for the suboptimization problem, i.e. the inner iteration. The safety limits are determined based on the assumption that the original system is tightly designed using all the safety margins, i.e. the safety limits are defined by Equation (2.42). One begins by setting the cost of the entire IRIS power plant equal to \$1.6 billion and

the cost of the NSSS at 30% of the total cost. The steam generator and the RCP cost are then assumed to be 50% and 25% of the NSSS cost, respectively. Figure 33 shows the result of the reactor system optimization using the a priori safety margins for the original reactor system. Figure 34 shows associated constraint violations during the simulated annealing procedure. Initially one allows the system to violate the safety constraints by giving small penalty function multipliers as is shown in Figure 34, and subsequently increases the multipliers to remove constraint violations so as to achieve feasible solutions. One can confirm that the constraint violation is removed, i.e. the penalty function converges to zero, as the inner objective function converges to its optimum value. In this case the objective function converges to zero, which implies that one will not have any benefit by redesigning the original reactor system using the same degree of design freedom. It is also confirmed that the decision variables stay almost identical to the original design specs. The power rating, steam generator tube length and RCP size for the original system are 334.98MWe, 100% and 100%, respectively, and for the best altered design specs are 335.74MWe, 98.29% and 103.56%, respectively.

Figure 35 presents the solution of the suboptimization problem using all experiments and sensors for data assimilation, and Figure 36 shows associated constraint violations for the accepted samples during the simulated annealing process. The objective function reaches its maximum value as the constraint violations converge to zero at the end of the simulation. These two extreme examples illustrate that the savings will increase as more sensors are used

and more experiments are conducted, since additional experimental data reduces a posteriori system attribute uncertainties so that it creates the larger degree of design freedom.

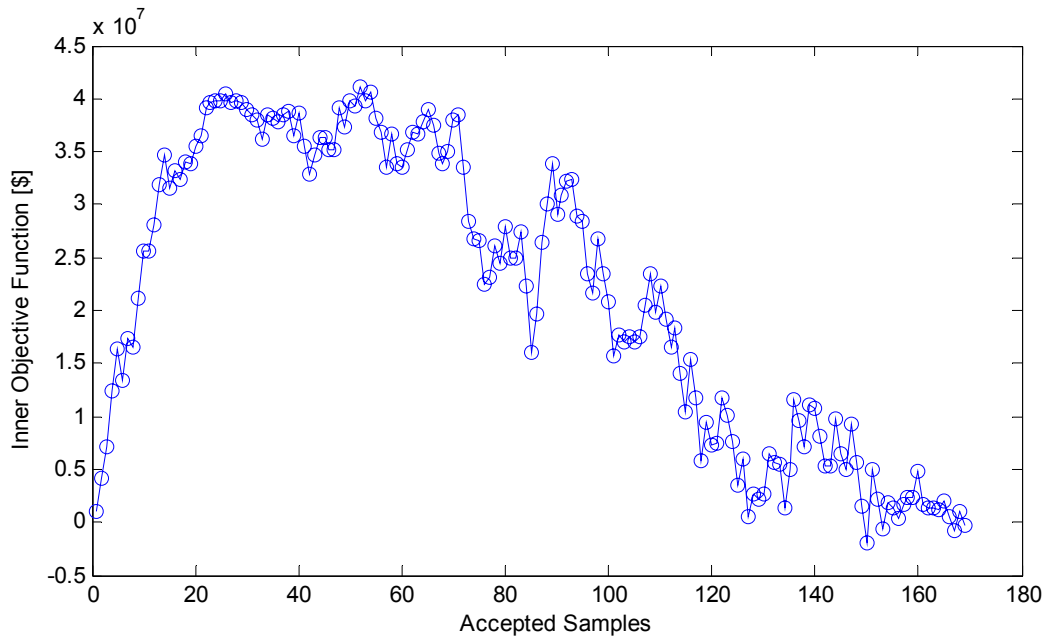


Figure 33. Inner Optimization using A Priori Design Margin



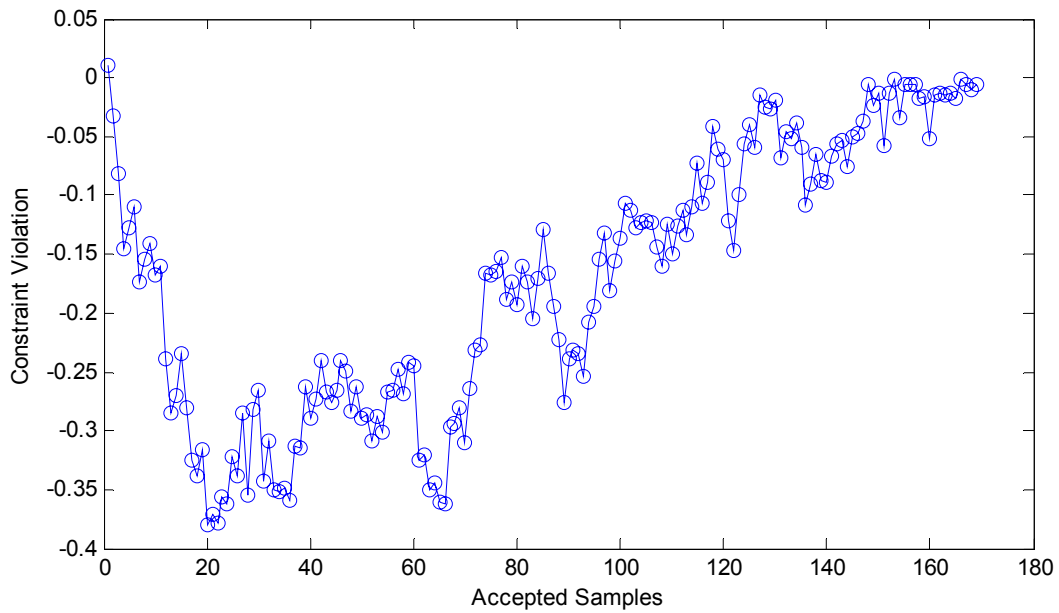


Figure 34. Constraint Violation for Inner Optimization using A Priori Design Margin

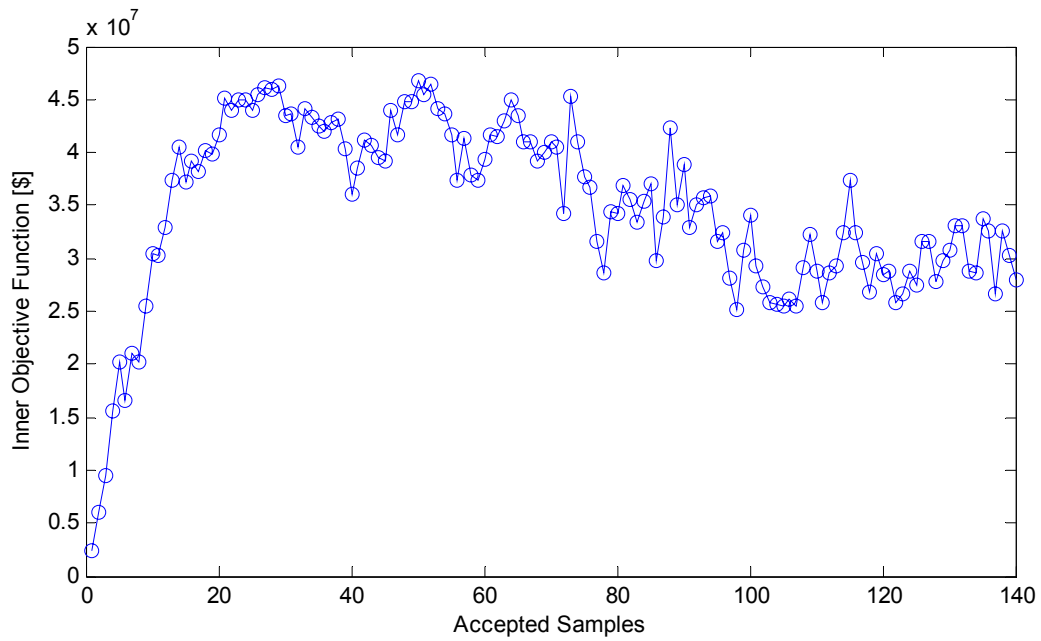


Figure 35. Inner Objective Function using All Experiments and Sensors for Data Assimilation

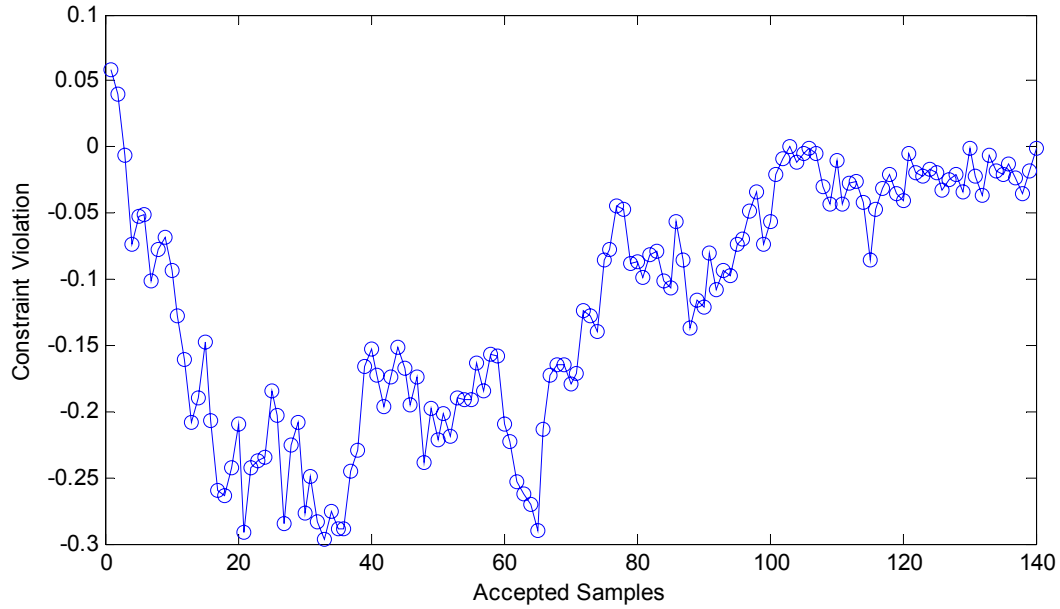


Figure 36. Constraint Violation for Inner Objective Function using All Experiments and Sensors for Data Assimilation

Figure 37 shows the solution of the optimization problem, i.e. the outer objective function, obtained by carefully annealing the solution space. The initial temperature was set high to allow wide solution space exploration, and the system was cooled down as the search progresses. This annealing schedule allows large jumps of the objective function during the initial search and makes the solution converge to the maximum point (about \$26,000,000) as the temperature decreases. If the cooling is done too rapidly, the solution can become trapped in local maxima. The result indicates the optimum Sensors and experiments which maximize savings are  $\bar{l} = \{\text{Neutron Power, Reactor Thermal Output, Core Flow Rate, Steam Pressure}\}$  and  $\bar{x} = \{\text{RCP Trip, FCV Failed Open, TCV Failed Open}\}$ , and associated decision variables

are 349.63MWe, 94.26% and 92.05% for the power rating, the steam generator tube length and the RCP size, respectively.

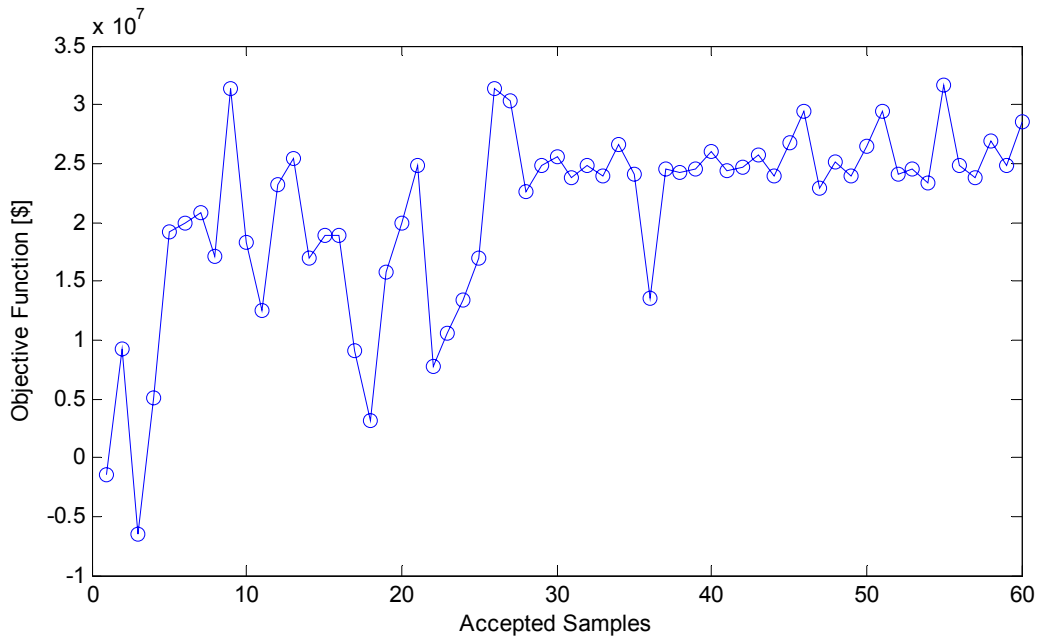


Figure 37. Objective Function for Outer Iteration

### 3. 6. Uncertainty Analysis for Reactor Control

The 10% step load changes at 70% and 90% power, and 20% ramp load changes at 70% power with ramp rate of 15%/min [29] were simulated with different gains. The following five observables were used to calculate the control ability objective, previously defined by Equation (2.53) and denoting the deviation from the desired state:

1. Neutron Power
2. Reactor Thermal Output
3. Feed Flow Rate per Steam Generator

#### 4. Steam Flow Rate per Steam Generator

#### 5. Turbine Output

The same five observables are used to determine the operational constraint, previously defined by Equation (2.55) and denoting the ability to stay within a desired control band. The desired control bands were subjectively selected and are presented in Table IX and XII. Four different algorithms are created by modifying gains and/or reactor control parameters as follows:

##### 1. Algorithm F1Q1:

FCV gains = {0, 0.05, 0.07}

Minimum Rod Speed = 3.75 inches/min

##### 2. Algorithm F2Q1:

FCV gains = {0, 0.01, 0.014}

Minimum Rod Speed = 3.75 inches/min

##### 3. Algorithm F3Q1:

FCV gains = {0, 0.0025, 0.0035}

Minimum Rod Speed = 3.75 inches/min

##### 4. Algorithm F1Q2:

FCV gains = {0, 0.05, 0.07}

Minimum Rod Speed = 0.75 inches/min

Tables VIII and IX present the deviations and the operational constraint probabilities, respectively, for the 10% step load changes. Table IX shows that as FCV gains increase it

generates larger deviations for the primary side observables, but smaller deviations for the secondary side responses. This is because wild feed control which results from the large FCV gains leads the primary side responses to overshoot while the secondary side responses usually follow the feed flow rate (see Figures 38, 39, 40 and 41). In order to reduce the size of overshoot, minimum rod speed was modified, denoted as Algorithm F1Q2, and uncertainty analysis was performed. The results for this analysis are presented in Tables VIII and IX for comparison, which indicates that substantial reductions in the deviations on the responses can be achieved through reducing the minimum rod speed. The deviations and the operational constraint probabilities for the 20% ramp changes are presented in Tables XI and XII. They show a similar behavior to the 10% step load change. The optimum control algorithm in terms of the deviations is F1Q2 as well. The safety constraint, previously defined in Equation (2.54), was also calculated for the MDNBR assuming that the safety limit is 3.6 and is presented in Table X and XIII. The value of 3.6 assures that if a loss of coolant accident initiates during a normal operating maneuver, there is sufficient DNB margin so that the MDNBR does not violate its safety limit during this accident.

Table VIII. Deviations for 10% Step Load Changes at 70% and 90% Power using Four Different Control Algorithms

Initial Power	Algorithm Index	Deviations
70%	F1Q1	0.007221
	F2Q1	0.008383
	F3Q1	0.012264
	F1Q2	0.005635
90%	F1Q1	0.004561
	F2Q1	0.005135
	F3Q1	0.011475
	F1Q2	0.002480

Table IX. Operational Constraint Probabilities for 10% Step Load Changes at 70% and 90% Power using Four Different Control Algorithms

Observable Index		1	2	3	4	5
$\Delta r_j$		50 MWt	50 MWt	25000 lbm/hr	25000 lbm/hr	15 MW
Initial Power	Algorithm Index	Operational Constraint Probabilities				
70%	F1Q1	0.6066	0.6268	0.9784	0.9086	0.9107
	F2Q1	0.7668	0.8041	0.9423	0.8034	0.8199
	F3Q1	0.7874	0.7651	0.7684	0.6980	0.6399
	F1Q2	0.8864	0.8805	0.9811	0.8711	0.8874
90%	F1Q1	0.7713	0.7757	0.9681	0.9303	0.9430
	F2Q1	0.8598	0.8467	0.8455	0.7997	0.8466
	F3Q1	0.6925	0.6542	0.5049	0.5024	0.4516
	F1Q2	0.9100	0.9027	0.9705	0.9306	0.9480

Table X. Safety Constraint Probabilities for 10% Step Load Changes at 70% and 90% Power using Four Different Control Algorithms

Initial Power	Algorithm Index	Safety Constraint Probabilities
70%	F1Q1	1.0000
	F2Q1	1.0000
	F3Q1	1.0000
	F1Q2	1.0000
90%	F1Q1	0.9000
	F2Q1	0.9500
	F3Q1	1.0000
	F1Q2	0.8600

Table XI. Deviations for 20% Ramp Load Changes at 70% Power using Four Different Control Algorithms

Initial Power	Algorithm Index	Deviations
70%	F1Q1	0.009937
	F2Q1	0.008618
	F3Q1	0.042307
	F1Q2	0.006269

Table XII. Operational Constraint Probabilities for 20% Ramp Load Changes at 70% Power using Four Different Control Algorithms

Observable Index		1	2	3	4	5
$\Delta r_j$		50 MWt	50 MWt	25000 lbm/hr	25000 lbm/hr	15 MW
Initial Power	Algorithm Index	Operational Constraint Probability				
70%	F1Q1	0.5760	0.5827	1.0000	0.9992	0.9789
	F2Q1	0.6033	0.6564	0.9308	0.7848	0.7310
	F3Q1	0.6818	0.6519	0.5548	0.4548	0.4404
	F1Q2	0.7726	0.7793	1.0000	0.9999	0.9626

Table XIII. Safety Constraint Probabilities for 20% Ramp Load Changes at 70% Power using  
Four Different Control Algorithms

Initial Power	Algorithm Index	Safety Constraint Probabilities
70%	F1Q1	1.0000
	F2Q1	1.0000
	F3Q1	1.0000
	F1Q2	1.0000



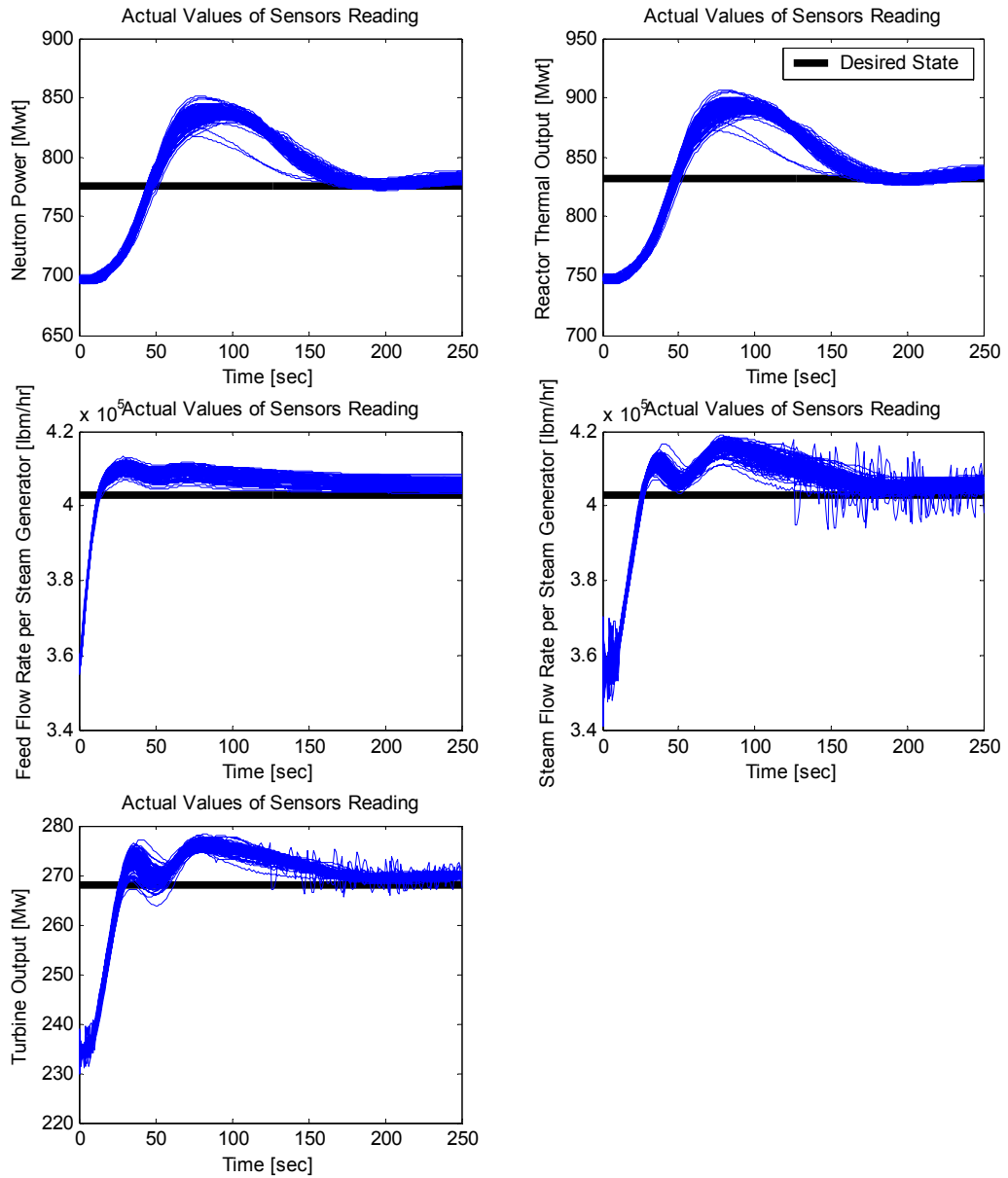


Figure 38. System Responses obtained Simulating 100 Samples for 10% Step Load Changes at 70% Power using Control Algorithm F1Q1 for Uncertainty Analysis

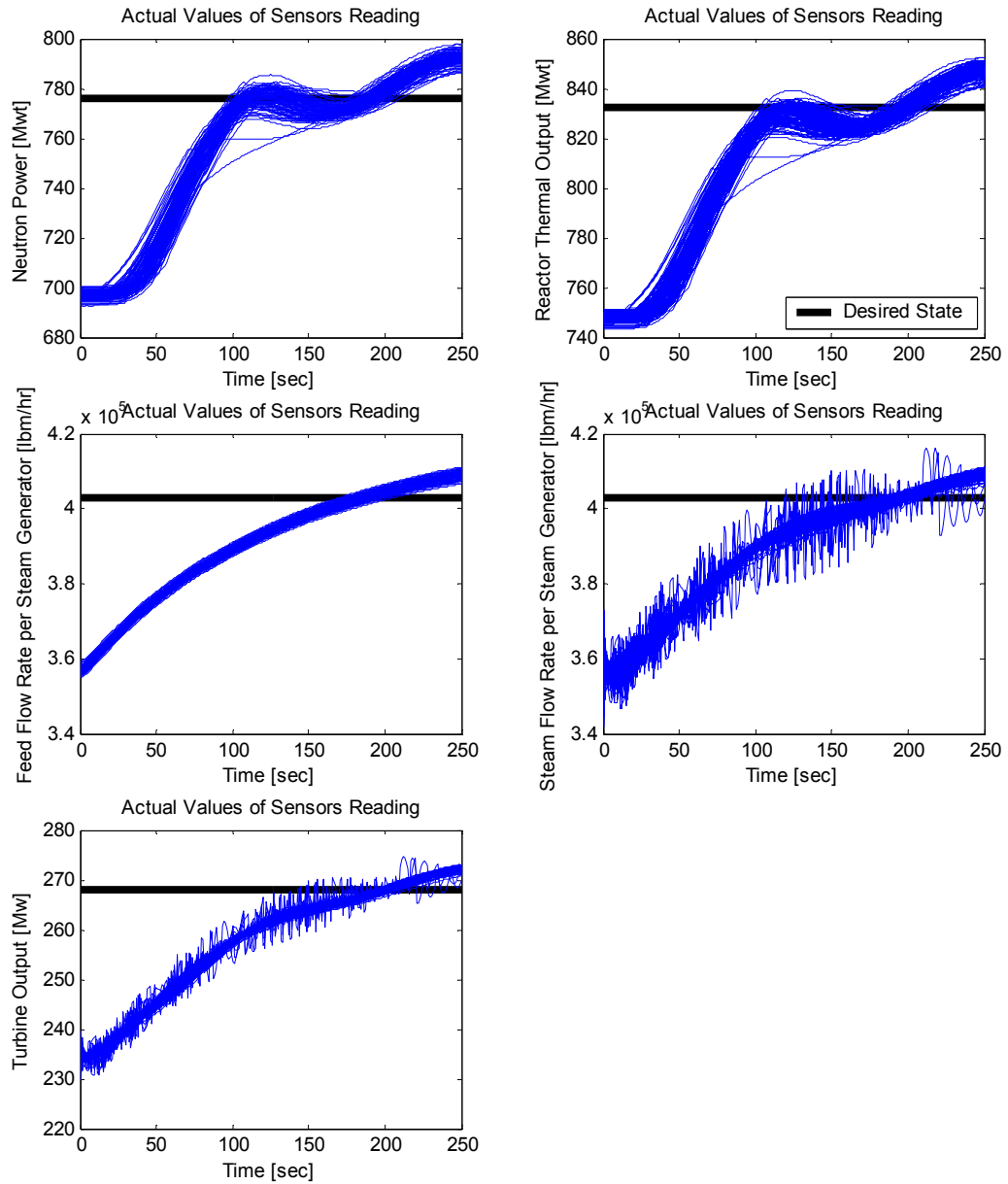


Figure 39. System Responses obtained Simulating 100 Samples for 10% Step Load Changes at 70% Power using Control Algorithm F3Q1 for Uncertainty Analysis

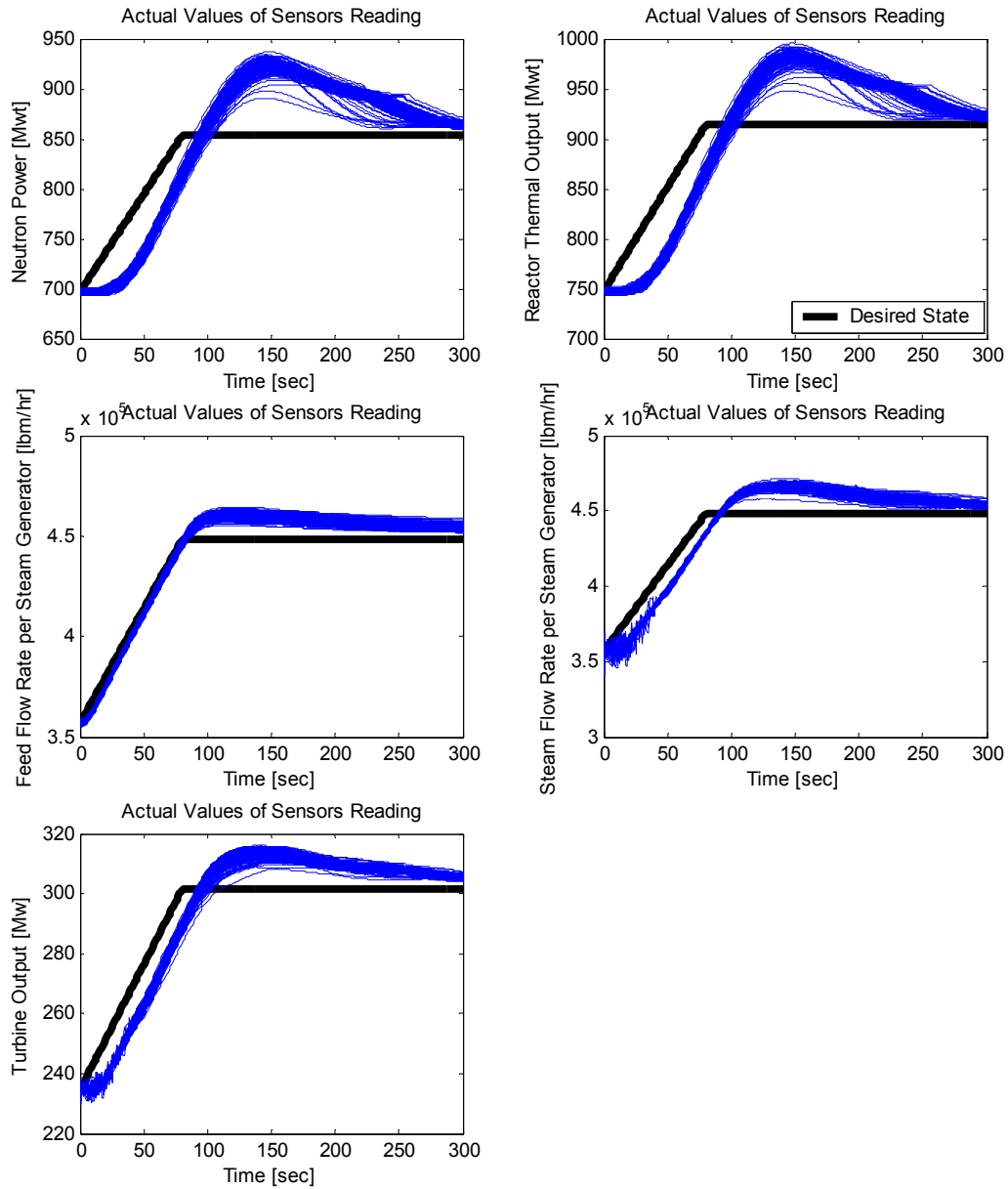


Figure 40. System Responses obtained Simulating 100 Samples for 20% Ramp Load Changes at 70% Power using Control Algorithm F1Q1 for Uncertainty Analysis

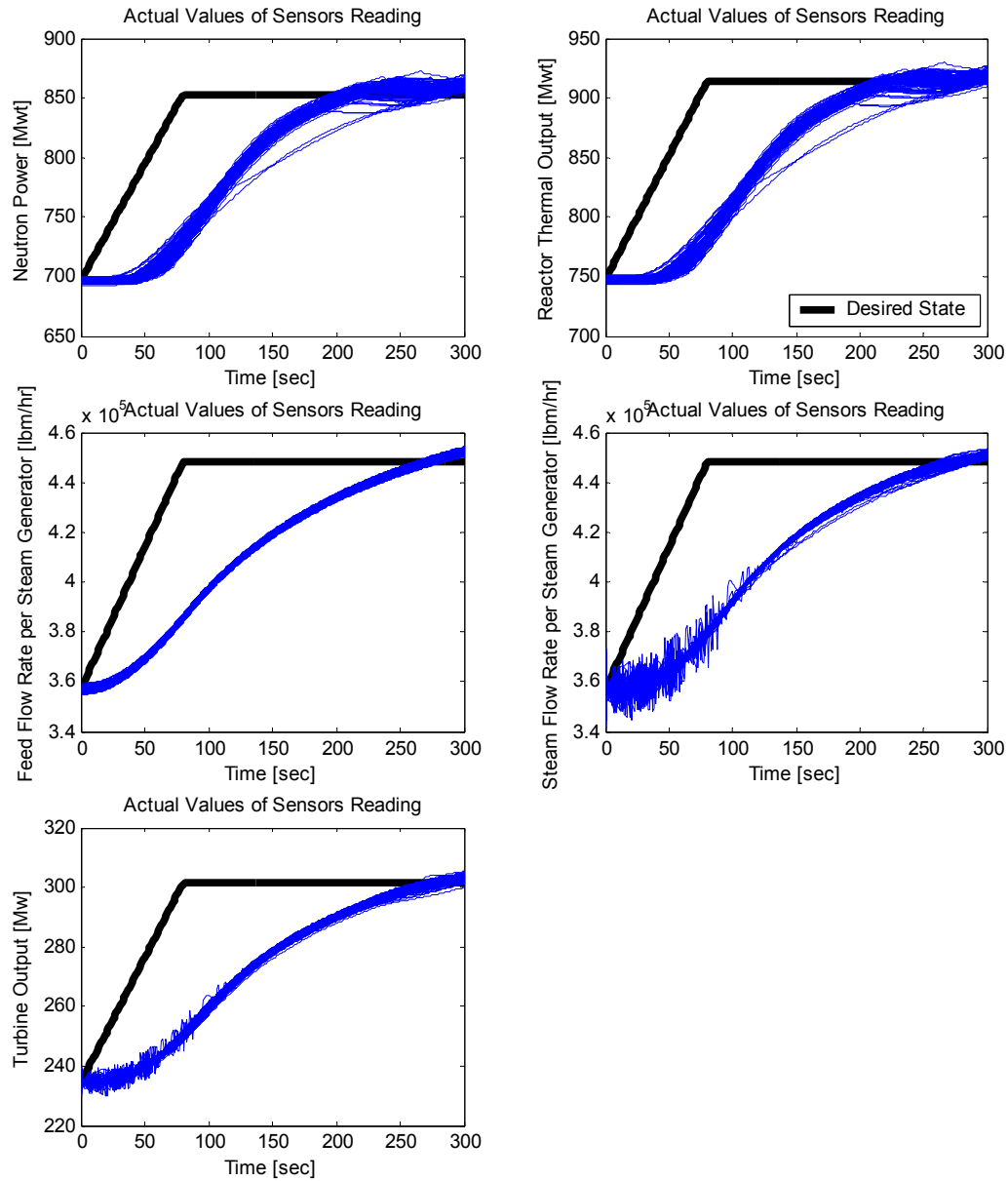


Figure 41. System Responses obtained Simulating 100 Samples for 20% Ramp Load Changes at 70% Power using Control Algorithm F3Q1 for Uncertainty Analysis

#### 4. Conclusions and Recommendations for Future Work

The goal of this work is to optimize the thermal hydraulic reactor system for an SMR by completing experiments using the SMR, doing data assimilation to reduce the simulation code's input parameters uncertainties, and subsequently simulation code's prediction uncertainties of design constraining responses, and finally using the margin reductions obtained to reoptimize the SMR for a next generation design. Also, the operational space of the current generation of SMR could be enlarged due to the enhanced margins. Thermal hydraulic parameters were adjusted for both mildly nonlinear and highly nonlinear transients, and their a posteriori parameter uncertainties were propagated through the simulation model to predict a posteriori uncertainties of the key system attributes. To solve both highly nonlinear as well as mildly nonlinear problem, both deterministic and probabilistic methods were used to complete data assimilation and uncertainty quantification. In order to accomplish this, the Bayesian approach modified by regularization is used to incorporate available information in quantifying uncertainties for the SMR, which was IRIS reactor system. The a priori information considered are the parameters and the experimental data together with their uncertainties. To determine the experimental data which do not exist, a virtual experiment model was developed and the following four experiments were simulated using the IRIS system simulation code: RCP Trip at 30% and 80% Power, Control Bank Withdrawal at 70% Power, Feed Control Valve Failed Open at 15% Power, and Turbine Control Valve Failed Open at 15% Power. Each parameter's uncertainty contribution to the system attributes was also calculated to identify major sources of uncertainty. The results indicate that substantial reductions in uncertainties on the system attributes can be achieved

with experimental data through refining input parameter uncertainty distributions. Some of the adapted parameters are not in good agreement with their known values, i.e. the virtual experiment model parameters, if those parameters affect the observables in a similar way and/or if they produce small sensitivities. Also, due to the input parameters that have highly correlated response sensitivities, it is shown that the errors can increase as more experimental data are added. However the uncertainties propagated from a posteriori parameter distributions will be correct as long as those parameters generate similar responses for the system attributes during accident transients. The MCMC simulation was completed for the highly nonlinear transient, i.e. reactor coolant pump trip transient in this research. Due to the computational burden, this method would not be applicable if there are too many parameters, but it can provide the best solution since the algorithm does not approximate the responses while the deterministic approach linearizes, i.e. approximates, the responses using a first-order Taylor series expansion. As a result of the simulation, nonGaussian a posteriori distributions of the parameters, with reduced uncertainties on them, were obtained due to the nonlinearity of the system.

Based on the reduced a posterior system attribute uncertainties, an optimization problem was formulated and solved using the simulated annealing method to maximize economic saving through redesign of IRIS features, while maintaining safety margin. The optimization problem decision variables for the outer iteration include the selection of sensor and experiment type with the objective of maximizing the economic savings achieved by the suboptimization of IRIS features using the larger degree of design freedom created by data

assimilation, offset by the cost of sensors and experiments. Power rating, steam generator tube length and RCP size are selected for the suboptimization problem decision variables, i.e. inner iteration decision variables, with the objective of maximizing the economic savings, constrained by the safety criteria. The result shows that one can obtain savings by redesigning the reactor system using the reduced uncertainties on the key system attributes. Needless to say, the amount of savings is highly dependent upon the cost data utilized. Since the cost data needed is estimated in this work, the value of savings presented is itself uncertain.

The uncertainty analysis was conducted for reactor control problems by formulating an objective function to minimize together with imposing the safety and operational constraints. The IRIS simulation code was reviewed to identify the control algorithms in the simulator, and the gains or the shim which controls trajectories of the system responses were perturbed to generate several different control algorithms. The optimum control algorithm which minimizes the time integrated deviation of the actual state from the desired state was identified by creating and testing multiple control algorithms for the step load change and ramp load change transient.

A recommendation for future work is to perform data assimilation for a neutronic and thermal hydraulic coupled model. The probabilistic method, e.g. MCMC, provides the best solution for not only mildly nonlinear but also highly nonlinear problems, but it is usually not applicable to a neutronic problem that has multiple parameters due to the demanding

calculational requirements. It may be tractable on a HPC but certainly is beyond the capabilities of current generation PCs if the simulation model requires substantial CPU time per sample to execute. The deterministic method is known to be computationally efficient for large scale systems, e.g. reactor physics problem, since efficient methods to obtain sensitivities exist, but inapplicable for highly nonlinear thermal hydraulic system transients. Thus it is desired to develop a hybrid uncertainty quantification method for neutronic and thermal hydraulic coupled problems to perform an efficient calculation. For the neutronic parameters adjustment, a deterministic approach can be used to deal with the linear system that has many parameters. For the thermal hydraulic parameters calibration, a probabilistic approach can be utilized to solve the nonlinear system with a relatively small number of parameter. For this analysis, one should pay attention to the correlation between the neutronic and the thermal hydraulic parameters since the reactor system is always affected by those parameters simultaneously.

Since the cost values associated with instrumentation and conducting experiments were estimated, their values should be refined and the optimization recompleted. Likewise, the cost values associated with the IRIS design modifications should be refined and used in the recompleted optimization.

An optimization should be completed with the objective of increasing the operating space without any changes to the IRIS NSSS design. The work presented in this dissertation simultaneously changed the operating space and IRIS NSSS design, so is applicable to only



future, modified designs. By restricting the optimization decision variables to only variables defining the operating space, the generation of the IRIS design that completes the experiments would reap benefits.

Only the parameters associated with the assumed currently used control systems were optimized in this study. The control system optimization study should be expanded to include not only control systems' parameters but also alternative control systems.

Not all parameters, including correlations, were addressed in the data assimilation. Data assimilation should be expanded to include all the important parameters, e.g. Weisman heat transfer coefficient for the reactor core.

The experiments simulated assumed that control systems were inactive to facilitate a more linear response to parameters allowing a more computationally efficient data assimilation approach to be employed. Data assimilation should be recompleted with control system active during the experiments. Now control system state, e.g. control bank position, valve position and pump speed, as a function of time, based upon their (virtual) measured values, would be input to the simulations used when performing data assimilation. This would facilitate a wider range of experiments allowed since the control systems would attempt to keep the reactor within normal operating conditions.

Finally, the work reported upon in this dissertation was performed using the NC State developed IRIS simulator. Given this simulator's computational efficiency and lack of precise knowledge of all the design specifications for IRIS, use of this simulator was appropriate. With more precise knowledge of the IRIS design specifications, it would be appropriate to utilize a simulator with the fidelity required to make design decisions in the optimizations.

## References

- [1] M. D. Carelli, "IRIS: Final Technical Progress Report," Westinghouse Electric Co., STD-ES-03-40, November 3, 2003.
- [2] H. Shen, "Advanced Feedwater Control for Next Generation Nuclear Power Systems," Ph.D. Dissertation, North Carolina State University, 2006.
- [3] J. M. Doster and P. J. Turinsky, "Advanced Instrumentation and Control Methods for Small and Medium Reactors with IRIS Demonstration - Final Report Volume 2: IRIS Simulator Development and Measurement Sensitivity Analysis," DE-FG07-07ID14895/UTNE/2011 - 4, May 2011.
- [4] B. E. Boyack, I. Catton, R.B. Duffey, P. Griffith, K. R. Katsma, G. S. Lellouche, S. Levy, U. S. Rohatgi, G. E. Wilson and N. Zuber, "Quantifying Reactor Safety Margins, Parts 1-6," Nuclear Engineering and Design, 119, 1, 1990
- [5] F. D'Auria, N. Debrecin and G. M. Galassi, "Outline of the Uncertainty Methodology based on Accuracy Extrapolation," J. Nuclear Technology, 109, 1, 21-38, 1995
- [6] C. Frepoli, K. Ohkawa and R. M. Kemper, "Realistic Large Break LOCA Analysis of AP1000 with ASTRUM," Proc. 6th International Conference on Nuclear Thermal Hydraulics, Operations and Safety (NUTHOS-6), Nara, Japan, Atomic Energy Society of Japan, 2004
- [7] A. De Crecy and P. Bazin, "BEMUSE Phase III Report - Uncertainty and Sensitivity analysis of the LOFT L2-5 Test," OECD/CSNI Report NEA/CSNI/R(2007)4, 2007
- [8] D. G. Cacuci, *Sensitivity and Uncertainty Analysis, Volume I*, CRC Press, 2000

- [9] H. S. Abdel-Khalik, "Adaptive Core Simulation," Doctoral Dissertation, North Carolina State University, 2004
- [10] M. A. Jessee, "Cross-Section Adjustment Techniques for BWR Adaptive Simulation," Doctoral Dissertation, North Carolina State University, 2008
- [11] A. Tarantola, *Inverse Problem Theory and Methods for Model Parameter Estimation*, Society for Industrial and Applied Mathematics, Philadelphia, 2005
- [12] D. G. Cacuci and M. Ionescu-Bujor, "Best-Estimate Model Calibration and Prediction Through Experimental Data Assimilation - I: Mathematical Framework," Nuclear Science and Engineering, 165, 18-44, 2010
- [13] J. W. Hines, B. R. Upadhyaya, J. M. Doster, R. M. Edwards, K. D. Lewis and P. J. Turinsky, "Advanced Instrumentation and Control Methods for Small and Medium Reactors with IRIS Demonstration," DE-FG07-07ID14895/UTNE/2010 -1, January 2010.
- [14] A. N. Tikhonov, *Numerical Methods for the Solution of Ill-Posed Problems*, Kluwer Academic Publishers, 1995
- [15] H. W. Engl and W. Grever, "Using the L-Curve for Determining Optimal Regularization Parameters," Numerische Mathematik, 69, 25, 1994
- [16] J. W. Hines, B. R. Upadhyaya, J. M. Doster, R. M. Edwards, K. D. Lewis and P. J. Turinsky, "Advanced Instrumentation and Control Methods for Small and Medium Reactors with IRIS Demonstration," DE-FG07-07ID14895/UTNE/2009 -4, October 2009.

- [17] Neil E. Todreas, Mujid S. Kazimi, *Nuclear Systems*, New York: Hemisphere Pub. Corp., 1990.
- [18] *RELAP5/MOD3 Code Manual Volume IV: Models and Correlations (Draft)*, EG&G Idaho, Inc., Idaho Falls, Idaho 83415, June 1990
- [19] Donald L. Hargman, *MATPRO - Version 11, A handbook of Materials Properties for Use in the Analysis of Light Water Reactor Fuel Rod Behavior*, EG&G Idaho, Inc., NUREG/CR-0497, February 1979
- [20] D. Higdon, M. Kennedy, J. C. Cavendish, J. A. Cafeo and R. D. Ryne, "Combining Field Data and Computer Simulation for Calibration and Prediction," *SIAM J. Sci. Comput.* Vol. 26, No. 2, pp. 448-466, 2004
- [21] A. Gelman, G. O. Roberts and W. R. Gilks, "Efficient Metropolis jumping rules," *Bayesian Statistics*, 5, 599-607, Oxford University Press, 1996
- [22] P. Muller, "A Generic Approach to Posterior Integration and Gibbs Sampling," 1993
- [23] K. M. Hanson and G. S. Cunningham, "Posterior Sampling with Improved Efficiency," *Proc. SPIE* 3338, 371-382, 1998
- [24] Duke Energy Company McGuire Nuclear Station, "Updated Final Safety Analysis Report," Rev 13, May 2007
- [25] Westinghouse Electric Company LLC, "IRIS Preliminary Safety Assessment, Volume I," WCAP-16082-NP, July 2003
- [26] S. Kirkpatrick, C. D. Gelatt and M. P. Vecchi, "Optimization by Simulated Annealing," *Science*, 220, 671-680, 1983

- [27] FORMOSA-B Code Methodology and Usage Manual - Version 3.2, North Carolina State University, 2004
- [28] B. Petrovic, D. Conti, G. D. Storrick, L. Oriani and L. E. Conway, "Instrumentation Needs for Integral Primary System Reactors (IPSRs)," Westinghouse Electric Company LLC, DE-FC07-05ID14690, September 2005
- [29] J. E. Ouzts, "Plant Startup Test Report - H. B. Robinson Unit No. 2, Volume I and II," Westinghouse Electric Corporation, WCAP-7844, January 1972
- [30] Kewaunee Nuclear Power Plant Safety Evaluation for Amendment No. 168 - Measurement Uncertainty Recapture Power Uprate

## Appendices

## Appendix A

This appendix derives the a posteriori parameter, response and covariance matrix expressions. For  $I$  total input parameters,  $J$  distinct responses, and  $T$  discrete times, the vector  $\bar{p}$  of parameters and the vector  $\bar{r}_j$  of each system response can be represented as follows:

$$\bar{p} = \{p_i | i=1, 2, \dots, I\}, \quad \bar{r}_j = \{r_j^{(t)} | t=1, 2, \dots, T\} \quad (\text{A.1})$$

Then the vector  $\bar{r}$  which contains all of the system response is:

$$\bar{r} = \begin{bmatrix} \bar{r}_1^T & \bar{r}_2^T & \dots & \bar{r}_J^T \end{bmatrix}^T \quad (\text{A.2})$$

The computed response is linearized around the nominal values of the parameter multipliers.

$$\bar{r} \cong \bar{r}_0 + \left( \bar{S} \right)_{\bar{p}_0} \delta \bar{p}_0 \quad (\text{A.3})$$

The minimization problem can be formulated with the parameter-response combined vector

$\bar{z}$  and the corresponding block covariance matrix  $\bar{C}$  as follows:

$$\bar{z} \equiv \begin{bmatrix} \bar{p} - \bar{p}_0 \\ \bar{r} - \bar{r}_m \end{bmatrix}, \quad \bar{C} = \begin{bmatrix} \bar{C}_p & \bar{C}_{pr} \\ \bar{C}_{rp} & \bar{C}_m \end{bmatrix} \quad (\text{A.4})$$

where,  $\bar{C}_{pr} = \bar{C}_{rp}^T$  is the parameter-response covariance matrix. The minimization problem is

then given by:

$$\min_p \left\{ \bar{z}^T \bar{C}^{-1} \bar{z} \right\}$$



$$\begin{aligned}
&= \min_p \left\{ \begin{bmatrix} \bar{p} - \bar{p}_0 \\ \bar{r}_m - \bar{r} \end{bmatrix}^T \begin{bmatrix} \bar{C}_p & \bar{C}_{pr} \\ \bar{C}_{rp} & \bar{C}_m \end{bmatrix}^{-1} \begin{bmatrix} \bar{p} - \bar{p}_0 \\ \bar{r}_m - \bar{r} \end{bmatrix} \right\} \\
&= \min_p \left\{ \begin{bmatrix} \bar{p} - \bar{p}_0 \\ \bar{r}_m - \bar{r}_0 - \bar{S}(\bar{p} - \bar{p}_0) \end{bmatrix}^T \begin{bmatrix} \bar{K}_p & \bar{K}_{pr} \\ \bar{K}_{rp} & \bar{K}_r \end{bmatrix} \begin{bmatrix} \bar{p} - \bar{p}_0 \\ \bar{r}_m - \bar{r}_0 - \bar{S}(\bar{p} - \bar{p}_0) \end{bmatrix} \right\} \\
&= \min_p \left\{ \begin{aligned} & \begin{bmatrix} \bar{p} - \bar{p}_0 \end{bmatrix}^T \bar{K}_p \begin{bmatrix} \bar{p} - \bar{p}_0 \end{bmatrix} + \begin{bmatrix} \bar{r}_m - \bar{r}_0 - \bar{S}(\bar{p} - \bar{p}_0) \end{bmatrix}^T \bar{K}_{rp} \begin{bmatrix} \bar{p} - \bar{p}_0 \end{bmatrix} \\ & + \begin{bmatrix} \bar{p} - \bar{p}_0 \end{bmatrix}^T \bar{K}_{pr} \begin{bmatrix} \bar{r}_m - \bar{r}_0 - \bar{S}(\bar{p} - \bar{p}_0) \end{bmatrix} \\ & + \begin{bmatrix} \bar{r}_m - \bar{r}_0 - \bar{S}(\bar{p} - \bar{p}_0) \end{bmatrix}^T \bar{K}_r \begin{bmatrix} \bar{r}_m - \bar{r}_0 - \bar{S}(\bar{p} - \bar{p}_0) \end{bmatrix} \end{aligned} \right\} \quad (\text{A.5})
\end{aligned}$$

where,  $\bar{K} = \begin{bmatrix} \bar{K}_p & \bar{K}_{pr} \\ \bar{K}_{rp} & \bar{K}_r \end{bmatrix}$  is the pseudo-inverse matrix of  $\bar{C}$ , and matrix dimensions of  $\bar{K}_p$ ,

$\bar{K}_{pr}$ ,  $\bar{K}_{rp}$ , and  $\bar{K}_r$  are identical to the dimensions of  $\bar{C}_p$ ,  $\bar{C}_{pr}$ ,  $\bar{C}_{rp}$ , and  $\bar{C}_m$ , respectively.

Solution to the minimization problem is then accomplished by differentiating the above equation with respect to  $\bar{p}$  and setting the result equal to zero. Differentiating Equation (A.5) after generalizing the problem to include a regularization parameter,  $\alpha$ , to address any ill-conditioning and to control the amount of parameter adjustments allowed, results in the following:

$$\begin{aligned}
&\alpha^2 \bar{K}_p \begin{bmatrix} \bar{p} - \bar{p}_0 \end{bmatrix} - \bar{S}^T \bar{K}_{rp} \begin{bmatrix} \bar{p} - \bar{p}_0 \end{bmatrix} \\
&+ \bar{K}_{pr} \begin{bmatrix} \bar{r}_m - \bar{r}_0 - \bar{S}(\bar{p} - \bar{p}_0) \end{bmatrix} - \bar{S}^T \bar{K}_r \begin{bmatrix} \bar{r}_m - \bar{r}_0 - \bar{S}(\bar{p} - \bar{p}_0) \end{bmatrix} = 0
\end{aligned}$$

Solving for the a posteriori parameter value produces:

$$\bar{p}_0^{post} = \bar{p}_0 + \left[ \bar{S}^T \bar{K}_r \bar{S} - \bar{S}^T \bar{K}_{rp} - \bar{K}_{pr} \bar{S} + \alpha^2 \bar{K}_p \right]^{-1} \left[ \bar{S}^T \bar{K}_r - \bar{K}_{pr} \right] \left[ \bar{r}_m - \bar{r}_0 \right] \quad (\text{A.6})$$

$$\bar{r}^{post} \cong \bar{r}(\bar{p}_0^{post}) + \left( \bar{S} \right)_{\bar{p}_0^{post}} \delta \bar{p}^{post} = \bar{r}_0^{post} + \left( \bar{S} \right)_{\bar{p}_0^{post}} \delta \bar{p}^{post} \quad (\text{A.7})$$

The a posteriori parameter covariance matrix can be computed by:

$$\bar{C}_p^{post} \equiv \left\langle \left[ \bar{p} - \bar{p}_0^{post} \right] \left[ \bar{p} - \bar{p}_0^{post} \right]^T \right\rangle \quad (\text{A.8})$$

Substituting a posteriori parameters into Equation (A.8) produces the following expression

for  $\bar{C}_p^{post}$  :

$$\begin{aligned} \bar{C}_p^{post} &= \left\langle \left[ \bar{p} - \bar{p}_0 - \left[ \bar{S}^T \bar{K}_r \bar{S} - \bar{S}^T \bar{K}_{rp} - \bar{K}_{pr} \bar{S} + \alpha^2 \bar{K}_p \right]^{-1} \left[ \bar{S}^T \bar{K}_r - \bar{K}_{pr} \right] \left[ \bar{r}_m - \bar{r}_0 \right] \right. \right. \\ &\quad \left. \left. \times \left[ \bar{p} - \bar{p}_0 - \left[ \bar{S}^T \bar{K}_r \bar{S} - \bar{S}^T \bar{K}_{rp} - \bar{K}_{pr} \bar{S} + \alpha^2 \bar{K}_p \right]^{-1} \left[ \bar{S}^T \bar{K}_r - \bar{K}_{pr} \right] \left[ \bar{r}_m - \bar{r}_0 \right] \right]^T \right\rangle \\ &= \bar{C}_p^{prior} - \left\langle \left[ \bar{p} - \bar{p}_0 \right] \left[ \bar{r}_m - \bar{r} + \bar{S}(\bar{p} - \bar{p}_0) \right]^T \right\rangle \left[ \bar{K}_r \bar{S} - \bar{K}_{rp} \right] \left[ \bar{S}^T \bar{K}_r \bar{S} - \bar{S}^T \bar{K}_{rp} - \bar{K}_{pr} \bar{S} + \alpha^2 \bar{K}_p \right]^{-T} \\ &\quad - \left[ \bar{S}^T \bar{K}_r \bar{S} - \bar{S}^T \bar{K}_{rp} - \bar{K}_{pr} \bar{S} + \alpha^2 \bar{K}_p \right]^{-1} \left[ \bar{S}^T \bar{K}_r - \bar{K}_{pr} \right] \left\langle \left[ \bar{r}_m - \bar{r} + \bar{S}(\bar{p} - \bar{p}_0) \right] \left[ \bar{p} - \bar{p}_0 \right]^T \right\rangle \\ &\quad + \left[ \bar{S}^T \bar{K}_r \bar{S} - \bar{S}^T \bar{K}_{rp} - \bar{K}_{pr} \bar{S} + \alpha^2 \bar{K}_p \right]^{-1} \left[ \bar{S}^T \bar{K}_r - \bar{K}_{pr} \right] \\ &\quad \times \left\langle \left[ \bar{r}_m - \bar{r} + \bar{S}(\bar{p} - \bar{p}_0) \right] \left[ \bar{r}_m - \bar{r} + \bar{S}(\bar{p} - \bar{p}_0) \right]^T \right\rangle \\ &\quad \times \left[ \bar{K}_r \bar{S} - \bar{K}_{rp} \right] \left[ \bar{S}^T \bar{K}_r \bar{S} - \bar{S}^T \bar{K}_{rp} - \bar{K}_{pr} \bar{S} + \alpha^2 \bar{K}_p \right]^{-T} \end{aligned}$$

$$\begin{aligned}
&= \bar{C}_p^{prior} + \left[ \bar{C}_{pr} - \bar{C}_p^{prior} \bar{S}^T \right] \left[ \bar{K}_r \bar{S} - \bar{K}_{rp} \right] \left[ \bar{S}^T \bar{K}_r \bar{S} - \bar{S}^T \bar{K}_{rp} - \bar{K}_{pr} \bar{S} + \alpha^2 \bar{K}_p \right]^{-T} \\
&+ \left[ \bar{S}^T \bar{K}_r \bar{S} - \bar{S}^T \bar{K}_{rp} - \bar{K}_{pr} \bar{S} + \alpha^2 \bar{K}_p \right]^{-1} \left[ \bar{S}^T \bar{K}_r - \bar{K}_{pr} \right] \left[ \bar{C}_{rp} - \bar{S} \bar{C}_p^{prior} \right] \\
&+ \left[ \bar{S}^T \bar{K}_r \bar{S} - \bar{S}^T \bar{K}_{rp} - \bar{K}_{pr} \bar{S} + \alpha^2 \bar{K}_p \right]^{-1} \left[ \bar{S}^T \bar{K}_r - \bar{K}_{pr} \right] \left[ \bar{C}_m - \bar{C}_{rp} \bar{S}^T - \bar{S} \bar{C}_{pr} + \bar{S} \bar{C}_p^{prior} \bar{S}^T \right] \\
&\times \left[ \bar{K}_r \bar{S} - \bar{K}_{rp} \right] \left[ \bar{S}^T \bar{K}_r \bar{S} - \bar{S}^T \bar{K}_{rp} - \bar{K}_{pr} \bar{S} + \alpha^2 \bar{K}_p \right]^{T-1}
\end{aligned} \tag{A.9}$$

The a posteriori parameter-response covariance matrix can be computed by:

$$\bar{C}_{pr}^{post} \equiv \bar{C}_{rp}^{postT} \equiv \left\langle \left[ \bar{p} - \bar{p}_0 \right] \left[ \bar{r} - \bar{r}_m \right]^T \right\rangle \tag{A.10}$$

$$\begin{aligned}
&\bar{C}_{pr}^{post} \\
&= \left\langle \left[ \bar{p} - \bar{p}_0 - \left[ \bar{S}^T \bar{K}_r \bar{S} - \bar{S}^T \bar{K}_{rp} - \bar{K}_{pr} \bar{S} + \alpha^2 \bar{K}_p \right]^{-1} \left[ \bar{S}^T \bar{K}_r - \bar{K}_{pr} \right] \left[ \bar{r}_m - \bar{r}_0 \right] \right] \left[ \bar{r} - \bar{r}_m \right]^T \right\rangle \\
&= \left\langle \left[ \bar{p} - \bar{p}_0 \right] \left[ \bar{r} - \bar{r}_m \right]^T \right\rangle + \left[ \bar{S}^T \bar{K}_r \bar{S} - \bar{S}^T \bar{K}_{rp} - \bar{K}_{pr} \bar{S} + \alpha^2 \bar{K}_p \right]^{-1} \left[ \bar{S}^T \bar{K}_r - \bar{K}_{pr} \right] \\
&\times \left\langle \left[ \bar{r} - \bar{r}_m - \bar{S} \left( \bar{p} - \bar{p}_0 \right) \right] \left[ \bar{r} - \bar{r}_m \right]^T \right\rangle \\
&= \bar{C}_{pr} - \left[ \bar{S}^T \bar{K}_r \bar{S} - \bar{S}^T \bar{K}_{rp} - \bar{K}_{pr} \bar{S} + \alpha^2 \bar{K}_p \right]^{-1} \left[ \bar{S}^T \bar{K}_r - \bar{K}_{pr} \right] \left[ \bar{C}_m - \bar{S} \bar{C}_{pr} \right]
\end{aligned} \tag{A.11}$$

The subsequent step of the iteration procedure would then be to use the above a posteriori values as a priori information, and compute the new best-estimate quantities by using these formulas again.

## Appendix B

The appendix presents the models and numerics employed in the IRIS simulator. In 1-D geometry, the mass continuity equation is:

$$A \frac{\partial \rho}{\partial t} + \frac{\partial}{\partial z}(\rho v A) = 0 \quad (\text{B.1})$$

where  $A$  is the cross section area,  $\rho$  is the fluid density and  $v$  is the flow velocity.

Integrating Equation (B.1) over the  $j$  th cell,

$$\int_{j-1/2}^{j+1/2} \left[ A \frac{\partial \rho}{\partial t} + \frac{\partial}{\partial z}(\rho v A) \right] dz = 0$$

$$V_j \frac{\partial \rho_j}{\partial t} + \rho_{j+1/2} v_{j+1/2} A_{j+1/2} - \rho_{j-1/2} v_{j-1/2} A_{j-1/2} = 0 \quad (\text{B.2})$$

Using the semi-implicit time advancement method,

$$V_j \frac{\rho_j^{t+\Delta t} - \rho_j^t}{\Delta t} + \rho_{j+1/2}^t v_{j+1/2}^{t+\Delta t} A_{j+1/2} - \rho_{j-1/2}^t v_{j-1/2}^{t+\Delta t} A_{j-1/2} = 0 \quad (\text{B.3})$$

where  $V_j$  is the volume of the  $j$  th cell. Since the mass equation is linear in the new time value, the mass at the next time step can be obtained after the first iteration as follows:

$$V_j \frac{\rho_j^{K+1} - \rho_j^t}{\Delta t} + \rho_{j+1/2}^t v_{j+1/2}^{K+1} A_{j+1/2} - \rho_{j-1/2}^t v_{j-1/2}^{K+1} A_{j-1/2} = 0$$

$$\rho_j^{K+1} = \rho_j^t - \frac{\Delta t}{V_j} \left( \rho_{j+1/2}^t v_{j+1/2}^{K+1} A_{j+1/2} - \rho_{j-1/2}^t v_{j-1/2}^{K+1} A_{j-1/2} \right) \quad (\text{B.4})$$

where  $K$  is the iteration index. The internal energy equation is:

$$A \frac{\partial}{\partial t}(\rho u) + \frac{\partial}{\partial z}(\rho u v A) = -P \frac{\partial}{\partial z}(v A) + q'(z) \quad (\text{B.5})$$

where  $u$  is the internal energy,  $P$  is the pressure and  $q'(z)$  is the heat transfer rate per unit distance in the steam generators. Integrating Equation (B.5) over the  $j$  th cell and implementing the semi-implicit time advancement,

$$\int_{j-1/2}^{j+1/2} \left[ A \frac{\partial}{\partial t} (\rho u) + \frac{\partial}{\partial z} (\rho u v A) \right] dz = \int_{j-1/2}^{j+1/2} \left[ -P \frac{\partial}{\partial z} (v A) + q'(z) \right] dz$$

$$V_j \frac{(\rho u)_j^{t+\Delta t} - (\rho u)_j^t}{\Delta t} + (\rho u)_{j+1/2}^t v_{j+1/2}^{t+\Delta t} A_{j+1/2} - (\rho u)_{j-1/2}^t v_{j-1/2}^{t+\Delta t} A_{j-1/2}$$

$$= -P_j^t (v_{j+1/2}^{t+\Delta t} A_{j+1/2} - v_{j-1/2}^{t+\Delta t} A_{j-1/2}) + q_j^t \quad (\text{B.6})$$

The internal energy equation is linear in the new time value. Thus the  $\rho u$  term at the next time step can be obtained after the first iteration as follows:

$$V_j \frac{(\rho u)_j^{K+1} - (\rho u)_j^t}{\Delta t} + (\rho u)_{j+1/2}^t v_{j+1/2}^{K+1} A_{j+1/2} - (\rho u)_{j-1/2}^t v_{j-1/2}^{K+1} A_{j-1/2}$$

$$= -P_j^t (v_{j+1/2}^{K+1} A_{j+1/2} - v_{j-1/2}^{K+1} A_{j-1/2}) + q_j^t$$

$$(\rho u)_j^{K+1} = (\rho u)_j^t - \frac{\Delta t}{V_j} \left[ v_{j+1/2}^{K+1} A_{j+1/2} \left\{ (\rho u)_{j+1/2}^t + P_j^t \right\} - v_{j-1/2}^{K+1} A_{j-1/2} \left\{ (\rho u)_{j-1/2}^t + P_j^t \right\} - q_j^t \right] \quad (\text{B.7})$$

Conservation of momentum in a fluid is given by:

$$\rho \frac{\partial v}{\partial t} + \rho v \frac{\partial v}{\partial z} = -\frac{\partial P}{\partial z} - k' \rho \frac{v^2}{2} - \rho g \sin \theta + \Delta P_p' \quad (\text{B.8})$$

where  $k'$  is the loss coefficient per unit distance,  $g$  is the standard gravity and  $\Delta P_p'$  is the pressure change per unit distance across the pump. Integrating the momentum equation from  $j$  to  $j+1$  and implementing time advancement,

$$\int_j^{j+1} \left[ \rho \frac{\partial v}{\partial t} + \rho v \frac{\partial v}{\partial z} \right] dz = \int_j^{j+1} \left[ -\frac{\partial P}{\partial z} - k' \rho \frac{v^2}{2} - \rho g \sin \theta + \Delta P_p' \right] dz$$

$$\begin{aligned} & \Delta z_{j+1/2} \rho_{j+1/2}^t \frac{v_{j+1/2}^{t+\Delta t} - v_{j+1/2}^t}{\Delta t} + \rho_{j+1/2}^t v_{j+1/2}^t (v_{j+1}^t - v_j^t)^* \\ & = - (P_{j+1}^{t+\Delta t} - P_j^{t+\Delta t}) - k_{j+1/2} \rho_{j+1/2}^t \frac{v_{j+1/2}^{t+\Delta t} |v_{j+1/2}^{t+\Delta t}|}{2} - \Delta z_{j+1/2} \rho_{j+1/2}^t g \sin \theta_{j+1/2} + \Delta P_p^t \end{aligned} \quad (\text{B.9})$$

$$\text{where, } \sin \theta_{j+1/2} = \frac{H_{j+1} - H_j}{\Delta z_{j+1/2}} = \frac{\Delta H_{j+1/2}}{\Delta z_{j+1/2}}$$

The momentum equation is nonlinear in the new time velocity. Linearizing this term gives:

$$\begin{aligned} & \rho_{j+1/2}^t \frac{v_{j+1/2}^{K+1} - v_{j+1/2}^t}{\Delta t} + \rho_{j+1/2}^t v_{j+1/2}^t \left( \frac{v_{j+1}^t - v_j^t}{\Delta z_{j+1/2}} \right)^* \\ & = - \frac{(P_{j+1}^{K+1} - P_j^{K+1})}{\Delta z_{j+1/2}} - \frac{k_{j+1/2}}{\Delta z_{j+1/2}} \rho_{j+1/2}^t \frac{(2v_{j+1/2}^{K+1} - v_{j+1/2}^K) |v_{j+1/2}^K|}{2} - \rho_{j+1/2}^t g \frac{\Delta H_{j+1/2}}{\Delta z_{j+1/2}} + \frac{\Delta P_p^t}{\Delta z_{j+1/2}} \end{aligned} \quad (\text{B.10})$$

$$\text{where, } \left( \frac{v_{j+1}^t - v_j^t}{\Delta z_{j+1/2}} \right)^* = \frac{v_{j+1/2}^t - \left[ \frac{1}{2} \{v_{j-1/2}^t + v_{j+3/2}^t\} + \frac{1}{2} \frac{|v_{j+1/2}^t|}{v_{j+1/2}^t} \{v_{j-1/2}^t - v_{j+3/2}^t\} \right]}{\frac{1}{2} \{ \Delta z_j + \Delta z_{j+1} \} + \frac{1}{2} \frac{|v_{j+1/2}^t|}{v_{j+1/2}^t} \{ \Delta z_j - \Delta z_{j+1} \}}$$

Solving Equation (B.10) for  $v_{j+1/2}^{K+1}$  produces following equation:

$$\begin{aligned} v_{j+1/2}^{K+1} & = \frac{v_{j+1/2}^t}{\alpha_{j+1/2}^K} - \frac{v_{j+1/2}^t}{\alpha_{j+1/2}^K} \left( \frac{v_{j+1}^t - v_j^t}{\Delta z_{j+1/2}} \right)^* \Delta t - \frac{\Delta t}{\Delta z_{j+1/2}} \frac{(P_{j+1}^{K+1} - P_j^{K+1})}{\rho_{j+1/2}^t \alpha_{j+1/2}^K} + k_{j+1/2} \frac{\Delta t}{\Delta z_{j+1/2}} \frac{v_{j+1/2}^K |v_{j+1/2}^K|}{2 \alpha_{j+1/2}^K} \\ & - g \frac{\Delta t}{\Delta z_{j+1/2}} \frac{\Delta H_{j+1/2}}{\alpha_{j+1/2}^K} + \frac{\Delta t}{\Delta z_{j+1/2}} \frac{\Delta P_p^t}{\rho_{j+1/2}^t \alpha_{j+1/2}^K} \end{aligned} \quad (\text{B.11})$$

$$\text{where } \alpha_{j+1/2}^K = \left( 1 + k_{j+1/2} \frac{\Delta t}{\Delta z_{j+1/2}} |v_{j+1/2}^K| \right)$$

The fluid velocity at node  $j+1/2$  and  $j-1/2$  is then simply,

$$v_{j+1/2}^{K+1} = -(a)_{j+1/2}^K P_{j+1}^{K+1} + (a)_{j+1/2}^K P_j^{K+1} + (c)_{j+1/2}^K \quad (\text{B.12})$$

$$v_{j-1/2}^{K+1} = -(a)_{j-1/2}^K P_j^{K+1} + (a)_{j-1/2}^K P_{j-1}^{K+1} + (c)_{j-1/2}^K \quad (\text{B.13})$$

$$\text{where } (a)_{j+1/2}^K \equiv \frac{\Delta t}{\Delta z_{j+1/2} \rho_{j+1/2}^t \alpha_{j+1/2}^K}$$

and

$$(c)_{j+1/2}^K \equiv -\frac{v_{j+1/2}^t}{\alpha_{j+1/2}^K} \left( \frac{v_{j+1}^t - v_j^t}{\Delta z_{j+1/2}} \right)^* \Delta t + \frac{v_{j+1/2}^t}{\alpha_{j+1/2}^K} + k_{j+1/2} \frac{\Delta t}{\Delta z_{j+1/2}} \frac{v_{j+1/2}^K |v_{j+1/2}^K|}{2\alpha_{j+1/2}^K} - g \frac{\Delta t}{\Delta z_{j+1/2}} \frac{\Delta H_{j+1/2}}{\alpha_{j+1/2}^K} \\ + \frac{\Delta t}{\Delta z_{j+1/2}} \frac{\Delta P_{pj}^t}{\rho_{j+1/2}^t \alpha_{j+1/2}^K}$$

Substituting the new time velocity into the mass and internal energy equations produces the

following equations for  $\rho_j^{K+1}$  and  $(\rho u)_j^{K+1}$ :

$$\rho_j^{K+1} = \frac{\Delta t}{V_j} \rho_{j-1/2}^t A_{j-1/2} (a)_{j-1/2}^K P_{j-1}^{K+1} - \frac{\Delta t}{V_j} \rho_{j-1/2}^t A_{j-1/2} (a)_{j-1/2}^K P_j^{K+1} \\ - \frac{\Delta t}{V_j} \rho_{j+1/2}^t A_{j+1/2} (a)_{j+1/2}^K P_j^{K+1} + \frac{\Delta t}{V_j} \rho_{j+1/2}^t A_{j+1/2} (a)_{j+1/2}^K P_{j+1}^{K+1} \quad (\text{B.14}) \\ + \frac{\Delta t}{V_j} \rho_{j-1/2}^t A_{j-1/2} (c)_{j-1/2}^K - \frac{\Delta t}{V_j} \rho_{j+1/2}^t A_{j+1/2} (c)_{j+1/2}^K + \rho_j^t$$

$$(\rho u)_j^{K+1} = \frac{\Delta t}{V_j} (a)_{j+1/2}^K P_{j+1}^{K+1} A_{j+1/2} \left\{ (\rho u)_{j+1/2}^t + P_j^t \right\} - \frac{\Delta t}{V_j} (a)_{j+1/2}^K P_j^{K+1} A_{j+1/2} \left\{ (\rho u)_{j+1/2}^t + P_j^t \right\} \\ - \frac{\Delta t}{V_j} (a)_{j-1/2}^K P_j^{K+1} A_{j-1/2} \left\{ (\rho u)_{j-1/2}^t + P_j^t \right\} + \frac{\Delta t}{V_j} (a)_{j-1/2}^K P_{j-1}^{K+1} A_{j-1/2} \left\{ (\rho u)_{j-1/2}^t + P_j^t \right\} \quad (\text{B.15}) \\ - \frac{\Delta t}{V_j} (c)_{j+1/2}^K A_{j+1/2} \left\{ (\rho u)_{j+1/2}^t + P_j^t \right\} + \frac{\Delta t}{V_j} (c)_{j-1/2}^K A_{j-1/2} \left\{ (\rho u)_{j-1/2}^t + P_j^t \right\} \\ + (\rho u)_j^t + \frac{\Delta t}{V_j} q_j^t$$

The equations of state are:

$$\rho_j^{K+1} = \tilde{\rho}_j^K + \delta u_j \left. \frac{\partial \rho}{\partial u} \right|_j^K + (P_j^{K+1} - P_j^K) \left. \frac{\partial \rho}{\partial P} \right|_j^K \quad (\text{B.16})$$

$$(\rho u)_j^{K+1} = (\tilde{\rho} u)_j^K + \delta u_j \left( \tilde{\rho}_j^K + u_j^K \left. \frac{\partial \rho}{\partial u} \right|_j^K \right) + (P_j^{K+1} - P_j^K) u_j^K \left. \frac{\partial \rho}{\partial P} \right|_j^K \quad (\text{B.17})$$

where,  $\tilde{\rho}_j^K = \rho(u_j^K, P_j^K)$

The internal energy at the new time step  $u_j^{K+1}$  is derived as:

$$u_j^{K+1} = u_j^K + \left[ \rho_j^{K+1} - \tilde{\rho}_j^K - (P_j^{K+1} - P_j^K) \left. \frac{\partial \rho}{\partial P} \right|_j^K \right] / \left. \frac{\partial \rho}{\partial u} \right|_j^K \quad (\text{B.18})$$

Setting the right hand side of Equation (B.14) equal to the right hand side of Equation (B.16),

$$\begin{aligned} & \frac{\Delta t}{V_j} \rho'_{j-1/2} A_{j-1/2} (a)_{j-1/2}^K P_{j-1}^{K+1} - \frac{\Delta t}{V_j} \rho'_{j-1/2} A_{j-1/2} (a)_{j-1/2}^K P_j^{K+1} \\ & - \frac{\Delta t}{V_j} \rho'_{j+1/2} A_{j+1/2} (a)_{j+1/2}^K P_j^{K+1} + \frac{\Delta t}{V_j} \rho'_{j+1/2} A_{j+1/2} (a)_{j+1/2}^K P_{j+1}^{K+1} \\ & + \frac{\Delta t}{V_j} \rho'_{j-1/2} A_{j-1/2} (c)_{j-1/2}^K - \frac{\Delta t}{V_j} \rho'_{j+1/2} A_{j+1/2} (c)_{j+1/2}^K + \rho'_j \\ & = \tilde{\rho}_j^K + \delta u_j \left. \frac{\partial \rho}{\partial u} \right|_j^K + (P_j^{K+1} - P_j^K) \left. \frac{\partial \rho}{\partial P} \right|_j^K \end{aligned} \quad (\text{B.19})$$

Dividing both sides of Equation of (B.19) by  $\left. \frac{\partial \rho}{\partial u} \right|_j^K$  and solving for  $\delta u_j$  gives:



$$\begin{aligned}
\delta u_j = & \frac{\Delta t}{V_j} \rho_{j-1/2}^t A_{j-1/2} (a)_{j-1/2}^K P_j^{K+1} \left/ \frac{\partial \rho}{\partial u} \right|_j^K - \frac{\Delta t}{V_j} \rho_{j-1/2}^t A_{j-1/2} (a)_{j-1/2}^K P_j^{K+1} \left/ \frac{\partial \rho}{\partial u} \right|_j^K \\
& - P_j^{K+1} \frac{\partial \rho}{\partial P} \left|_j^K \right/ \frac{\partial \rho}{\partial u} \left|_j^K \\
& - \frac{\Delta t}{V_j} \rho_{j+1/2}^t A_{j+1/2} (a)_{j+1/2}^K P_j^{K+1} \left/ \frac{\partial \rho}{\partial u} \right|_j^K + \frac{\Delta t}{V_j} \rho_{j+1/2}^t A_{j+1/2} (a)_{j+1/2}^K P_{j+1}^{K+1} \left/ \frac{\partial \rho}{\partial u} \right|_j^K \\
& + \frac{\Delta t}{V_j} \rho_{j-1/2}^t A_{j-1/2} (c)_{j-1/2}^K \left/ \frac{\partial \rho}{\partial u} \right|_j^K - \frac{\Delta t}{V_j} \rho_{j+1/2}^t A_{j+1/2} (c)_{j+1/2}^K \left/ \frac{\partial \rho}{\partial u} \right|_j^K \\
& + \left( \rho_j^t - \tilde{\rho}_j^K + P_j^K \frac{\partial \rho}{\partial P} \left|_j^K \right) \right/ \frac{\partial \rho}{\partial u} \left|_j^K
\end{aligned} \tag{B.20}$$

Since Equation (B.15) is equal to Equation (B.17),

$$\begin{aligned}
& \frac{\Delta t}{V_j} (a)_{j+1/2}^K P_{j+1}^{K+1} A_{j+1/2} \left\{ (\rho u)_{j+1/2}^t + P_j^t \right\} - \frac{\Delta t}{V_j} (a)_{j+1/2}^K P_j^{K+1} A_{j+1/2} \left\{ (\rho u)_{j+1/2}^t + P_j^t \right\} \\
& - \frac{\Delta t}{V_j} (a)_{j-1/2}^K P_j^{K+1} A_{j-1/2} \left\{ (\rho u)_{j-1/2}^t + P_j^t \right\} + \frac{\Delta t}{V_j} (a)_{j-1/2}^K P_{j-1}^{K+1} A_{j-1/2} \left\{ (\rho u)_{j-1/2}^t + P_j^t \right\} \\
& - \frac{\Delta t}{V_j} (c)_{j+1/2}^K A_{j+1/2} \left\{ (\rho u)_{j+1/2}^t + P_j^t \right\} + \frac{\Delta t}{V_j} (c)_{j-1/2}^K A_{j-1/2} \left\{ (\rho u)_{j-1/2}^t + P_j^t \right\} \\
& + (\rho u)_j^t + \frac{\Delta t}{V_j} q_j^t \\
& = (\tilde{\rho} u)_j^K + \delta u_j \left( \tilde{\rho}_j^K + u_j^K \frac{\partial \rho}{\partial u} \left|_j^K \right) \right) + (P_j^{K+1} - P_j^K) u_j^K \frac{\partial \rho}{\partial P} \left|_j^K
\end{aligned} \tag{B.21}$$

Dividing both sides of Equation (B.21) by  $\left( \tilde{\rho}_j^K + u_j^K \frac{\partial \rho}{\partial u} \left|_j^K \right) \right)$  produces the following

expression for  $\delta u_j$ :

$$\begin{aligned}
\delta u_j = & \frac{\Delta t}{V_j} (a)_{j-1/2}^K P_{j-1}^{K+1} A_{j-1/2} \left\{ (\rho u)_{j-1/2}^t + P_j^t \right\} \left/ \left( \tilde{\rho}_j^K + u_j^K \frac{\partial \rho}{\partial u} \Big|_j^K \right) \right. \\
& - \frac{\Delta t}{V_j} (a)_{j-1/2}^K P_j^{K+1} A_{j-1/2} \left\{ (\rho u)_{j-1/2}^t + P_j^t \right\} \left/ \left( \tilde{\rho}_j^K + u_j^K \frac{\partial \rho}{\partial u} \Big|_j^K \right) \right. \\
& - P_j^{K+1} u_j^K \frac{\partial \rho}{\partial P} \Big|_j^K \left/ \left( \tilde{\rho}_j^K + u_j^K \frac{\partial \rho}{\partial u} \Big|_j^K \right) \right. \\
& - \frac{\Delta t}{V_j} (a)_{j+1/2}^K P_j^{K+1} A_{j+1/2} \left\{ (\rho u)_{j+1/2}^t + P_j^t \right\} \left/ \left( \tilde{\rho}_j^K + u_j^K \frac{\partial \rho}{\partial u} \Big|_j^K \right) \right. \\
& + \frac{\Delta t}{V_j} (a)_{j+1/2}^K P_{j+1}^{K+1} A_{j+1/2} \left\{ (\rho u)_{j+1/2}^t + P_j^t \right\} \left/ \left( \tilde{\rho}_j^K + u_j^K \frac{\partial \rho}{\partial u} \Big|_j^K \right) \right. \\
& + \frac{\Delta t}{V_j} (c)_{j-1/2}^K A_{j-1/2} \left\{ (\rho u)_{j-1/2}^t + P_j^t \right\} \left/ \left( \tilde{\rho}_j^K + u_j^K \frac{\partial \rho}{\partial u} \Big|_j^K \right) \right. \\
& - \frac{\Delta t}{V_j} (c)_{j+1/2}^K A_{j+1/2} \left\{ (\rho u)_{j+1/2}^t + P_j^t \right\} \left/ \left( \tilde{\rho}_j^K + u_j^K \frac{\partial \rho}{\partial u} \Big|_j^K \right) \right. \\
& + \left( (\rho u)_j^t + \frac{\Delta t}{V_j} q_j^t - (\tilde{\rho} u)_j^K + P_j^K u_j^K \frac{\partial \rho}{\partial P} \Big|_j^K \right) \left/ \left( \tilde{\rho}_j^K + u_j^K \frac{\partial \rho}{\partial u} \Big|_j^K \right) \right.
\end{aligned} \tag{B.22}$$

The final form of the equation for pressure is then obtained by subtracting equation (B.22) from equation (B.20) as follows:

$$\begin{aligned}
& \left[ \rho'_{j-1/2} \left/ \frac{\partial \rho}{\partial u} \right|_j^K - \left\{ (\rho u)'_{j-1/2} + P'_j \right\} \left/ \left( \tilde{\rho}_j^K + u_j^K \frac{\partial \rho}{\partial u} \Big|_j^K \right) \right] \frac{\Delta t}{V_j} (a)_{j-1/2}^K A_{j-1/2} P_j^{K+1} \\
& - \left[ \rho'_{j-1/2} \left/ \frac{\partial \rho}{\partial u} \right|_j^K - \left\{ (\rho u)'_{j-1/2} + P'_j \right\} \left/ \left( \tilde{\rho}_j^K + u_j^K \frac{\partial \rho}{\partial u} \Big|_j^K \right) \right] \frac{\Delta t}{V_j} (a)_{j-1/2}^K A_{j-1/2} P_j^{K+1} \\
& - \left[ \frac{\partial \rho}{\partial P} \Big|_j^K \left/ \frac{\partial \rho}{\partial u} \Big|_j^K - u_j^K \frac{\partial \rho}{\partial P} \Big|_j^K \left/ \left( \tilde{\rho}_j^K + u_j^K \frac{\partial \rho}{\partial u} \Big|_j^K \right) \right] P_j^{K+1} \\
& - \left[ \rho'_{j+1/2} \left/ \frac{\partial \rho}{\partial u} \right|_j^K - \left\{ (\rho u)'_{j+1/2} + P'_j \right\} \left/ \left( \tilde{\rho}_j^K + u_j^K \frac{\partial \rho}{\partial u} \Big|_j^K \right) \right] \frac{\Delta t}{V_j} (a)_{j+1/2}^K A_{j+1/2} P_j^{K+1} \\
& + \left[ \rho'_{j+1/2} \left/ \frac{\partial \rho}{\partial u} \right|_j^K - \left\{ (\rho u)'_{j+1/2} + P'_j \right\} \left/ \left( \tilde{\rho}_j^K + u_j^K \frac{\partial \rho}{\partial u} \Big|_j^K \right) \right] \frac{\Delta t}{V_j} (a)_{j+1/2}^K A_{j+1/2} P_{j+1}^{K+1} \\
& = - \left[ \rho'_{j-1/2} \left/ \frac{\partial \rho}{\partial u} \right|_j^K - \left\{ (\rho u)'_{j-1/2} + P'_j \right\} \left/ \left( \tilde{\rho}_j^K + u_j^K \frac{\partial \rho}{\partial u} \Big|_j^K \right) \right] \frac{\Delta t}{V_j} (c)_{j-1/2}^K A_{j-1/2} \\
& + \left[ \rho'_{j+1/2} \left/ \frac{\partial \rho}{\partial u} \right|_j^K - \left\{ (\rho u)'_{j+1/2} + P'_j \right\} \left/ \left( \tilde{\rho}_j^K + u_j^K \frac{\partial \rho}{\partial u} \Big|_j^K \right) \right] \frac{\Delta t}{V_j} (c)_{j+1/2}^K A_{j+1/2} \\
& - \left( \rho'_j - \tilde{\rho}_j^K + P_j^K \frac{\partial \rho}{\partial P} \Big|_j^K \right) \left/ \frac{\partial \rho}{\partial u} \Big|_j^K \tag{B.23} \\
& + \left( (\rho u)'_j + \frac{\Delta t}{V_j} q'_j - (\tilde{\rho} u)'_j + P_j^K u_j^K \frac{\partial \rho}{\partial P} \Big|_j^K \right) \left/ \left( \tilde{\rho}_j^K + u_j^K \frac{\partial \rho}{\partial u} \Big|_j^K \right)
\end{aligned}$$

Thus, the form of the equations for the pressure is simply:

$$C_{j-1}^K P_{j-1}^{K+1} - (C_{j-1}^K + C_j^K + C_{j+1}^K) P_j^{K+1} + C_{j+1}^K P_{j+1}^{K+1} = S_{j-1}^K + S_j^K + S_{j+1}^K \tag{B.24}$$

Equation (B.24) can be solved using the tri-diagonal matrix solver.